Model Development and Validation of Samaria Doped Ceria (SDC) Based Solid Oxide Fuel Cell Operating with Practical Fuels

by

Mazni Ismail

A thesis
presented to the University of Waterloo
in fulfillment of the
thesis requirement for the degree of
Doctor of Philosophy
in
Chemical Engineering

Waterloo, Ontario, Canada, 2013

AUTHOR'S DECLARATION

I hereby declare that I am the sole author of this thesis. This is a true copy of the thesis, including any required final revisions, as accepted by my examiners.

I understand that my thesis may be made electronically available to the public.

Abstract

Solid Oxide Fuel Cell (SOFC) is a promising technology for producing electricity cleanly and efficiently. This type of fuel cell is a high temperature fuel cell operating around 1000°C for state-of-the-art SOFC. An advantage of the high temperature is the possibility of combined heat and power generation which would even further increase the efficiency of this technology. However, due to high operating temperatures, there are problems associated with the development and commercialization of SOFC, such as requirement of high temperature gas seals, and relatively poor long-term stability. The current trend in SOFC development is therefore to reduce the operating temperature of the cell to the range 600-800°C. However, this requires developing new cell designs and materials since decreasing the operating temperature increases the ohmic overpotential due to higher ionic diffusion resistance in the electrolyte, thereby reducing electrochemical performance. For intermediate temperature SOFC, SDC is a promising electrolyte material to reduce the ohmic overpotential.

The present research focused on developing a 1D model of SDC based SOFC validated for a number of feed gas compositions, from humidified H_2, mixture of CO and CO_2, to several syngas compositions (typical of diesel syngas, biomass syngas and pre-reformed natural gas). The model was developed for an anode supported cell. Few parameters were used as free fit parameters: essentially structural parameters, such as porosity and tortuosity, as well as kinetic parameters for H_2 and CO electrochemical reactions. In most cases, the simulated results (polarization curve) fitted well the experimental data. It was seen that the performance of CO/CO_2 system is considerably lower than the H_2/H_2O system. The model results also allowed to access variables' profiles that would not be accessible experimentally, such species composition profile and local current density along the anode. In particular, it was observed that most the electrochemical reaction occurred within 10 μm away from the anode/electrolyte interface.

In the literature, the water-gas shift (WGS) reaction is considered to occur only over Ni, but the present work demonstrated that SDC is active toward the WGS reaction. Therefore, a kinetic study was carried out to determine a rate expression for the WGS reaction. This rate

expression was then incorporated into the SOFC model. The results indicated that inclusion of the WGS reaction on SDC has minor or negligible effect in most situations, except in the case of CO mole fraction for the diesel syngas feed at higher cell voltage. The reason was that the composition of diesel syngas was such that there was a higher driving force for the WGS reaction to proceed in the reverse WGS direction. When the water content is high enough, as in the case of higher current densities, the form of the derived rate expression for the WGS on SDC makes the value of this rate very small. The rate expression was derived using relatively small amounts of water because of experimental limitation and therefore, the form of this rate needs to be revisited by considering higher amount of water.

Acknowledgements

I would like to thank my supervisor Professor Eric Croiset, for his invaluable guidance, patience and encouragement throughout my study. I appreciate the prayers, understanding, encouragement, sacrifice and unconditional love from my husband, Raja Mohd Taufika, family members and my friends. I am also grateful to fellow researchers Asmida, Monrudee, Aiyu and Weifang for their support and help. I also owe my special thanks to all my Waterloo friends for the support and courage that I shall not forget, in my mind and my heart. Last but not least, my best ever friend, Noorlisa for her support, tolerance, courage and help. Finally, financial supports from Ministry of Higher Education, Malaysia and University of Waterloo are also gratefully acknowledged.

Dedication

Dedicated to my beloved husband, parents, sisters and brothers….

Table of Contents

List of Figures

List of Tables

Nomenclature

List of English symbols

D_{ij}	Binary diffusion coefficient
D_{ik}^{eff}	Effective Knudsen diffusion coefficients
D_{im}^{eff}	Effective molecular diffusion coefficient
$\mathbf{d}_k$	Diffusional driving force acting on species k
E_a	Activation energy
$E_{a,e}$	Activation energy for the electronic conductivity
$E_{a,i}$	Activation energy for the ionic conductivity
E_{cell}	Cell potential
E^o	Reversible fuel cell voltage
F	Faraday's constant
F_i	Molar flow rate of species i
F_I	Flow rate of inert
F_T	Total flow rate
$\mathrm{i_o}$	Exchange current density
J	Current density
k	Reaction rate constant
K	Equilibrium constant
M	Molecular weight
N_i	Molar flux of species i
n_i^{in}	Inlet molar flow rate of species i
n_i^{out}	Outlet molar flow rate of species i
P	Pressure
r	Reaction rate
R	Gas constant
T	Temperature
V	Voltage

v_i	Molar diffusion volume of species *i*
V_{ref}	Relative potential difference between the electronic and ionic conductors
W	Mass of catalyst
X_i	Conversion of species *i*
Y_i	Product yield of species *i*
ΔG_i	Standard Gibb's energy of species *i*
$\dot{S}_c$	Rate of production or consumption of electric charge

List of Greek symbols

η_{ohm}	Ohmic overpotential
η_{act}	Activation overpotential
η_{con}	Concentration overpotential
η_T	Total overpotential
α	Exchange transfer coefficient
ε_{ij}	Characteristic Lennard-Jones energy
ρ	density in kg/m^3
σ	Conductivity
$\sigma_{E,i}$	Standard electronic conductivity
σ_i	Diameter of the molecular collision
$\sigma_{o,i}$	Standard ionic conductivity
τ	Tortuosity factor for molecular diffusion
φ	Porosity of the porous structure
Ω_D	Collision integral
ω_i	Mass fraction of species *i*

List of abbreviations and acronyms

AFC	Alkaline Fuel Cell
CHP	combined heat and power

GHSV	Gas Hourly Space Velocity
IT-SOFC	Intermediate Temperature Solid Oxide Fuel Cell
JCRs	Joint Confidence Regions
LSM	Strontium doped Lanthanum Manganite
MCFC	Molten Carbonate Fuel Cell
MCMC	Markov Chain Monte Carlo
MFCs	Mass-Flow Controllers
MSR	Methane Steam Reforming
Ni-SDC	Nickel-Samaria Doped Ceria
OCV	Open Circuit Voltage
PAFC	Phosphoric Acid Fuel Cell
PEMFC	Polymer Electrolyte Membrane Fuel Cell
RWGS	Reverse Water Gas Shift RWGS
SDC	Samaria-Doped Ceria
SOFC	Solid Oxide Fuel Cell
TPB	Three Phase boundary
WGS	Water Gas Shift
YSZ	Yittria-Stabilized Zirconia

Chapter 1
Introduction

One of the major drivers to accelerate the development of fuel cells is the increasing concern about the environmental consequences of the continuous use of fossil fuels for both stationary and transportation applications. With the rising concern about greenhouse gas emissions, many efforts are being pursued to develop more efficient energy conversion devices to replace conventional combustion heat engines. Fuel cell technologies offer efficient and clean conversion of chemical energy of fuels to electrical energy. The waste stream from a fuel cell using H_2 fuel contains primarily water and heat, thereby greatly reducing greenhouse gases. Even for the fuel cells that can operate on hydrocarbons, the greenhouse gas emissions can be significantly reduced due to the higher efficiency. Also, the operation of some fuel cells (e.g. solid oxide fuel cell, SOFC) are such that CO_2 capture could potentially be implemented with relatively low penalty since the cell exhaust is composed mainly of CO_2 and water. Therefore, research focusing on the improvement of performance of SOFCs is increasing.

In addition, since no nitrogen oxides or particulates are emitted, fuel cells are known as a very clean technology. With rising fuel prices and stricter emission control regulations, these capabilities make fuel cells even more attractive.

Solid Oxide Fuel Cell (SOFC) is a type of high temperature fuel cell which operates at about 1000°C and is thus capable of producing both electricity and heat. A very important advantage of SOFC is that it can tolerate many types of fuel, including hydrocarbon fuels, natural gas, synthesis gas (syngas) and humidified hydrogen (H_2) (Shi and Cai, 2006). Furthermore, since SOFC operates at high temperatures, SOFC can reform hydrocarbon fuels internally. Internal reforming in a SOFC simplifies the overall system design because the external reformer can be eliminated. A SOFC system with internal reforming has an inherent advantage in terms of energy efficiency because the heat required for the reforming reaction is supplied by the heat generated by the electrochemical reaction. Moreover, the ceramic

solid-phase electrolyte reduces corrosion considerations and eliminates electrolyte management problems associated with liquid electrolyte fuel cells. Thus, many advantages have led to significant SOFC research and development efforts for SOFC commercialization (Ding and Liu, 2008; Young et al., 2008).

There are still numerous issues that need to be addressed before full SOFC commercialization is possible. The barriers for full scale commercialization of SOFC are the high cost and relatively poor long term stability due to the high temperature used in current state-of-the-art SOFCs. Recently, considerable R&D efforts are being made to reduce the SOFC operating temperature to intermediate temperatures in the range 600-800°C. These lower temperatures allow for a wider choice of compartment materials that will reduce the cost and increase the cell stability by reducing thermal degradation. Unfortunately, decreasing the operating temperature also reduces the electrochemical performance since the overpotential increases due to higher ionic diffusion resistance in the electrolyte. In addition, more carbon coking issues on the anode are occurring in the intermediate temperatures range. To alleviate these problems, designs of intermediate temperature SOFC (IT-SOFC) aim at reducing the thickness of the electrolyte and improving the anode material and design.

Since improving the performance of SOFC at low operating temperature is an important challenge in SOFC technology, the overall goal of this research is to enhance the IT-SOFC performance using anode supported button cell design for direct use of hydrocarbon fuels. This will be done via a combination of mathematical modelling and experimental validation. Nickel-Samaria Doped Ceria (Ni-SDC) anode material will be considered in the present work because SDC is a promising electrolyte material for intermediate temperature SOFCs. The performance of SOFC using Ni-SDC anodes was studied over a wide range of fuels compositions (3% humidified H_2, 20%CO/80%CO_2, and different syngas compositions). Also, a 1D button cell model was developed incorporating all relevant physical, chemical and electrochemical processes by considering the electrochemical reactions occurring along the

thickness of the electrodes, and not only at the boundary between the electrode and electrolyte.

1.1 Motivation of the Research

Recently, many efforts have been made toward developing intermediate-temperature SOFC (IT-SOFC) operating in the temperature range 600-800°C, because such temperatures enable the use of low cost metallic interconnects, shorter start-up time and improved long-term stability of cell materials by reducing the material degradation rate. Unfortunately, decreasing the operating temperature increases the ohmic overpotential due to higher ionic diffusion in the electrolyte resistance, thereby reducing electrochemical performance. To alleviate this problem, designs of IT-SOFC aim at reducing the thickness of the electrolyte while increasing that of the anode. In such design, ohmic losses are reduced. Therefore this research focused on anode supported cell which is done via a combination of mathematical modelling and experimental validation. Methane reforming reaction and water-gas shift reaction have been taken into account in the modelling for syngas composition. For the water gas shift reaction, it was assumed that this reaction occurs not only on Ni (like all reported studies assumed), but also on SDC. The electrochemical reactions were assumed to be able to occur along the thickness of the electrodes, and not only at the boundary between the electrode and electrolyte.

There are two specific objectives in this work:

1) Determine the reaction rate expression for water gas shift reaction on SDC.
2) Develop a 1D model that can predict the performance of the cell and on the Ni/SDC material under different operating conditions (e.g. temperature, current density, fuel composition).

In order to achieve these objectives, two research scopes have been considered:

1) Kinetic Study: Developed a kinetic expression for the reverse water gas shift reaction combining experiments and calculations using Matlab codes involving a non-linear least square problem (lsqcurvefit command).

2) Modelling Study: Developed a one-dimensional mechanistic model of anode supported button cells that considers that electrochemical reaction occurs not only at anode/electrolyte interface to predict SOFC performance. The model was validated with experimental data produced in the SOFC group at the University of Waterloo.

1.2 Research Contributions

1) Developed the first Ni/SDC model validated for various fuel compositions; 97%H_2/3%H_2O, 20%CO/80%CO_2, syngas compositions (diesel, biomass, pre-reformed natural gas). At the time of writing this thesis, there is only one paper in the literature (Cui et al., 2010) dealing with SDC-electrolyte SOFC modeling, but their model was validated only with humidified hydrogen.
2) Demonstrated that SDC is active towards the water gas shift reaction (WGS) and determined the kinetic parameters of WGS using Matlab codes involving solving a non-linear least square problem (lsqcurvefit command). The WGS on SDC was then incorporated in the modeling study.

1.3 Thesis Outline

This thesis is organised into seven chapters, as follows:
Chapter 1 presents an introduction of the research and discusses the motivation of the research, its objectives and its contribution.

Chapter 2 presents a general discussion about fuel cells and an overview of several studies on SOFC single cell modelling.

Chapter 3 describes the experimental techniques including material preparation to study the activity of methane steam reforming (MSR) and kinetics of water gas shift reaction.

Chapter 4 demonstrates the activity of SDC toward the water-gas shift reaction and describes the kinetic study of the water gas shift reaction on SDC.

Chapter 5 describes the model formulation for a 1D SOFC model of button cell.

Chapter 6 discusses the results of the modelling study involving H_2/H_2O, CO/CO_2 and syngas compositions.

Chapter 7 presents the conclusions and recommendations for this work.

Chapter 2
Literature Review

2.1 Introduction

This chapter begins with a general discussion about fuel cells, and then focuses on solid oxide fuel cells (SOFC) including SOFC fuels, materials, cell design and performance. In the last section (section 2.4), an overview of several studies on SOFC modelling is provided.

2.2 Fuel Cells in Brief

The fuel cell, an electrochemical energy conversion device which directly converts chemical to electrical energy, is a promising technology for producing electricity cleanly and efficiently. The invention of fuel cells as energy conversion systems began in the middle of the 19th century (Hirschenhofer et al., 1998; Stambouli and Traversa, 2002). Because of its high energy efficiency and being environmentally friendly, fuel cells are considered to be potentially attractive devices to produce electricity.

Fuel cells exist in different types. There are five major types of fuel cells: phosphoric acid fuel cell (PAFC), polymer electrolyte membrane fuel cell (PEMFC), alkaline fuel cell (AFC), molten carbonate fuel cell (MCFC) and solid oxide fuel cell (SOFC). The types of fuel cells differ primarily by the type of electrolyte they employ, charge carrier, operating temperature, material, fuel tolerance and performance characteristics, as listed in Table 2.1.

Although the five types of fuel cells have different characteristics, the basic structure of all fuel cells is similar. The cell consists of two electrodes called anode and cathode separated by an electrolyte and connected to an external circuit. A schematic representation of a fuel cell with the reactant and product and the ion conduction flow directions through the cell is shown in Figure 2.1.

Table 2.1: Types of fuel cells (Li, 2006; O'Hayre et al., 2006)

Characteristic	Type of fuel cells				
	PEMFC	PAFC	AFC	MCFC	SOFC
Electrolyte	Polymer membrane	Liquid H_3PO_4 (immobilized)	Liquid KOH (immobilized)	Molten carbonate	Ceramic
Charge carrier	H^+	H^+	OH^-	CO_3^{2-}	O^{2-}
Operating temperature (°C)	50-80	160-220	60-220	600-700	600-1000
Catalyst	Platinum (cathode / anode)	Platinum (cathode / anode)	Platinum (cathode / anode)	Nickel (cathode / anode)	Ni: anode $LaSrMnO_3$: cathode
Cell component	Carbon based	Carbon based	Carbon based	Stainless based	Ceramic based
Fuel compatibility	H_2, methanol	H_2	H_2	H_2, CH_4	H_2, CH_4, CO
Fuel efficiency (Chemical to electrical)	45-60	55	40-60	60-65	55-65

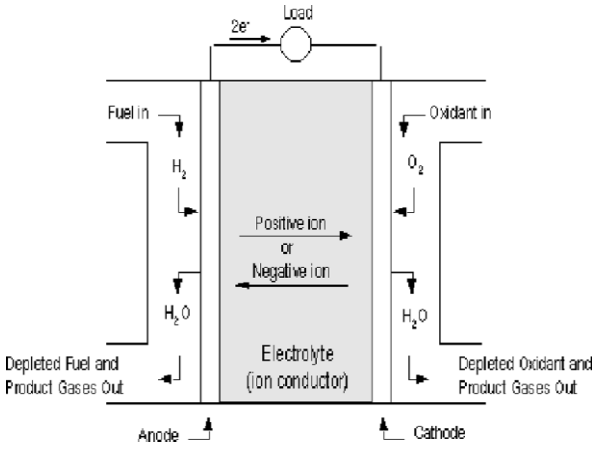

Figure 2.1: Diagram of a single fuel cell (Lisbona et al., 2005)

In a typical fuel cell, gaseous fuels (e.g. hydrogen) are fed continuously to the anode and an oxidant (typically oxygen from air) is fed continuously to the cathode. The electrochemical reactions take place in the electrodes to produce an electric current. The function of the electrolyte is to conduct ionic charges between the electrodes (Lisbona et al., 2005). Individual fuel cells have a maximum output voltage on the order of 1 V. Substantial

voltages and power outputs are obtained by connecting many cells electrically in series to form a fuel cell stack.

All five fuel cell types have different electrochemical reactions. The electrochemical reactions occurring at the anode and cathode sides are summarized in Table 2.2.

Table 2.2: Anodic and cathodic reactions of fuel cells (Selman and Lin, 1993)

Fuel Cell	Anode Reaction	Cathode Reaction
PEMFC	$H_2 \rightarrow 2H^+ + 2e^-$	$O_2 + 4H^+ + 4e^- \rightarrow 2H_2O$
PAFC	$H_2 \rightarrow 2H^+ + 2e^-$	$O_2 + 4H^+ + 4e^- \rightarrow 2H_2O$
AFC	$H_2 + 2OH^- \rightarrow 2H_2O + 2e^-$	$O_2 + 2H_2O + 4e^- \rightarrow 4OH^-$
MCFC	$H_2 + CO_3^{2-} \rightarrow H_2O + CO_2 + 2e^-$ $CO + CO_3^{2-} \rightarrow 2CO_2 + 2e^-$	$O_2 + 2CO_2 + 4e^- \rightarrow 2CO_3^{2-}$
SOFC	$H_2 + O^{2-} \rightarrow H_2O + 2e^-$ $CO + O^{2-} \rightarrow CO_2 + 2e^-$	$O_2 + 4e^- \rightarrow 2O^{2-}$

The operational principles of fuel cells and batteries have similarities: both are galvanic cells. They consist of an anode and a cathode in contact with an electrolyte. Both devices generate electrical energy by converting chemical energy using an electrochemical reaction. These reactions occur at the anode and cathode with the electron transfer forced through an external load in order to complete the reaction. Individual cells of both batteries and fuel cells generate only small voltages, which are then combined in series to achieve substantial voltage and power capacities.

Fuel cells differ from batteries in which the chemical reactants are stored. In a battery, the anode and cathode are consumed during use. Thus, a battery can only operate until these materials are fully consumed after which it either must be replaced or recharged, depending on the nature of the materials. In a fuel cell, the chemical reactants are supplied from an external source so that its materials of construction are never consumed and do not need to be recharged. A fuel cell continues to operate as long as reactants are supplied and the reaction products are removed (O'Hayre et al., 2006).

The choice of electrochemical device, either battery or fuel cell, depends upon use. For larger scale applications, fuel cells have several advantages over batteries including smaller size, lighter weight, quick refuelling and longer range.

Fuel cells and combustion engines also share some similarities. Both fuel cells and internal combustion engines completely oxidize the fuel. Fuel cells use pure hydrogen or a reformate gas mixture. Internal combustion engines typically use hydrogen containing fossil fuels directly, although they could be configured to operate using pure hydrogen. Both systems use air as the oxidant. In some respects, fuel cells and internal combustion engines are fundamentally different. Fuel cells react the fuel and oxidant electrochemically whereas internal combustion engines react the fuel and oxidant through combustion. Like other electrochemical devices, fuel cells are not limited by the Carnot efficiency as combustion engines are (Lisbona et al., 2005). For example, when ethanol is burned in a combustion engine, the energy efficiency is limited by the Carnot efficiency and can reach, in practice, only about 25%. This fuel efficiency can be significantly increased when ethanol is first converted to hydrogen and then used in a fuel cell with an efficiency of more than 50% (Rass-Hansen et al., 2007).

Applications of fuel cells are in transportation, power generation and in powering mobile devices (Shi and Cai, 2006). The application of fuel cells in the transportation sector increases fuel efficiency, decreases foreign oil dependency and becomes an important technology to fight climate change. As fuel cell vehicles begin to operate on fuels from natural gas or gasoline, greenhouse gas emissions will be reduced. The PEM fuel cell is regarded as ideally suited for transportation applications due to its high power density, high energy conversion efficiency, compactness, lightweight nature and low operating temperature (below 100°C).

For stationary power generation applications, both low-temperature and high-temperature fuel cells could be utilized. The low-temperature fuel cells have the advantage that usually a

faster start-up time can be achieved, which makes it more attractive for small-power generation. The high-temperature systems such as SOFC and MCFC generate high-grade heat which can be used directly in a heat cycle or indirectly by incorporating the fuel cell system into a combined cycle. SOFC and MCFC are more suitable for large-scale power plants (Dokiya, 2002). SOFCs are expected to play a significant role in residential combined heat and power (CHP) applications (1 to 10 kW) and commercial CHP applications (up to 250 kW), or power plant stationary applications (Wei Zhang, 2006).

2.3 Solid Oxide Fuel Cell

SOFC is a high temperature fuel cell operating around 1000°C for state-of-the-art SOFCs, composed of a YSZ (Yittria-Stabilized Zirconia, $(Y_2O_3)_{0.08}$ $(ZrO_2)_{0.92}$) electrolyte, Ni-YSZ anode, LSM (Strontium doped Lanthanum Manganite, $La_{1-x}Sr_xMnO_3$) and cathode (Singhal, 2000; Zhu and Deevi, 2003). An advantage of the high operating temperature is the possibility of combined heat and power generation which would even further increase the efficiency of this technology (Singhal, 2000). An even more important advantage of SOFC compared to low temperature fuel cells (e.g. PEMFC) is not only the lower cost of the electrocatalyst (Ni for SOFC, as opposed to Pt for PEMFC), but also that they are tolerant to CO, making SOFC fuel flexible (Stambouli and Traversa, 2002). Moreover, the high operating temperature allows internal reforming of the fuel to form H_2 and CO, where the heat released by the electrochemical reaction can be utilized by the endothermic steam reforming reaction (Ahmed and Foger, 2000). Internal reforming can also lower the overall system costs because steam required for the steam reforming can be obtained from the steam generated by the electrochemical fuel cell reaction, and because of reduced maintenance due to the elimination of an external reformer (Clarke et al., 1997; Boder and Dittmeyer, 2006; Cheekatamarla et al., 2008). All of these advantages make the SOFC an even more attractive means for producing electrical power.

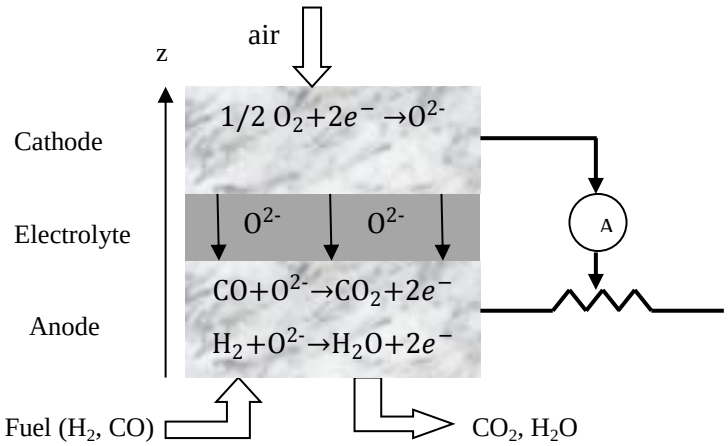

Figure 2.2: Schematic diagram of SOFC operation

Figure 2.2 shows the main components of a SOFC, consisting of two electrodes, called anode and cathode, separated by a dense solid electrolyte. The electrodes are porous to facilitate the transport of fuel and oxidant from the gas channels to the three phase boundaries where electrochemical reactions occur. Within an SOFC anode structure, the hydrocarbon's fuel may be reformed via heterogeneous reaction to produce H_2 and CO in the presence of a reforming catalyst (e.g. Ni). The CO may further react with H_2O to form H_2 and CO_2 via the water–gas-shift reaction. Within the anode, the pore spaces are typically sufficiently small that the most likely collisions are between gas molecules and surfaces, and there is very little probability for gas–gas collisions. Consequently, gas phase homogeneous kinetics are usually negligible (Hecht et al., 2005; Zhu and Kee, 2008).

The electrolyte is dense to keep the gases separated and to allow an oxygen concentration difference between the anode and the cathode. Oxygen ions are produced at the three phase boundaries near the cathode/electrolyte interface and are transported by a solid-state migration mechanism through the electrolyte to the anode/electrolyte interface, where oxygen ions react with the fuel (Badwal, and Foger, 1996). Products generated from the reaction are transported back to the fuel channel through pores.

The electrochemical reactions at the anode are:

$$H_2 + O^{2-} \rightarrow H_2O + 2e^- \quad (2.1)$$
$$CO + O^{2-} \rightarrow CO_2 + 2e^-$$

The electrochemical reaction at the cathode is:

$$1/2O_2 + 2e^- \rightarrow O^{2-} \quad (2.2)$$

The O^{2-} ion is drawn through the electrolyte from the cathode to the anode, while electrons are forced through an external circuit from the anode to the cathode. These electrochemical reactions occur continuously as long as enough fuel and oxidant are supplied to the SOFC.

SOFC Fuel:

As was previously stated, one of the major advantages of SOFC is fuel flexibility: fuels that can be used in a SOFC can be hydrogen (H_2), carbon monoxide (CO), methane (CH_4) or some higher hydrocarbons and synthesis gas from solid fuels (coal and biomass) (Li et al., 2010). This feature reduces considerably the cost intensive efforts for producing high quality pure hydrogen, as demanded by other types of low temperature fuel cells.

Hydrocarbon based fuels, such as methane, can be reformed to produce H_2 and CO. Reforming is a chemical process that reacts hydrogen-containing fuels in the presence of steam, oxygen, or both, into a hydrogen-rich gas stream. The resulting hydrogen-rich gas mixture is called reformate. Reforming can be further subdivided according to whether (1) it occurs in a chemical reactor outside the fuel cell (external reforming) or (2) it occurs at the catalyst surface inside the fuel cell itself (internal reforming), the latter being possible in high temperature fuel cells.

Methane steam reforming is one of the most widely used processes for the production of H_2 and CO mixtures. In fact, methane steam reforming accounts for 95% of the hydrogen produced in the United States (Blaylock et al., 2009). Methane steam reforming is an endothermic reaction and is normally carried out at temperatures around 700-800°C in the presence of a suitable catalyst. Nickel used as anode material can act as a methane steam

reforming catalyst. In the reforming of the methane with steam, the dominant reactions are the following two reactions:

$$CH_4 + H_2O \leftrightarrow CO + 3H_2 \text{ (steam reforming)} \quad (2.3)$$

$$CO + H_2O \leftrightarrow CO_2 + H_2 \text{ (water gas shift reaction)}$$

The steam reforming reaction is a slow and highly endothermic reaction, and the water gas shift (WGS) reaction is a fast and weakly exothermic reaction. Therefore, the overall reaction resulting from the methane steam reforming reaction and the water gas shift reaction is highly endothermic. Several authors have assumed that the water gas shift reaction is at equilibrium at the reforming temperature (Nagata et al., 2001).

Methane steam reforming is affected by operating pressure, temperature and the ratio of steam to carbon in the feed gas. Methane steam reforming is favourable at low pressure, high temperature and high steam-to-carbon ratio.

Although internal reforming offers an advantage in terms of reducing the overall system cost, it also poses the problem of carbon deposition with the use of Ni-based catalyst which deteriorates the performance of the cell. Methane tends to dissociate on the surface of the nickel particles, depositing carbon, and the CO produced through MSR can also contribute to carbon deposition, as indicated by the following reactions:

$$CH_4 \rightarrow C + 2H_2 \text{(methane cracking)} \quad (2.4)$$

$$2CO \leftrightarrow C + CO_2 \text{ (Boudouard)}$$

$$CO + H_2 \leftrightarrow C + H_2O \text{ (CO hydrogenation)}$$

The formation of carbon is a serious problem in solid oxide fuel cells fed with hydrocarbons. Although the ability to utilize hydrocarbons as a fuel is an important attribute of SOFC, because of carbon formation problems associated with pure hydrocarbon fuels, practical SOFC systems usually operate with mixtures of H_2, CO, and hydrocarbons (Hecht et al., 2005). In addition to reducing carbon formation, mixing the hydrocarbon fuel with H_2 and CO can also avoid thermal stresses in the SOFC, as regions where the highly endothermic

methane steam reforming reaction occurs will experience a decrease in temperature. Large temperature differences can cause localized thermal stress within the cell and can lead to cracking of the cell material. (Pastula et al., 2001; Mogensen et al., 2011). Therefore, the amount of hydrocarbon in the fuel must be carefully controlled to avoid localized thermal stress due to internal steam reforming.

Carbon deposition results in anode deactivation because deposited carbon can plug gas flow paths, thereby blocking the active sites, which leads to a loss of cell performance and poor durability. Internal reforming requires an anode material that possesses good catalytic reforming properties as well as good carbon deposition resistance for the effective generation of power by the fuel cell.

For SOFCs running on direct CH_4 feed, alternative anode materials to Ni-YSZ, or new formulations are necessary. The anodes should be compatible with the SOFC electrolyte, possess acceptable conductivity and thermal expansion coefficient, and appropriate catalytic and electrocatalytic properties with low coking activity (Fergus, 1990; Wincewics and Cooper, 2005).

Increasing the amount of steam relative to hydrocarbon is a common way of preventing carbon deposition in catalytic systems. However, high steam to carbon ratios typically used to suppress carbon formation are unattractive for fuel cells as they lower the SOFC's efficiency because of fuel dilution by steam (Ahmed and Foger, 2000; Gunji et al., 2004). High steam concentration is also not desirable because additional heat is required to heat and vaporize water. A more satisfactory solution is to develop materials suitable for internal reforming and resistant to coking.

In addition, state-of-the-art SOFCs operating at around 1000°C show durability problems, essentially due to the very high operating temperature. Such high temperatures are required to achieve sufficiently high ionic conductivity in the electrolyte. A temperature of 1000°C

also reduces the choice of materials to be used and leads to high cell costs. The current trend in SOFC's development is, therefore, to reduce the operating temperature of the cell and to develop high performance electrodes for intermediate temperature solid oxide fuel cells (IT-SOFC) especially with the use of high carbon deposition resistance materials that can operate with minimal steam to carbon ratio. A typical temperature range for IT-SOFC would be 600 to 800°C.

SOFC Components Material:

SOFC components consist of five main parts which are electrolyte, cathode, anode, interconnect and seal. Because SOFC operates at high temperature, all cell components must withstand high temperature. State-of-the-art high temperature SOFC usually employs yttria-stabilized zirconia (YSZ) electrolyte which is an oxygen ion conductor, a lanthanum strontium manganite (LSM) cathode and a nickel-YSZ cermet (a cermet is a mixture of ceramic and metal) anode, operating in the temperature range of 600–1000^{o}C (Badwal, 2001; Hart et al., 2001; Ivers-Tiffee et al., 2001; Deseure et al., 2005; Ni et al., 2007; Yang et al., 2012).

YSZ is a preferred electrolyte material for SOFC because it exhibits predominately ionic conductivity without electronic conductivity. Its electronic conductivity must be kept as low as possible to prevent losses from leakage currents. The YSZ electrolyte is a very dense layer with low gas permeability to prevent reactant gas crossover. Furthermore, YSZ is highly stable in both reducing and oxidizing environments. This characteristic is important for the electrolyte since it is exposed to both anode and cathode sides (Li, 2006). The high operating temperatures of SOFCs allow the oxygen ion transport to be sufficient for good performance. However, as the operating temperature decreases, the electrolyte begins to have large ionic transport resistances, which affect significantly the performance. Ohmic overpotential at lower operating temperatures (IT-SOFC) could be reduced by using alternative electrolytes that have higher ionic conductivity than conventional YSZ electrolytes such as SDC (Peng et al., 2002; Singh et al., 2007; Wang et al., 2008; Chen et al., 2009; Yang et al., 2012) or by

adopting an electrode-supported configuration with a thinner electrolyte. One promising configuration for IT-SOFCs is an anode-supported SOFC where a thin electrolyte of thickness in the ranges of 8–15 μm is deposited on a thick anode (Shi et al., 2007a).

Pure CeO_2 has a cubic fluorite structure (Minh and Takahashi, 1995). This fluorite structure is built on the basis of a Ce^{4+} cation face centered cubic (FCC) packing with oxygen ions located in the tetrahedral sites of the structure (Fergus et al., 2009). Pure CeO_2 has negligible ionic conductivity.

In general, the ionic conductivity (σ) can be expresses in an Arrhenius form (Nandasiri, 2013).

$$\sigma = \frac{\sigma_o}{T} e^{\frac{-E}{k_B T}} \tag{2.5}$$

where, σ_o is a temperature independent pre-exponential factor, E is the activation energy of ion diffusion, k_B is the Boltzmann constant and T is the temperature.

The oxygen ion conductivity in ceria mainly depends on the oxygen-vacancy formation because the conduction occurs by diffusion of oxygen ions via vacancies. To obtain relatively high oxygen ion conductivity, part of the Ce^{4+} cation in ceria must be doped by another cation with a lower valence state to form oxygen-vacancy in the fluorite lattice (Fergus et al., 2009).Various dopants have been used with CeO_2 including Lanthanum oxide (La_2O_3), Yttrium Oxide (Y_2O_3), Samarium Oxide (Sm_2O_3), Gadolinium Oxide (Gd_2O_3), and other rare earth oxides. The conductivity depends on the characteristic of the dopant elements and their concentrations. At low temperatures, doped CeO_2 shows a higher conductivity and lower conduction activation energy as compared to stabilized ZrO_2 material (Minh and Takahashi, 1995).

Samarium doped ceria (SDC) was reported to exhibit the highest ionic conductivity at fixed doping levels among the rare earth doped ceria. The addition of a small amount of Sm_2O_3

significantly enhances the ionic conductivity because of the formation of a large number of oxygen vacancies in the fluorite lattice (Fergus et al., 2009; Minh and Takahashi, 1995; Ursaki et al., 2012; Yahiro et al., 1987).

The oxygen ionic conductivity of SDC increases with an increase in samaria concentration up to an optimum dopant concentration value and then decreased with increasing samaria concentration. The increase in the oxygen ionic conductivity was attributed to the increase in the number of oxygen vacancies, which decrease the activation energy for oxygen ion diffusion through ceria lattice. However, the formation of defect between dopant cations and oxygen vacancies at higher dopant concentrations increases the activation energy for oxygen ion diffusion which decreases the oxygen ionic conductivity. The optimum dopant concentration reported in the literature for the maximum oxygen ionic conductivity of SDC shows a discrepancy. However most researchers have recommended an optimum samarium concentration of 20 mol % (Nandasiri, 2013).

LSM is widely used as a cathode material due to its high electrochemical activity, good stability, and thermal expansion compatibility with YSZ at the cell operating temperature (Liu et al., 2004). It is advantageous to produce the cathode as a composite of LSM and YSZ. In this way, the electrochemically active reaction zone may be extended from the interface between the electrode and the electrolyte to the bulk of the electrode (Jorgensen et al., 2000). It was shown that by adding 50 wt.% YSZ to the LSM cathode, the polarization resistance could be reduced by 25% of its original value (Hart et al., 2001). If materials other than YSZ are used for the electrolyte, then for compatibility, different cathode materials must be used as well. For example, for SDC electrolyte (Samarium-doped ceria, $Ce_{0.8}Sm_{0.2}O_{1.9}$) a typical cathode would be SSC (Strontium-doped samarium cobaltite, $Sm_{0.5}Sr_{0.5}CoO_3$)(Ding et al., 2008; Zhao et al., 2008; Yang et al., 2012).

At the anode, nickel provides good electron conductivity and good catalytic activity for the internal reforming reaction. The YSZ add ion conductivity, thermal expansion compatibility,

mechanical stability and maintains the high porosity and surface area of the anode structure (O'Hayre et al., 2006). The Ni-YSZ anode shows a high tolerance to sulfur impurity in the fuel stream. Since YSZ conducts oxygen ions, it increases the TPB for the electrochemical reaction in the anode. The percentage of Ni in the Ni-YSZ cermet should be at least 30% by volume to maintain a good electronic conductivity. Since Ni has a high thermal expansion coefficient, the percentage of Ni should be controlled in order to balance the requirement for the electronic conductivity and the thermal expansion match with other SOFC components (Li, 2006).

Other than electrodes and electrolytes, interconnect is also an important component of SOFC to connect individual fuel cells to form a fuel cell stack, so that the electricity each cell generates can be combined to obtain the required voltage. The interconnect can be either a metallic or ceramic layer that sits between each individual cell. Because the interconnect is exposed to both the oxidizing and reducing side of the cell at high temperatures, it must be extremely stable. For this reason, ceramics have been more successful in the long term than metals as interconnect materials. However, these ceramic interconnect materials are very expensive compared to metals. Nickel and steel-based alloys are becoming more promising as lower temperature (600-800°C) SOFCs are developed. The most common intermetallic materials used today are doped lanthanum chromites. Ceramic-metal composites called cermet are also under consideration, as they have demonstrated thermal stability at high temperatures and excellent electrical conductivity (Singhal, 2000; Stambouli and Traversa, 2002).

Seal is necessary for planar SOFCs to prevent fuel and oxidant mixing and leakage. Sealing the SOFC compartments is still a major problem due to the high temperature for which not many sealing materials are available. The most commonly used material for this purpose is glass (SiO_2). Normal glass, however, can evaporate and soften with a higher likelihood of leakages as a result. Pyrex seals can be used to avoid evaporation and glass ceramic sealants

have been proven to have the necessary stability at high temperatures and pressures so that the probability of leakages can be reduced dramatically.

As a conclusion, SOFC components must meet certain general requirements in order to have successful design and excellent SOFC performance. The components must be chemically stable in order to limit chemical interactions with other cell components. They must have very close thermal expansion coefficients in order to minimize thermal stresses that may cause cracking and delamination during thermal cycling or fabrication. It is also desirable that fuel cell components have high strength and durability, are easy to fabricate, and are relatively inexpensive.

Cell Design:

Different SOFC designs have been developed over the years. Among the various configurations, the two most common are tubular and planar (Singhal and kendall, 2003; Arpino et al., 2008). These two configurations are shown in Figure 2.3.

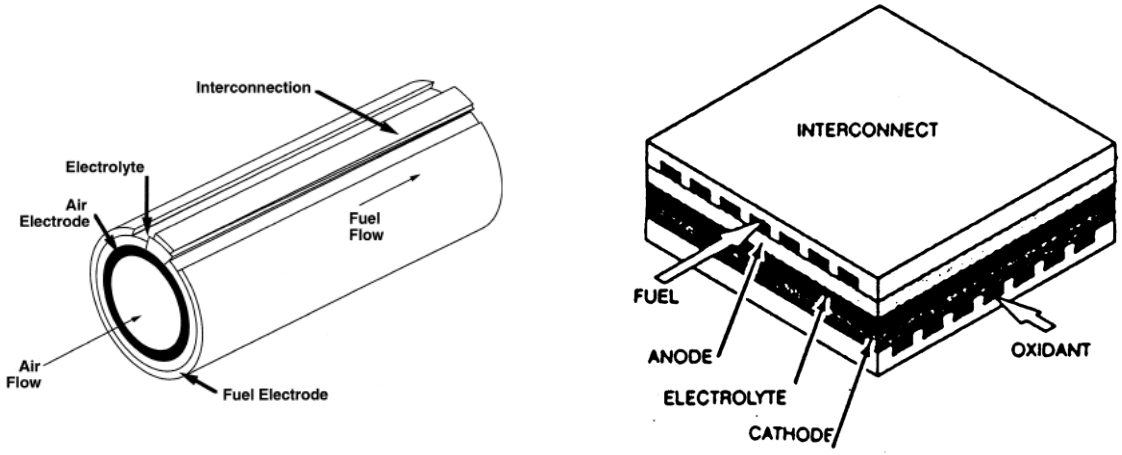

a) Tubular design b) Planar design

Figure 2.3: SOFC design (Singhal, 2000; Yamamoto, 2000)

The planar geometry is the typical sandwich type geometry employed by most types of fuel cells, where the electrolyte is sandwiched in between the electrodes. For the tubular SOFC,

the electrolyte layer forms the middle tube, while either the anode or the cathode tube can be located on the inner side of the electrolyte tube. In tubular geometries, if the anode is located at the inner side of the electrolyte tube, the fuel will be passed through the inside of the tube and the other gas is passed along the outside of the tube. Although earlier cells used the anode on the inner side, more recent cells have the cathode on the inner side for stack consideration. The recent tubular SOFC uses a thicker cathode inside as a support for the entire cell structure (Li, 2006).

The tubular design has a self-sealing structure which improves thermal stability and eliminates the need for good thermal-resistant sealants. However the performance of the planar design is currently better than the performance of the tubular design because the planar design has a lower resistance comparatively, resulting in lower ohmic overpotential (Hussain et al., 2006; Arpino et al., 2008; Yuan, 2010). Furthermore, the planar design offers lower cost and higher power density per unit volume compared to tubular designs. The planar SOFC designs, however, face many challenges in materials development, processing, and system integration that must be overcome.

One of the planar design challenges is the seal technology. The seal needs to provide sufficiently low leak rates (e.g. H_2 into the air stream) so that it will not cause undesirable local heating which can lead to structural or functional failure of the stack. The seal also needs to have long-term stability and cause no degradation of the materials with which they are in contact (e.g. stabilized zirconia, interconnect and electrodes) at the elevated temperatures (e.g. 800^oC) and must sustain harsh environments (oxidizing, reducing and humid). So far, most SOFC seal development has focused on glass or glass–ceramic seals although other approaches, such as cement seals, mica glass–ceramics, brazes, and compressive seals have been proposed (Chou and Stevenson, 2002).

Cell Performance:

Ideal performance of fuel cells can only be obtained by operating fuel cells at open circuit potential where no losses occur. This ideal performance, as shown in Figure 2.4, is impossible to achieve because there are a few prominent losses, which contribute to the deviation of the operating potential from the ideal cell potential.

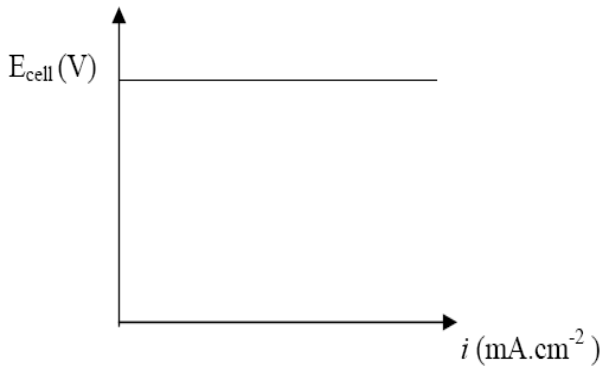

Figure 2.4: Ideal performance of fuel cells

These losses, which are usually referred to as overpotentials or polarizations, are classified into three groups: 1) ohmic, due to the resistance to conduct ions (through the electrolyte) and electronic (through the electrodes and current collectors); 2) activation, due to the energy threshold to be overcome for the electrochemical reaction to take place and 3) concentration, due to the effect of slow mass diffusion through the porous electrodes from bulk flows to reaction places and back to the main gas stream. Concentration overpotential becomes large at high current density where the reactant requirement for the electrochemical reactions exceeds the capability of supplying the reactant to the reaction site (Nagata et al., 2001; Sanchez et al., 2008).

Figure 2.5 depicts a typical cell potential versus its current density which is known as polarization curve. Polarization curves record the voltage change with current density, which are important data for fuel cell performance characterization. A good fuel cell should display a polarization curve with high current density at high cell voltage, indicating high power output of the cell.

Figure 2.5 shows that the cell potential is not ideal and decreases with increasing current density. Three distinct regions can be distinguished from this graph: Region I is controlled mainly by activation polarization, Region II by ohmic resistance (essentially linear and proportional to current density) while Region III is mainly controlled by mass transport limitation.

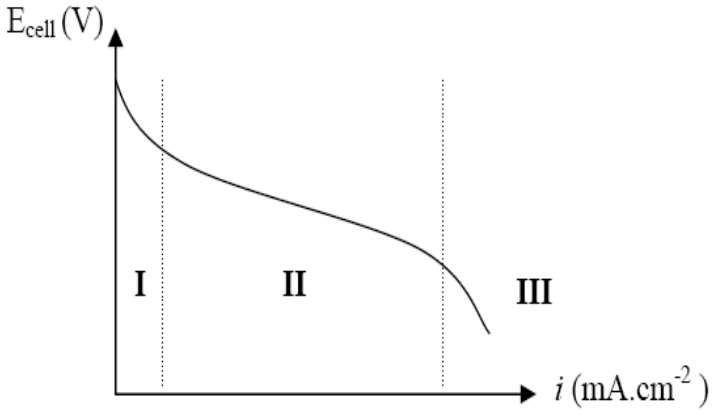

Figure 2.5: Actual performance of fuel cells

These various polarizations are functions of both operating conditions (temperature, pressure, fuel and oxidizer concentration) and physical properties of the cell (material and dimensions). These losses make the voltage of the operating fuel cell (V) compared to ideal potential (E) as

$$V = E - \eta_T \tag{2.6}$$

in which η_T is the total overpotential defined as $\eta_T = \eta_{\text{act}} + \eta_{\text{con}} + \eta_{\text{ohm}}$, where η_{act} , η_{con} and η_{ohm} are activation, concentration and ohmic overpotentials, respectively.

Many of the recent efforts in fuel cell technology development have been devoted to reducing the thickness of critical cell components while refining and improving the electrode structure and electrolyte phase, with the aim of obtaining a higher and more stable electrochemical performance, while lowering the cost (Aguiar et al., 2004). Minimization of the cell polarization can be achieved by choosing appropriate materials, material compositions, cell morphology and cell design. To reduce the activation polarization, one

promising way is to use fine electrode particle size close to the electrode/electrolyte interface. To reduce concentration polarization, the electrode should be coarse with large amounts of porosity in the regions away from the electrolyte. This electrode structure is known as graded electrode. Therefore, graded electrode will be an ideal electrode structure to minimize the activation and concentration polarizations and provides better cell performance (Singhal and Kendall, 2003).

Generally, planar SOFC is fabricated in two designs which are electrolyte-supported or electrode-supported. To reduce the ohmic polarization, electrode supported is preferred compared to electrolyte supported cell. In the electrolyte-supported cell, the electrolyte is the thickest component and works as the support structure. Electrolyte-supported cells are only suitable for high-temperature operation where the ohmic losses can be reduced. Electrode-supported SOFCs have been developed in an attempt to minimize the ohmic losses (generally dominated by the electrolytes resistance) under lower temperature operation, as in the case of IT-SOFCs. In these cells, one of the two electrodes is the thickest component and support structure, while the electrolyte have small thickness. However, many researches have shown that anode-supported design leads to better cell performance than the cathode supported since cathode activation overpotential is higher compared to anode activation overpotential (Yakabe et al., 2000; Ivers-Tiffee el at., 2001; Aguiar et al., 2004). Furthermore, concentration polarization caused by the resistance of mass transport through the electrodes is generally largest at the cathode if cathode supported cells are employed. In the case of anode, diffusion is generally fast due to the low molecular weight of hydrogen. Therefore, an anode supported cell usually gives lower concentration polarization (Singhal and Kendall, 2003). The anode is commonly the thickest and strongest layer in each individual cell, due to the fact that is has the smallest polarization losses, and is often the layer that provides the mechanical support.

2.4 Summary of SOFC Modelling Studies

To predict SOFC performance, different models have been developed. Such models can be for different geometries (tubular or planar), different structures (electrolyte or electrode

supported), and different flow configurations (co- or counter-flow), can range from one to three-dimensional, and either consider or ignore internal reforming or various other phenomena. This section presents an overview of recently published studies on SOFC cell modelling.

Modelling studies on YSZ electrolyte based SOFC

Shi et al. (2007) presented a 2D anode supported model based on button cell geometry for YSZ based cells. The model considered the ionic and electronic conduction, gas transport and electrochemical reaction interdependency. The reaction active sites were assumed to be uniformly distributed in the electrode. All forms of polarization were included in the model. The model was used to predict the cell performance with different humidified H_2 gas compositions, cathode area and anode thickness. The simulation result was validated with data from literature and showed good agreement. However the study should be extended using multi-components fuels which are more practical in actual SOFC applications due to their wide spread availability and distribution availability (Janardhanan and Deutchmann, 2006).

Another study on a 2D YSZ-based SOFC button cell was conducted by Suwanwarangkul et al. (2006) operating on syngas fuel consisting of H_2, CO, H_2O, CO_2 and N_2. Momentum, mass and ionic transport coupled with electrochemical (H_2 oxidation, CO oxidation and O_2 reduction) and chemical reactions (water gas shift) were incorporated in the model. Thermodynamics analysis of the Boudouard reaction for carbon formation was discussed using this model. In this model it was assumed that the electrochemical reactions only occur at the electrode/electrolyte interface. Moreover, Suwanwarangkul et al. (2006) neglected the mass transport and ohmic resistance within the electrodes as the thicknesses of electrodes were very thin and they ignored the electrode subdomains in the model. The model was used to study the effect of operating conditions on carbon formation. This study included experimental validation. The developed model showed good agreement with experimental

data for various syngas compositions obtained at an operating temperature of 900°C but the simulation results deviated somewhat from the experimental data at 800°C.

Zhu et al. (2005) incorporated an elementary heterogeneous chemical kinetics of CH_4 reforming in the form of a multi-step reaction mechanism into a 1D anode supported planar SOFC model to predict fuel cell performance. Fuel gases considered in this model were CH_4, H_2 and CO. They assumed electrochemical reactions occur only at the electrode/electrolyte interface where the charge transfer kinetics were represented by a modified Butler-Volmer equation where the exchange current density was derived from elementary reactions by assuming a single rate-limiting step. At the anode, they assumed only H_2 is involved in the electrochemical reaction. The variations of cell performance due to changes of parameters such as channel dimensions, reaction rates, electrode porosity, fuel composition and flow rate were studied. The model which was able to predict the open circuit potential, current-voltage characteristics, fuel utilization and efficiency was validated with limited experimental data at 800°C available in the literature.

Like Zhu et al. (2005), Janardhanan and Deutschmann (2006) developed a model to analyze the detailed multi-step chemical processes within the anode, electrochemical processes, and losses of anode supported SOFC button cell SOFCs running on CH_4 rich fuel (mixed with 3% H_2O) under internal reforming conditions. The model assumed that the electrochemical reactions occur only at the electrode/electrolyte interface with the hydrogen being the only electrochemically active species. The charge transfer kinetics were represented using the same modified Butler-Volmer equation as in Zhu et al. (2005). The predicted cell performances were compared with experimental data obtained from literature. The results show that model predictions were in good agreement with experimental observations except the open circuit potentials. There was no experimental data to validate the anodic loss potentials.

Danilov and Tade (2009) studied the influence of Ni-YSZ anode flow field designs and kinetics using multi-step reactions for internal reforming, water gas shift reaction and electrochemical reactions on planar SOFC performance. The main function of the anode flow field was to supply the fuel which was a mixture of pre-reformed methane and water to the anode and to remove the reactants from the anode. As Zhu et al. (2005) and Janardhanan and Deutschmann (2006), the electrochemical reaction were assumed to occur only at the catalyst/electrolyte interface. The multi-step heterogeneous reaction mechanism for the methane reforming and water gas shift reaction were taken from Zhu et al. (2005). The global electrochemical reactions were described by Butler-Volmer equation. They considered both H_2 and CO for the electrochemical reactions. This 3D model was able to predict the cell performance, temperature and concentration profiles. However, the governing equations in the model including conservation of mass, momentum and energy were considered only on the anode side. This model was not validated with experimental data.

Hofmann et al. (2009) developed a 2D YSZ electrolyte supported planar cell model to compare the SOFC performance by considering a detailed heterogeneous reaction mechanism (methane reforming and water gas shift reaction) with global kinetic rate. From the simulation result, they found that considering detailed heterogeneous reaction mechanism gives lower reforming rate than with their global kinetics which contributes to lower SOFC power output and electrical efficiency. Hofmann et al. (2009) also assumed that the electrochemical reactions (described by Butler-Volmer equation) took place at the electrode/electrolyte interface. The model was not validated with experimental data.

Hofmann and Panopoulos (2010) developed 1D, 2D and 3D anode supported planar cell models by considering a detailed heterogeneous reaction mechanism (methane reforming and water gas shift reaction). They used the modified Butler-Volmer equation developed by Zhu et al. (2005) to represent the electrochemical reaction. As Hofmann et al. (2009), they assumed that the electrochemical reactions took place at the electrode/electrolyte interface and only H_2 oxidation was involved at the anode. However in these models, they include

multi-components gas diffusion mechanisms using Dusty-Gas model. The main improvement in these models is that they included electrochemical impedance spectroscopy simulation (EIS). However the models were not validated with experimental data.

Ni et al. (2007) developed a 1D model to investigate the effect of particle size and porosity of graded anode on the performance of a SOFC supplied with H_2 gas. This model only considered the Ni-YSZ anode in the model geometry. In the graded anode, the microstructure of the anode varied along the anode depth. Both the particle size graded and porosity graded SOFC anode gave better performance compared to non-graded anode. However, the particle size graded anode gave more promising results in terms of reducing the total overpotential due to decrease in H_2 mass transport resistance and increase reactive surface area of the electrochemical reaction close to the electrode/electrolyte interface. They used a Butler-Volmer equation for the electrochemical reactions and considered that the electrochemical reaction occurs throughout the anode. The model was not validated with experimental data.

Ni et al. (2009) later improved their model by considering CH_4 as SOFC feed with direct internal methane steam reforming and water gas shift reaction using global kinetics. In this model, they included all cell components (anode, cathode and electrolyte), contrary to their previous model where they only considered the anode in the model geometry. They assumed that the electrochemical reactions occur only at the electrode/electrolyte interface where the charge transfer kinetics are represented by Butler-Volmer equation. At the anode, they assumed that only H_2 is involved in the electrochemical reaction. The model was used to analyse transport characteristics, chemical and electrochemical reaction kinetics and various overpotentials under different electrode microstructures including electrode porosity, pore size and functionally graded electrode. The purpose of the graded electrode is to reduce both the concentration and activation overpotentials in the electrode since the electrode microstructure has opposite effects on these overpotentials. In order to reduce the activation overpotential, large TPB is required whereas low electrode porosity and small electrode pore size are needed. However, to reduce the concentration overpotential, high porosity and large

pore size are desired. Compared to non-graded electrode, the performance of the porosity graded electrode increased by 7%, while for the pore size graded electrode, the performance increased by 5.6%. The model was validated using some experimental data available in the literature and the predicted performances agreed well with the literature data.

Hussain et al. (2006) modelled an anode composed of a homogeneous material by distinguishing two layers: a reaction layer where all mass transport, electronic and ionic transports occur simultaneously, and a backing layer where there is no ionic transport. The thickness of these layers were somewhat arbitrary. The model agreed well with literature data. Later, Hussain et al. (2009) improved their modelling by considering the whole anode as a reaction layer. However, in this model they only considered anode as a model geometry. Both chemical and electrochemical reactions were modeled as global reactions. They found that the actual reaction layer where oxygen ions are present varies with operating parameters; for example, it increases as the temperature increases. However, the results of their more recent paper were not validated with any experimental data.

Zhu and Kee (2008) improved their earlier model (Zhu et al., 2005) model for a SOFC with mixed ionic and electronic conducting composite electrode by considering distributed charge transfer in electrode assemblies. Distributed charge transfer means that the electrochemical reactions do not occur only at the electrode/electrolyte interface, but take place over a few tens of micrometers from the electrolyte. The anode consists of two layers which are a thin (tens of micrometer) active layer and a thick (order of a millimeter) conduction layer. Both layers have the same composition of material (Ni/YSZ) but the support layer has larger particle and pore size to facilitate gas transport. As in their previous study the model still assumed that only H_2 is electrochemically active. The model was not validated using experimental data. Later, in 2011 Zhu and Kee improved their model into a 2D model with different cell geometry which is segmented-in-series cell. This model was also not validated using experimental data.

Li et al. (2010) developed a 1D anode supported button cell model operating with syngas. In this model they incorporated elementary water gas shift reaction and elementary anodic heterogeneous reaction. However the diffusion of adsorbed species was neglected. They considered both H_2 and CO involved in the electrochemical reactions and its occurrence throughout the electrolyte. The objective of this study was to evaluate the effect of operating temperatures (750-850^oC) and operating voltage on cell polarization, performance and species concentration distribution in the anode and carbon deposition. They found that higher temperature and lower operation voltage can reduce carbon deposition on the Ni surface. The model was validated with experimental data.

Farhad and Hamdullahpur (2012) modelled an anode-supported planar SOFC with a range of micro-/nano-structures of porous composite electrodes. The anode consisted of a thick substrate layer and a thin functional layer where electrochemical reactions take place. The model considered biogas fuel. The objective of their work was to study the effects of the electrode micro-/nano-structure (e.g. volume fractions, Ni and LSM sizes, porosity, thickness) on the polarization resistance. The most important parameters were found to be Ni volume fraction and Ni size in the anode functional layer, thickness of the anode functional layer, and porosity of the anode substrate layer. The simulation results were not validated with any experimental data.

Modelling studies on SDC electrolyte based SOFC

Cui et al. (2010) developed a 2D anode supported button cell model where they considered the electrochemical reactions occurring throughout the electrode. The objective of this study was to evaluate the effect of operating conditions and cell geometry on the current efficiency of SOFC with ceria-based electrolytes. The model used humidified H_2 as the fuel and the Butler-Volmer equation was used to represent the H_2 oxidation reaction. Fick's law was used to model the mass transport in the electrodes where both the Knudsen and molecular diffusion were taken into account in the effective diffusion coefficient calculation. The model was validated with the experimental data.

In conclusion, although many SOFC modelling studies assumed that the electrochemical reaction occurred at the electrode/electrolyte interface and it worked well in many circumstances, it is important to note that in reality, electrochemical reactions are taking place at the TPB where the ionic conductor, electronic conductor and gases meet. From the literature review it is clear that almost all the models were conducted for Ni/YSZ anode material at temperatures above 800°C. Only one paper dealing with Ni/SDC anode at lower temperatures was found. Some key features of models previously described are summarized in Table 2.3.

Table 2.3: Summary of various key SOFC model developments

Modelling studies on YSZ electrolyte based SOFC				
Authors	**Design Type**	**Fuel**	**Approach in Modelling**	**Model Limitations**
Shi et al. (2007)	2D anode supported button cell	H_2/H_2O mixture	▪ Use Stefan Maxwell model for diffusion in porous media ▪ Use Butler-Volmer equation for electrochemical reactions ▪ Considered ohmic, concentration and activation overpotentials	▪ The model is only valid for humidified hydrogen fuel ▪ Do not include fuel and air channels
Suwanwarangkul et al. (2006)	2D electrolyte supported button cell	H_2, CO, H_2O,CO_2 and N_2	▪ Use Dusty Gas model for diffusion in porous media ▪ Use Butler-Volmer equation for electrochemical reactions ▪ Considered activation and electrolyte ohmic overpotentials	▪ Assumed the electrochemical reaction and water gas shift reaction only occurred at the electrode/electrolyte interface ▪ Electrodes subdomains are ignored in the model ▪ Simulation result deviated from the experimental data for the operating temperature at 800^oC
Zhu et al. (2005)	1D anode supported planar cell	CH_4, H_2 and CO	▪ Use Dusty Gas model for diffusion in porous media ▪ Use modified Butler-Volmer equation for electrochemical reactions ▪ Considered activation and ohmic overpotentials	▪ Considered H_2 is the only electrochemical active fuel species ▪ Assumed the electrochemical reaction only occurred at the electrode/electrolyte interface ▪ Model with the condition where coking occurred is still not yet validated.
Janardhanan and Deutschmann (2006)	2D anode supported button cell	CH_4 and 3% H_2O	▪ Use Dusty Gas model for diffusion in porous media ▪ Use modified Butler-Volmer equation for electrochemical reactions ▪ Considered activation and ohmic	▪ Considered H_2 is the only electrochemical active fuel species ▪ Assumed the electrochemical reaction only occurred at the electrode/electrolyte interface ▪ Model prediction was not in good

Modelling studies on YSZ electrolyte based SOFC				
Authors	**Design Type**	**Fuel**	**Approach in Modelling**	**Model Limitations**
			overpotentials	agreement with experimental results for open circuit potential ▪ No experimental findings to validate anodic loss potential
Danilov and Tade (2009)	3D anode supported planar cell	H_2, CO, CO_2	▪ Use Butler-Volmer equation for electrochemical reactions ▪ Considered activation and ohmic overpotentials	▪ Assumed the electrochemical reaction only occurred at the electrode/electrolyte interface ▪ Considered momentum, mass and energy transfer processes only on anode side ▪ This model is not validated with experimental data
Hofmann et al. (2009)	2D electrolyte supported planar cell	CH_4	▪ Use Butler-Volmer equation for electrochemical reactions ▪ Considered activation and ohmic overpotentials	▪ Considered H_2 is the only electrochemical active fuel species ▪ Assumed the electrochemical reaction only occurred at the electrode/electrolyte interface ▪ Anode and cathode were treated as non-porous media ▪ This model is not validated with experimental data
Hofmann and Panopoulos (2010)	1D, 2D and 3D anode supported planar cell	CH_4, H_2 and CO	▪ Use Dusty Gas model for diffusion in porous media ▪ Use Butler-Volmer equation for electrochemical reactions ▪ Considered activation and ohmic overpotentials	▪ Considered H_2 is the only electrochemical active fuel species ▪ Assumed the electrochemical reaction only occurred at the electrode/electrolyte interface ▪ This model is not validated with experimental data
Ni et al. (2007)	1D model	H_2	▪ Use Dusty Gas model for diffusion in porous media	▪ Only considered anode in the model ▪ This model is not validated with experimental data

Modelling studies on YSZ electrolyte based SOFC				
Authors	**Design Type**	**Fuel**	**Approach in Modelling**	**Model Limitations**
			▪ Use Butler-Volmer equation for electrochemical reactions ▪ Considered activation and concentration overpotentials	
Ni et al. (2009)	1D anode supported cell	CH_4	▪ Use Dusty Gas model for diffusion in porous media ▪ Use Butler-Volmer equation for electrochemical reactions ▪ Considered activation and concentration and ohmic overpotentials	▪ Do not considered multi-step reaction mechanism ▪ Considered H_2 is the only electrochemical active fuel species ▪ Assumed the electrochemical reaction only occurred at the electrode/electrolyte interface
Hussain et al.(2009)	2D anode supported planar	CH_4,CO, CO_2, H_2 and H_2O	▪ Use Stefan Maxwell model for diffusion in porous media ▪ Use Butler-Volmer equation for electrochemical reactions ▪ Considered ohmic, concentration and activation overpotentials	▪ Do not considered multi-step reaction mechanism ▪ Considered H_2 is the only electrochemical active fuel species ▪ Only considered anode as a model geometry ▪ This model is not validated with experimental data
Zhu and Kee (2008)	1D anode supported button Cell	CH_4 and H_2O	▪ Use Dusty Gas model for diffusion in porous media ▪ Use modified Butler-Volmer equation for electrochemical reactions ▪ Considered activation and ohmic overpotentials	▪ Considered H_2 is the only electrochemical active fuel species ▪ This model is not validated with experimental data
Zhu and Kee (2011)	2D segmented-in-series cell	CH_4, CO, CO_2, H_2 and H_2O	▪ Use Dusty Gas model for diffusion in porous media ▪ Use modified Butler-Volmer equation for electrochemical reactions	▪ Considered H_2 is the only electrochemical active fuel species ▪ This model is not validated with experimental data

Modelling studies on YSZ electrolyte based SOFC				
Authors	**Design Type**	**Fuel**	**Approach in Modelling**	**Model Limitations**
			▪ Considered activation and ohmic overpotentials	
Li at al. (2010)	1D anode supported button cell	H_2, CO, CO_2, H_2O	▪ Use Fick's law for diffusion in porous media ▪ Use Faraday's law for electrochemical reactions	▪ Elementary electrochemical reaction is assumed to occurs only on Ni surface ▪ Diffusion of adsorbed species are negligible.
Farhad and Hamdullahpur. (2012)	2D anode supported planar cell	Biogas	▪ Use Butler-Volmer equation for electrochemical reactions ▪ Considered ohmic, concentration and activation overpotentials	▪ This model is not validated with experimental data

Modelling studies on SDC electrolyte based SOFC				
Authors	**Design Type**	**Fuel**	**Approach in Modelling**	**Model Limitations**
Cui et al. (2010)	2D anode supported button cell	H_2 and H_2O	▪ Use Fick's law for diffusion in porous media ▪ Use Butler-Volmer equation for electrochemical reactions ▪ Considered ohmic overpotentials	▪ Do not include fuel and air channels

Chapter 3
Experimental - Apparatus and Procedures

This section describes the experimental techniques for the material preparation and evaluation of Ni-SDC and Ni-YSZ catalysts for methane steam reforming reaction as well as evaluation of SDC and YSZ support materials for the reverse water gas shift reaction.

Experimental data for model validation in Chapter 6 were generated by Miss Asmida Ideris (PhD student at University of Waterloo). The detail description of SOFC button cell setup and measurement procedures can be found in Phongaksorn (2010) and Yan et al. (2012).

3.1 Material Preparation

3.1.1 Material Preparation for Methane Steam Reforming (MSR) Experimental Work

NiOH (nickel hydroxide) powder was prepared using a co-precipitation method from a solution containing 0.2M of $Ni(NO_3)_2.6H_2O$ (nickel nitrate). This solution was added drop-wise into a 30% NH_4OH (ammonia) solution under stirring to precipitate the NiOH. Additional NH_4OH solution was added simultaneously to keep the pH constant at 9. The solution was then stirred for 30 minutes in a closed system and the resulting precipitate was aged for 24 h at room temperature. The solid cake was washed and filtered with distilled water several times until pH reached ~7 to remove residual nitrate. The filter cake was then dried at 115°C overnight. Finally, the precipitate in the form of metal hydroxide was transformed into a metal oxide form by calcination in air at 750°C for 4 h. The procedure for the material preparation is summarized in Figure 3.1.

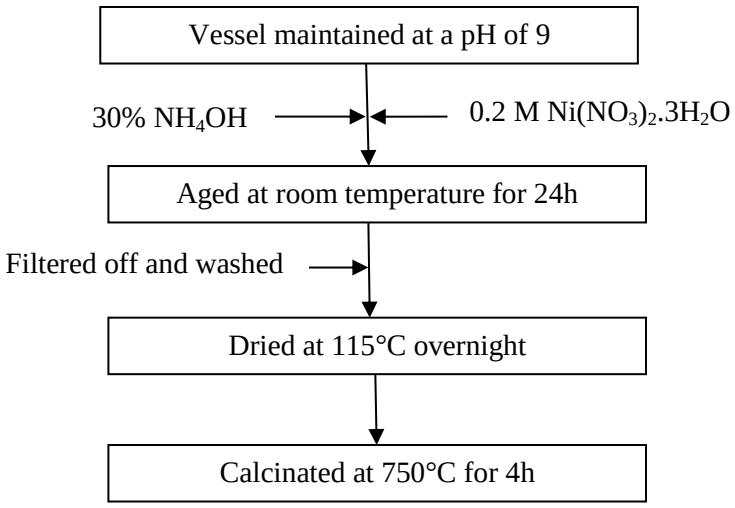

Figure 3.1: Procedure for preparing NiO powder

The NiO powder was then mixed with SDC or YSZ powder with a ratio 50/50 (per weight) and ball milled for one hour. The powder mixture was then pressed and sieved (100 mesh) to form pellets of dimension 150 μm.

3.1.2 Material Preparation for Reverse Water Gas Shift (RWGS) Reaction Experimental Work

For reverse water gas shift reaction experimental work, commercial SDC and YSZ powders were pressed and sieved to form pellets of dimension 150 μm.

3.2 Fixed Bed Reactor for Catalyst Performance Experiments

The activity of Ni-YSZ and Ni-SDC for methane steam reforming and the activity of SDC and YSZ for reverse water gas shift reaction were evaluated using a fully automated fixed-bed reactor. The overview of the fixed bed system and experimental procedures are explained below:

Overview of the fixed bed system:

A fully automated fixed-bed reactor with online gas analysis of the product stream was employed for catalyst performance evaluation experiments. A schematic of the fixed-bed

reactor catalyst test station used in this study is given in Figure 3.2. The fixed bed reactor catalyst test station consists of six main parts:

1) Gas manifold and liquid delivery system
2) Pre (including steam generation) and post reactor heated sections
3) High temperature furnace
4) Quartz tube fixed bed reactor
5) Data acquisition and process control
6) Product gas analysis system

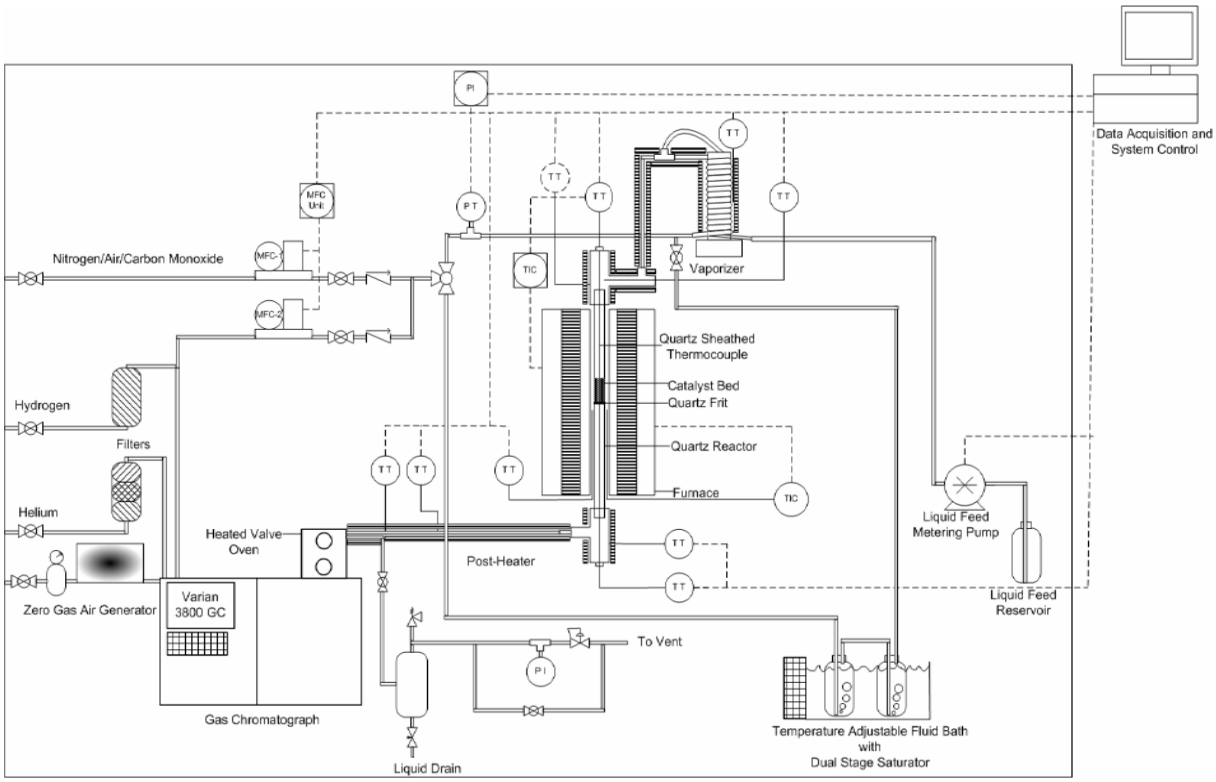

Figure 3.2: Catalysis activity test station

The feed gases were supplied from gas cylinders and their flow rates were metered and controlled by UNIT 1100 mass-flow controllers (MFCs). Six heated sections (vaporizer, pre-reactor heater, three post-reactor heaters, and a GC sample line heater) were maintained at approximately 200°C to ensure that the vaporized reactant feed mixture entering the reactor

and the product stream exiting the reactor remained gaseous. The temperature of the Lindberg Blue 2000 W furnace was controlled by a LabView control program using a quartz-sheathed micro K-type thermocouple located in the middle of the catalyst bed. Methane steam reforming experiments were performed in a down-flow fixed bed quartz tube reactor. Quartz was selected as a material of construction because of its inert chemical structure and inactivity towards the reforming reactions. The schematic diagram of the quartz tube reactor is shown in Figure 3.3. A National Instrument Field Point measurement, data logging, and process control system in combination with LabView process control program was used to control the process and to collect and store critical process information (e.g., reactant flow rate, total reactor pressure, catalyst bed temperature, and temperature of each controlled section).

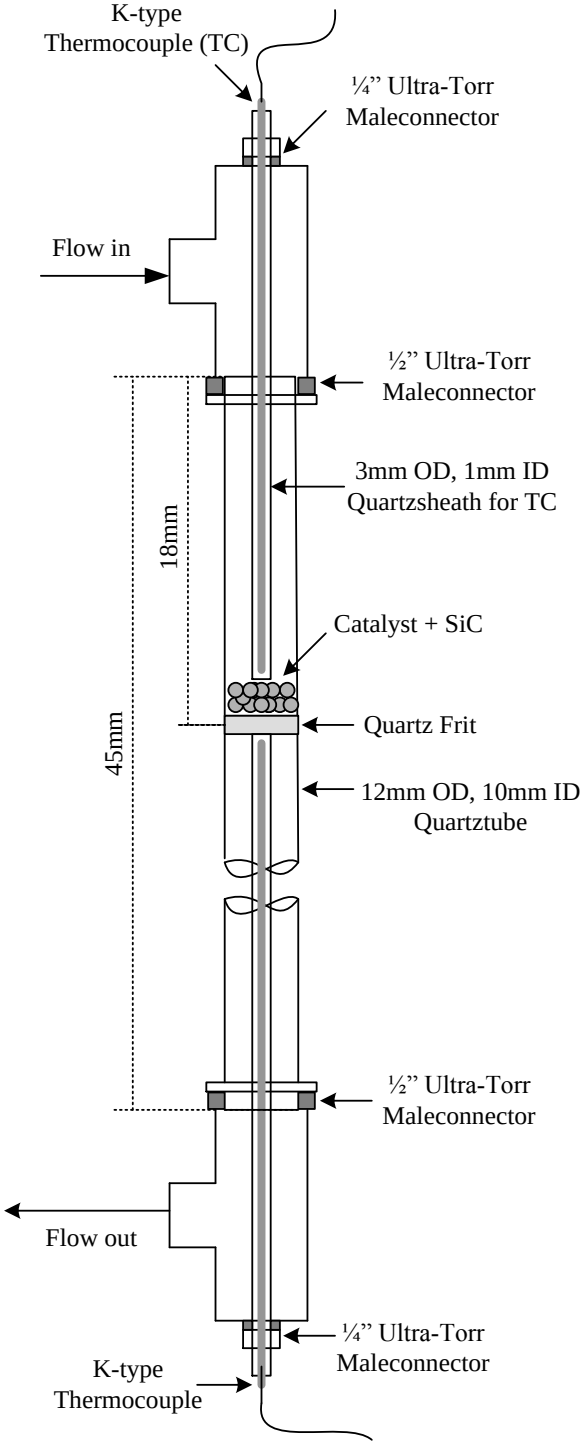

Figure 3.3: Quartz tube reactor

Procedure and Data Analysis for MSR:

Water was fed by a liquid pump at a constant rate to the vaporizer which was maintained at 175°C to ensure vaporization of the water. Methane, eventually diluted with nitrogen, metered by a Unit 1100 mass flow controller was mixed with the vaporized water. N_2 was fed as an internal standard to aid in analysis of the product stream (determine the total product flow rate). The feed mixture (methane, N_2 and steam) passed through a pre-reactor heater section maintained at 200°C to prevent condensation and was delivered to the reactor. The reactor consisted of a 10 mm I.D quartz tube with a porous quartz fritz on which sat 60 mg of catalyst dispersed in 160 mg of SiC (silicon carbide) as inert. The SiC was used to maintain a bed temperature as constant and homogeneous as possible. The temperature of the catalyst bed was measured by a quartz sheathed micro thermocouple located in the middle of the catalyst bed which was also used to control the furnace temperature. This arrangement ensured that the average temperature of the bed was maintained at the desired reaction temperature. The product stream exiting the reactor passed through a series of heated systems (post-heaters) which were maintained at 200°C to ensure the product stream remained gaseous. Finally, the product gas entered a Varian CP3800 Gas Chromatograph for product composition analysis.

The activity and selectivity of the Ni-SDC and Ni-YSZ catalysts for the methane steam reforming reaction were evaluated and compared using the parameters defined in Table 3.1.

Table 3.1: Methane steam reforming evaluation parameters

Parameter	Formula	Definitions
Methane Conversion	$X_{CH_4} = \frac{n_{CH_4}^{in} - n_{CH_4}^{out}}{n_{CH_4}^{in}}.100$	$n_{CH_4}^{in}, n_{CH_4}^{out}$: Molar flow rate of methane entering and exiting the reactor
Product yield (of species i)	$Y_i = \frac{n_i^{out}}{n_{CH_4}^{in} X_{CH_4}}$	n_i^{out}: Molar flow rate of species i exiting reactor
Carbon balance	$C_{Bal} = \frac{\sum \chi_i n_i^{out}}{n_{CH_4}^{in}}.100$	χ_i : represent the number of carbon atoms in molecule i (χ_{CH_4}= 1). Note: All carbonaceous species exiting the reactor, including unconverted methane, are included in the numerator term.

The experimental results (methane conversion and H_2 and CO yields) were compared with the predicted thermodynamic equilibrium values using Gibbs' equilibrium reactor in Aspen Plus.

Procedure and Data Analysis for the RWGS reaction:

RWGS reaction experiments were carried out in a fixed bed reactor as discussed in section 3.2. The activity of SDC and YSZ toward the reverse water gas shift reaction was evaluated at three different CO_2/H_2 ratios which were 1:1, 1:3 and 1:4. For each experiment the flow rate of CO_2 was kept constant at 15 ml/min while the H_2 flow rate was varied depending on the CO_2/H_2 ratios. N_2 was also added in the feed mixture as an internal standard to aid in analysis of the product stream. The amount of SDC and YSZ used were 60 mg for each experiment and dispersed in 160 mg of SiC (silicon carbide) as inert. The amount of N_2 was varied to kept the gas hourly space velocity constant at 70 h^{-1}. For each ratio, the reverse water gas shift reaction was conducted at three different temperatures which were 650, 700 and 750°C. The product gas streams were analyzed using an online gas chromatograph where the catalyst activity was evaluated every 30 minutes. The activity of SDC and YSZ on

RWGS reaction was evaluated and compared using carbon dioxide conversion (see Table 3.1).

Procedure for RWGS reaction kinetic study:

For the RWGS kinetic study, all kinetics experiments were also performed in fixed bed reactor. In this set of experiments, SDC and YSZ particulates with diameters of 210 μm and total flow rate of 287 ml/min were used. All experiments were carried out using a constant GHSV of 640 h^{-1}. This was accomplished by varying the amount of catalyst, depending on the composition of the feed flow rate. The experiments were performed at temperatures of 650, 700, 750 and 800°C. At each temperature, 28 experiments with various feed compositions (mostly in variation of H_2 and CO_2) were considered.

Table 3.2: RWGS evaluation parameters

Parameter	Formula	Definitions
Carbon dioxide conversion	$X_{CO_2} = \frac{n_{CO_2}^{in} - n_{CO_2}^{out}}{n_{CO_2}^{in}} . 100$	$n_{CO_2}^{in}, n_{CO_2}^{out}$: Molar flow rate of carbon dioxide entering and exiting the reactor

3.3 SOFC Button cell Electrochemical Performance Measurement

Material Preparation:

In this work, SDC ($Ce_{0.8}Sm_{0.2}O_{1.9}$) and NiO powders were synthesized using glycine-nitrate process (GNP). GNP is a powder synthesis route involving combustion reaction where glycine and metal nitrates act as fuel and oxidizers, respectively. It is a rapid self-combustion method which produces homogenous nano-sized powders with low carbon residue (Chick *et al.,* 1990). The main reason GNP was chosen for this work is due to its highly porous, foam-like structure powders that have a very low fill density. This morphology is favorable for a successful fabrication of thin film electrolyte on a porous electrode via the dry-pressing technique (Xia and Liu, 2001). GNP managed to provide fine electrolyte powders which exhibit high relative density and excellent conductivity after sintering (Peng *et al.,* 2004).

Button Cell Fabrication:

An NiO/SDC button cell consists of NiO/SDC anode, SDC electrolyte and SSC/SDC cathode. NiO/SDC anode is composed of NiO:SDC = 55:45 ratio by weight. 5wt% of polyvinyl-butyral was added as a binder and 5wt% of di-octyl phthalate was used as a plasticizer. In the SSC/SDC cathode preparation, a commercially purchased samaria-doped strontium cobalt oxide ($Sm_{0.5}Sr_{0.5}CoO_3$) was mixed with the SDC powder at a weight ratio of SSC:SDC = 70:30. To obtain a cathode material in the form of an ink, 10 wt% isopropanol, 32.5 wt% α-terpeniol and 2.5wt% ethyl cellulose as solvent, carrier and binder, respectively were added to the powders.

Anode supported cells were fabricated using a dry-pressing technique. 1.0 g of NiO/SDC powder was weighed and pressed in a stainless steel mold at 160 MPa for 1 min using a hydraulic press to obtain a circular disk for the anode substrate. An approximately 0.0330 g of SDC powder was then carefully distributed onto the substrate and both were co-pressed at 220 MPa for 1 min. The co-pressed powders were then sintered at 1330ºC for 5 hrs to produce an anode-electrolyte bilayer with a thin film of a dense electrolyte. The bilayer was approximately 15 mm in diameter.

A cathode ink was then applied onto the middle of the bilayer at the electrolyte surface with 6 mm in diameter. A cell with a painted cathode was then sintered at 1000ºC for 2 hrs. The electrolyte-anode bilayer and NiO/SDC anode-supported cell are shown in Figure 3.4.

Figure 3.4: a) Electrolyte-anode bilayer; b) NiO/SDC anode-supported cell

SOFC Test Station:

SOFC performance measurements were conducted in a SOFC test station shown in Figure 3.5. The test station consists of gas controlling system, a humidifier, button cell, furnace and an electrochemical measurement equipment. The compositions of the fuel gases used in this work; H_2, N_2, CH_4, CO_2, and CO were adjusted by mass flow controllers connected to a LabVIEW field-point program. 3% humidified fuels were achieved by bubbling the gases through a column of water. For higher percentage of H_2O, controlled evaporator mixture (CEM) was used. A button cell was placed on the two co-axial tubes of different diameters inside a vertical tubular furnace. During the experiment, the fuel flows upward along the inner tube to the anode surface and leaves the system by flowing downward, leaving the tube to the outer stream connected to a water trap and finally to the vent. The electrochemical reactions were carried out by introducing the gas fuels and air to the anode and cathode sides, respectively, and the cell performance was monitored by electrochemical measurement device.

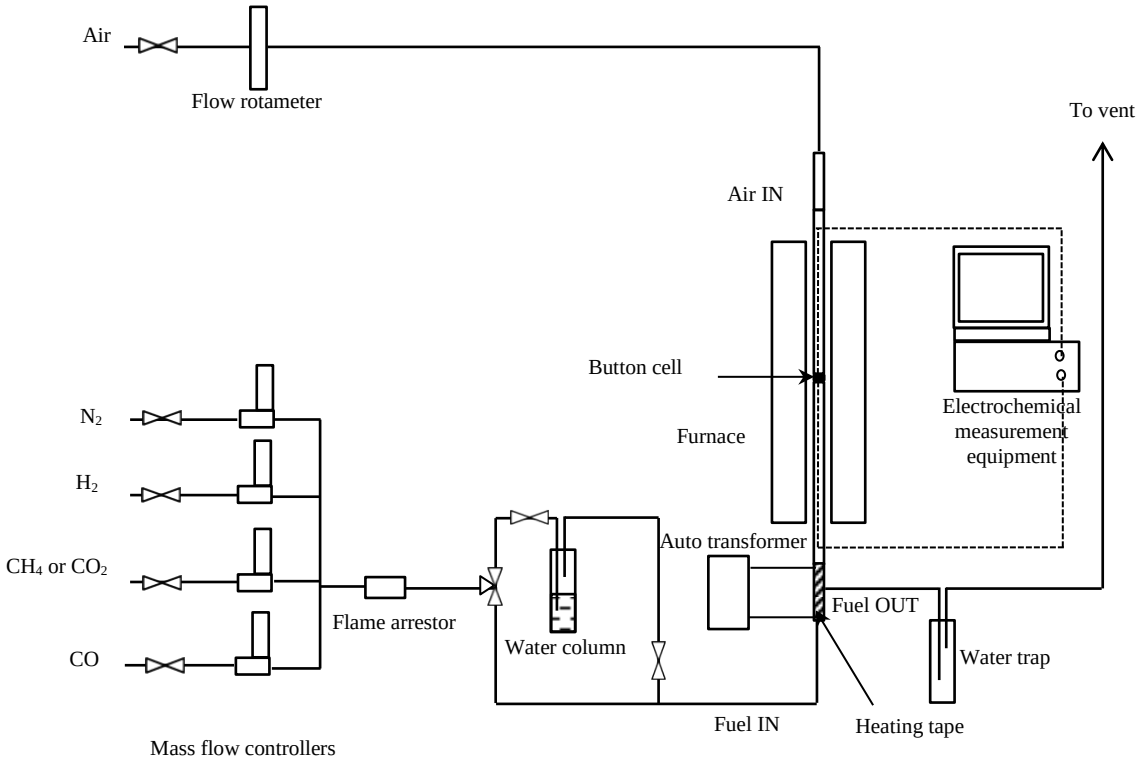

Figure 3.5: A schematic diagram of SOFC test station

Cell Setup:

A button cell was mounted on a vertical alumina tube (15 mm O.D) with a parallel quartz tube (6 mm O.D) inside. The alumina tube is responsible to hold the cell during the testing while the quartz tube supplies the fuel gases to the cell. Fuel from the quartz tube flows upward to the anode surface and leaves through a space between the quartz tube and the alumina tube. A similar arrangement was incorporated for the air supply introduced to the cathode surface. The air inlet was flowed through a quartz tube and its outlet was let to the environment. Current collectors were positioned between the quartz tube ends and the anode and cathode surfaces. The current collectors consisted of a 0.25 mm O.D silver wire and a silver mesh (50 mesh). The set-up of the cell inside the furnace is shown in Figure 3.6.

A ceramic seal was employed to seal the cell to the alumina tube. The cell was heated to its sealing temperatures (93ºC) for 2 hrs followed by heating at 260ºC for another 2 hrs. It was then further heated to 600ºC, a temperature required for the reduction step. The cell reduction was conducted once the temperature has reached 600ºC. During the reduction, NiO in the NiO/SDC cermet was converted into its active Ni metal form. The reduction was carried out at 600ºC by increasing the H_2 concentration gradually for every one hour under a humidified 10% H_2/bal. N_2 mixture for 6 hrs. The cell open circuit voltage (OCV) was monitored throughout the reduction process. For the purpose of cell stabilization before the electrochemical testing, the reduced cell was then held overnight under a humidified 10%H_2/bal.N_2 at 600ºC. After cell stabilization for approximately 18 hrs, the temperature was then adjusted to the operating temperatures (600-700°C), and the gas feed was gradually switched from the 10%H_2/bal.N_2 to 100% H_2. A total flow rate of 80 mL/min was used for the humidified H_2 and CO/CO_2 fuels. Meanwhile, the flow rate for a fuel containing CH_4 was fixed at 40 mL/min. Air was supplied into the system at a flow rate of 86 mL/min. An initial electrochemical testing was conducted under a humidified H_2 to ensure that the electrochemical tests started with a decent cell. Finally, the carbon-containing fuel was introduced into the system by slowly changing the fuel from the humidified H_2 to CO/CO_2 and syngas under a galvanostatic mode.

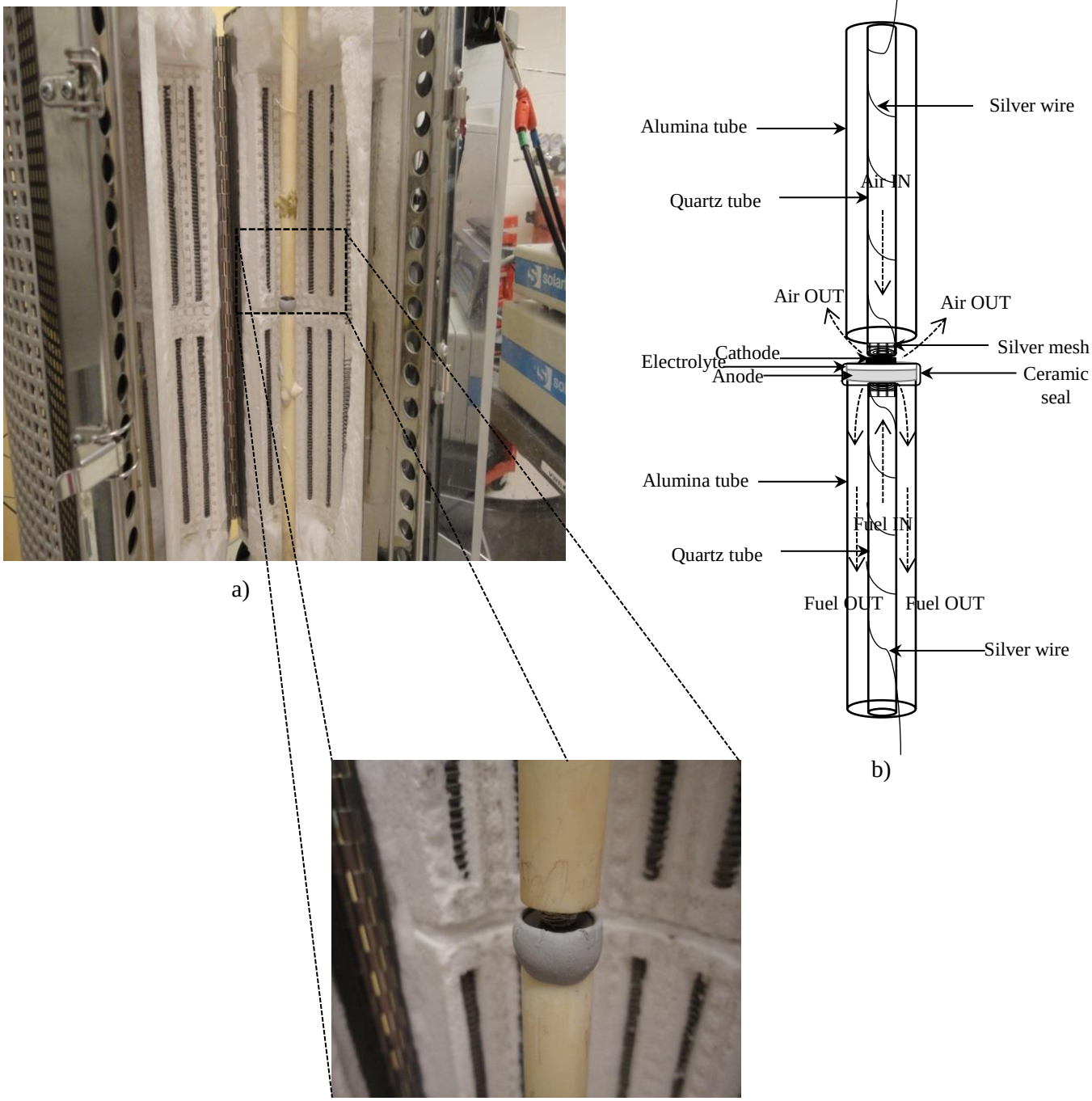

Figure 3.6: SOFC cell set-up

Cell Performance Measurement:

Cell performance was measured under potentiodynamic and galvanostatic modes using a Solartron Electrochemical Interface 1287 and Solartron Impedance Analyzer 1260 (Solartron, USA). The current-voltage (IV) curve was generated by the CorrWare software. The IV curves were obtained from the potentiodynamic using a linear sweep of 5mV/s while the galvanostatic test was performed under 100 mA/cm^2 and 350 mA/cm^2 current densities.

Chapter 4
Kinetic Study of Reverse Water Gas Shift Reaction

4.1 Introduction

Current SOFC models involving CH_4 consider only Ni as the active materials for the non-electrochemical reactions (e.g. reforming and water-gas shift reaction). To make sure this assumption is valid, experiments were carried out on a fixed bed reactor to investigate the activity of YSZ and SDC electrolytes toward methane steam reforming (MSR).

The MSR results indicated very similar low activities between the two electrolyte materials: methane conversion for the two materials varied from ~0% at 650°C to about ~2-3% at 750°C. Therefore, it was expected that methane steam reforming on Ni-YSZ and Ni-SDC should yield a similar performance. However, Ni-YSZ showed different conversion than Ni-SDC. Further analysis revealed that the H_2 yield was higher for Ni-SDC than for Ni-YSZ (the opposite trend was observed for the CO yield). These results pointed out to differences in activity toward the water-gas shift (WGS) reaction or reverse water-gas shift (RWGS) reaction, which was confirmed experimentally: for the RWGS reaction, SDC was more active than YSZ. It was, therefore, decided to conduct a comprehensive kinetic study of the reverse water-gas shift reaction on SDC to be later implemented in the SOFC button cell model.

Sections 4.2 and 4.3 discuss in details the MSR and RWGS reactions experiments, respectively. Finally, section 4.4 presents the kinetics of the RGWS reaction on SDC.

4.2 Methane Steam reforming on YSZ/Ni-YSZ and SDC/Ni-SDC

MSR experiments on electrolyte materials were conducted at 650 and 750°C, with steam to carbon (S/C) ratio of 3 for 20 h. The flow rates of CH_4(g), N_2(g) and H_2O(l) were 15 ml/min, 43 ml/min, and 0.1 ml/min, respectively. Nitrogen was added as internal standard for the GC

analysis. For each experiment, the amount of catalyst and diluent silicon carbide (SiC) used was 60 and 160 mg, respectively. SiC was used as a heat sink to minimize temperature gradient within the bed. Based only upon the catalyst mass, the flow conditions corresponded to a GHSV (gas hourly space velocity) of ~140 h^{-1}.

Methane conversion for SDC and YSZ is presented in Figure 4.1. Results for MSR over YSZ and SDC, as shown in Figure 4.1, indicated no methane conversion at 650°C and very low conversion (~2%) over both YSZ and SDC at 750°C. This figure indicates some negative conversion. This is due to the very low actual conversion and measurement errors. This negative conversion data should be regarded as an indication of no conversion.

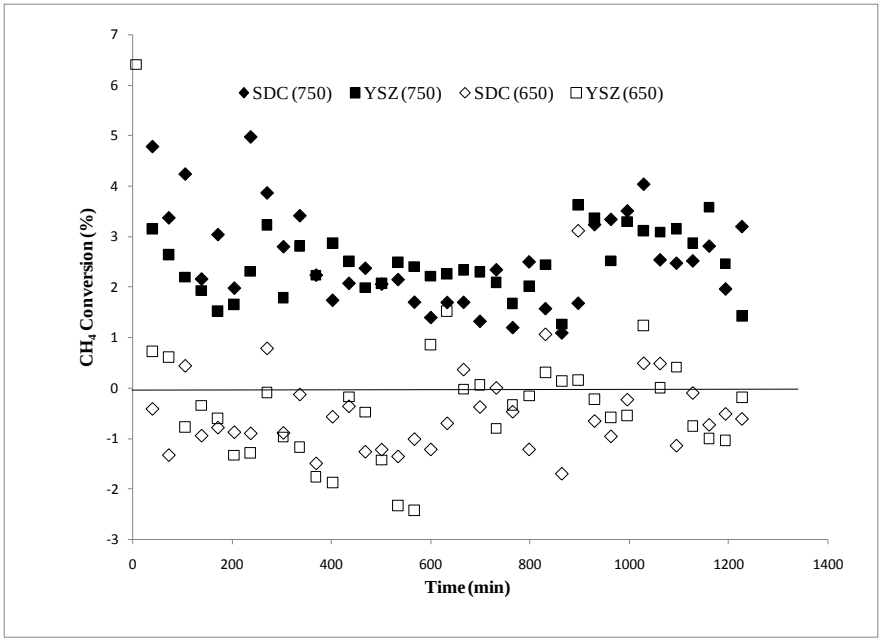

Figure 4.1: Methane conversion for SDC and YSZ at 750 and 650°C (S/C = 3, GHSV ~ 140 h^{-1})

As shown in Figure 4.1, methane conversion increases with increasing temperature from ~0% at 650°C to about ~2-3% at 750°C. One also could not observe differences between conversions over SDC and YSZ. It can then be concluded that SDC and YSZ have similar

low activity towards MSR, at least under the conditions investigated in those experiments (650-750°C, S/C =3).

From the experimental data for MSR over SDC and YSZ, it was expected that methane steam reforming on Ni-SDC and Ni-YSZ should yield a similar performance. Then, MSR experiments were conducted to evaluate Ni-SDC and Ni-YSZ activity and selectivity. MSR experiments on Ni-SDC and Ni-YSZ materials were conducted at 650, 700 and 750°C, with steam to carbon (S/C) ratio of 3 for 20 h. The flow rates of reactants and the amount of catalyst used were the same as the experimental conducted with only SDC and YSZ. Therefore, the GHSV for experiments on Ni-SDC and Ni-YSZ were also set at ~140 h^{-1}. Prior to the reaction, the NiO-SDC and NiO-YSZ catalysts were reduced in situ at 750^{o}C for 1 h with 100 ml/min of 10/90 H_2/N_2 mixture in order to reduce the metal oxide to a metal.

The results for methane conversion for MSR over Ni-SDC and Ni-YSZ are shown in Figure 4.2. Although the data is scattered, the overall trends are still clear. For most experiments, the methane conversion remains more or less constant over the 20 hours (1200 minutes) time on stream. Only the experiment conducted with Ni-SDC at 650°C showed a decrease in conversion over time. Figure 4.2 shows that the conversion decreased as the temperature decreased. Such trend is to be expected for the equilibrium conversion as MSR is an endothermic reaction.

Surprisingly, especially in light of the results from MSR on pure SDC and YSZ, at the lower temperatures (650 and 700^{o}C), differences in conversion between Ni-SDC and Ni-YSZ were observed, with conversion over Ni-SDC being lower than Ni-YSZ.

At 650°C the conversion over Ni-SDC is between 40 and 50%, whereas it is around 60% over Ni-YSZ. At 700°C, the conversion over Ni-SDC is around 65%, whereas it is on average around 80% over Ni-YSZ. However, as the temperature increases, the differences between Ni-SDC and Ni-YSZ decreases; at 750°C, methane conversions are very close for

both materials, although Ni-YSZ still shows higher activity (around 85-90%) than for Ni-SDC (around 80%).

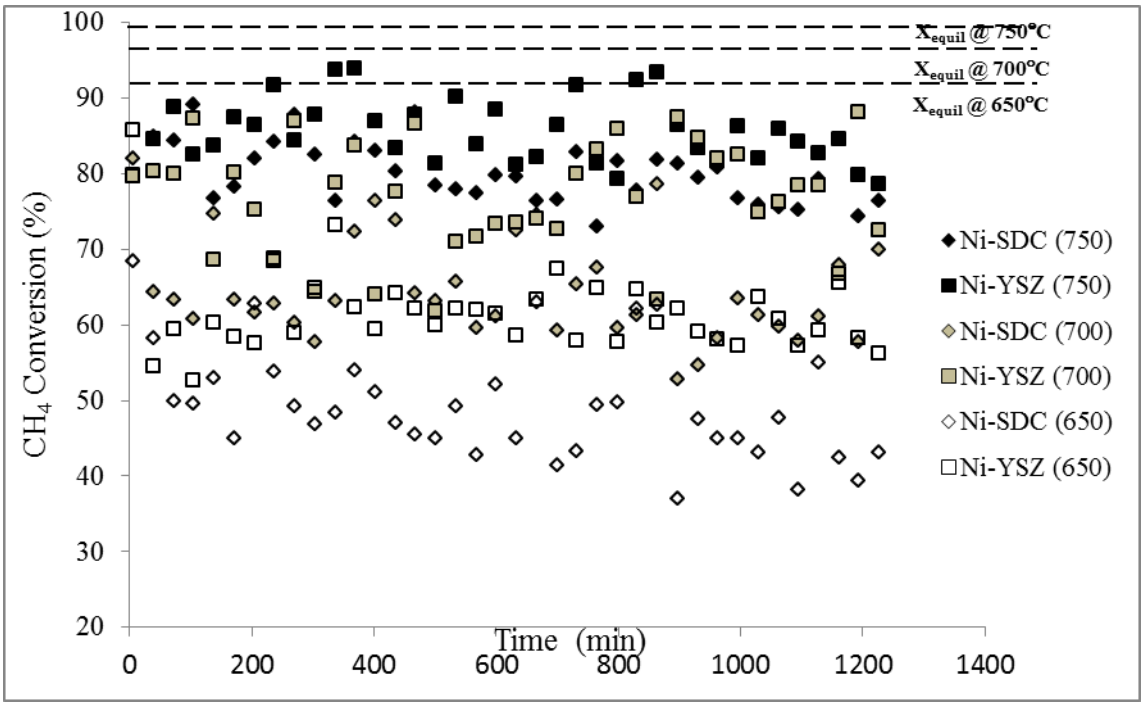

Figure 4.2: Methane conversion for Ni-SDC and Ni-YSZ catalysts at different temperatures (S/C = 3, GHSV ~ 140 h^{-1})

It was observed in Figure 4.1 that the activity of YSZ and SDC alone are low and not much different. So, the difference in reforming activity between SDC and YSZ cannot be invoked to explain the difference between Ni-YSZ and Ni-SDC activities. One possible explanation for the differences observed for the MSR activity between Ni-YSZ and Ni-SDC could be different activities over SDC and YSZ for the water gas shift reaction, which always inevitably occurs during MSR. Therefore, more attention was paid on the production of H_2 and CO during MSR over Ni-YSZ and Ni-SDC. The H_2 and CO yields are shown in Figure 4.3 and Figure 4.4, respectively.

Figure 4.3 indicates that the hydrogen yield decreases when increasing temperature. Thermodynamics also shows that the H_2 yields should decrease when increasing temperature, but in a very narrow range, from 3.5 at 650°C to 3.4 at 750°C. The experimental H_2 yields have lower values, especially at 700 and 750°C. At 750°C, the H_2 yield is only about 2.8 for both Ni-YSZ and Ni-SDC, as opposed to the thermodynamic value of 3.4. When comparing the two anode materials, the difference between their selectivity increases when lowering the temperature: at 750°C the selectivity are similar, but at lower temperatures Ni-SDC presents higher H_2 yield than Ni-YSZ and this difference is more accentuated at 650°C than at 700°C.

The CO yield (Figure 4.4) shows an opposite trend with temperature than H_2 yield: CO yield increases when increasing temperature. Thermodynamics indicates that the CO yield should be equal to 0.5 at 650°C and to 0.6 at 750°C. The experimental data shows lower CO yield than what is expected at equilibrium. The difference in CO yield between the anode materials increases as the temperature decreases, where the CO yield is higher on Ni-YSZ than on Ni-SDC.

In conclusion, the CO and H_2 yields follow opposite trends: when the temperature increases, H_2 yield decreases, but CO yield increases; H_2 yield is greater for Ni-SDC than Ni-YSZ (especially at the lower temperatures), but this is the opposite for the CO yield. This points to the effect of the water-gas shift (WGS) reaction [$CO + H_2O \rightleftharpoons CO_2 + H_2$], which could explain the opposite trend regarding the CO and H_2 yields. The WGS reaction is an exothermic reaction and thus the equilibrium is shifted to the left as the temperature increases, with the results of increasing the CO yield and decreasing the H_2 yield, as observed here. As Ni-SDC showed higher H_2 yield, this seems to indicate that SDC had a higher activity than YSZ toward the WGS reaction.

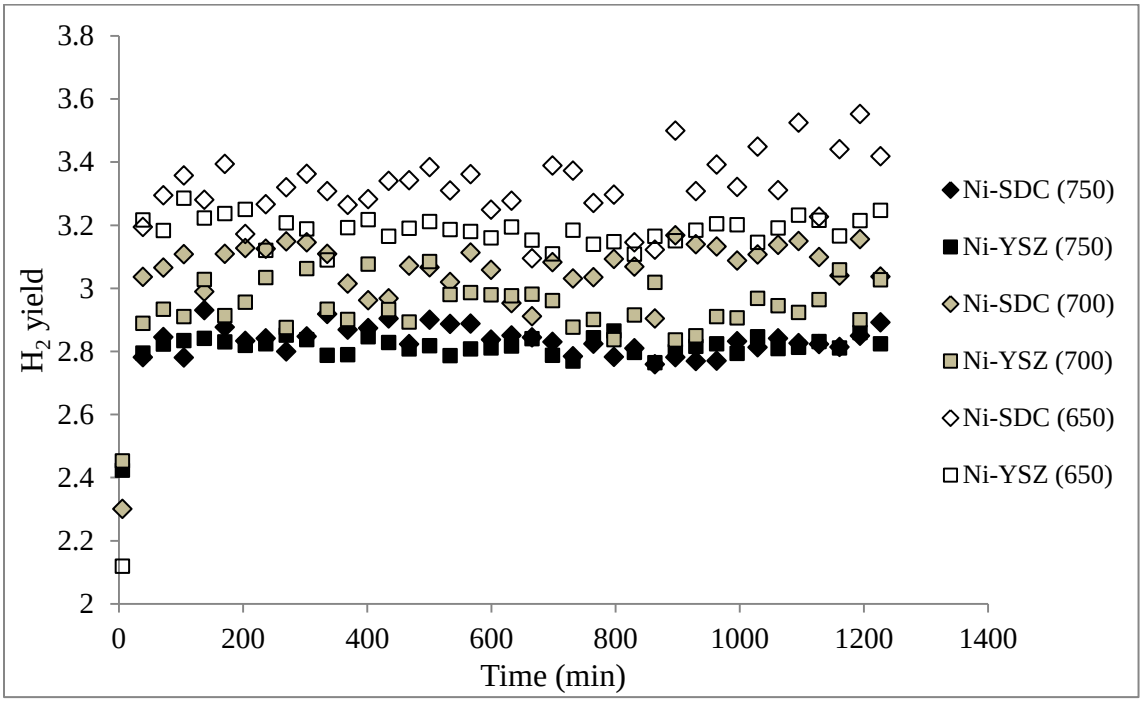

Figure 4.3: H_2 yield for Ni-YSZ and Ni-SDC at different temperatures (S/C=3; GHSV~ 140 h^{-1})

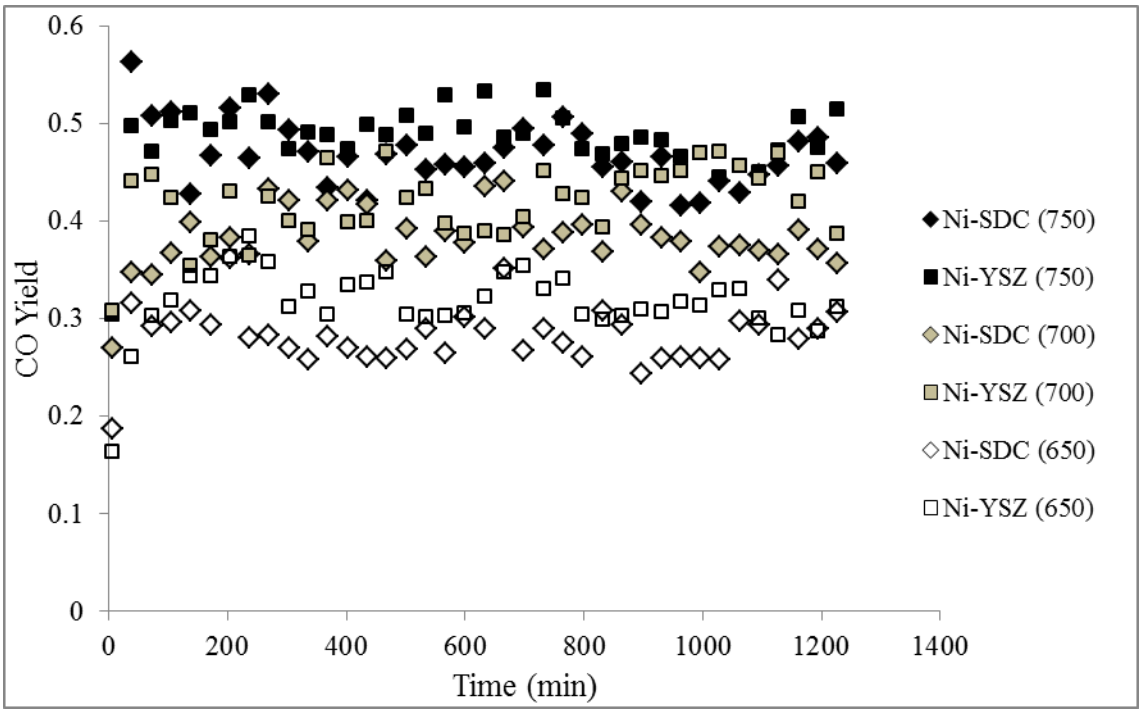

Figure 4.4: CO yield for Ni-YSZ and Ni-SDC at different temperatures (S/C= 3; GHSV~140 h^{-1})

4.3 Reverse Water Gas Shift Reaction on SDC and YSZ

To test the different activities toward WGS reactions between SDC and YSZ, reverse WGS experiments were conducted at 650, 700 and 750°C over SDC and YSZ materials in the absence of Ni catalyst at three different H_2/CO_2 ratio (1, 3 and 4) for 20 hours. It was decided to conduct experiments on the reverse WGS reaction rather than on WGS reaction because of safety (no or small amount of CO to be fed) and ease of operation (no or small amount of water to be fed). Figure 4.5 to Figure 4.7 show the CO_2 conversion of SDC and YSZ for the reverse WGS reaction at different temperatures and at different H_2/CO_2 ratios with constant GHSV (~70 h^{-1}). The results show that SDC is more active towards the reverse WGS reaction compared to YSZ at all H_2 to CO_2 ratios and temperatures, with CO_2 conversion on SDC being about 1.4-2.5 higher than CO_2 conversion on YSZ. The differences of CO_2 conversion between SDC and YSZ is summarized in Table 4.1. This result confirms the findings from the MSR experiments that a likely reason contributing to the difference of MSR activity between Ni-SDC and Ni-YSZ is due to the different WGS activity over SDC and YSZ.

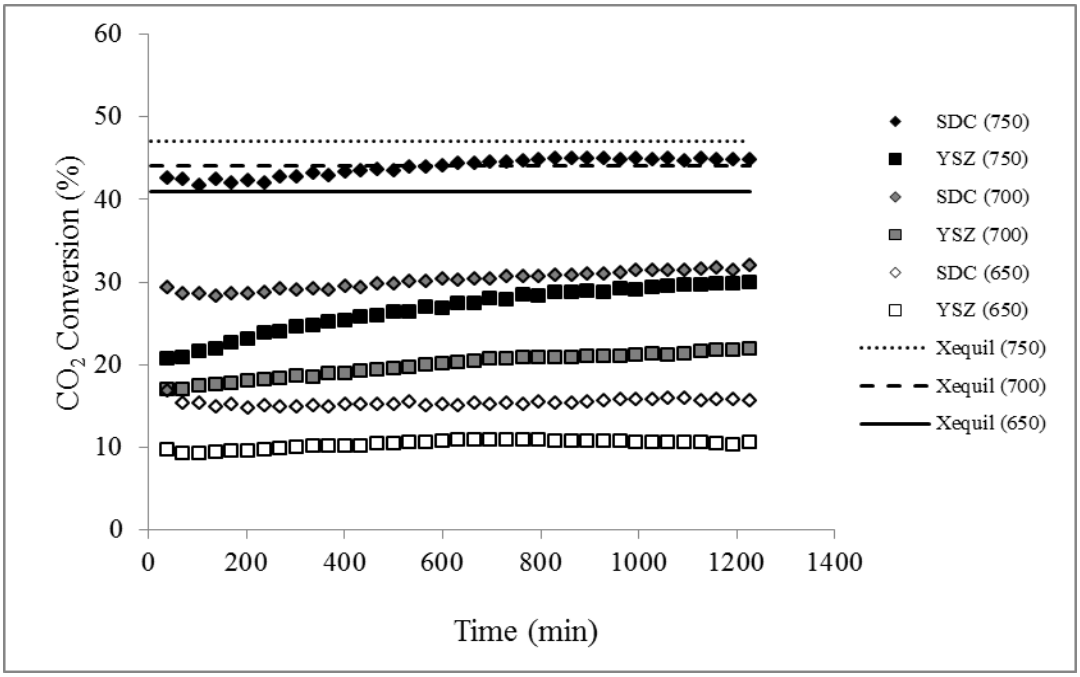

Figure 4.5: CO_2 conversion for reverse WGS reaction over SDC and YSZ at different temperatures (H_2/CO_2 = 1, GHSV ~ 70 h^{-1})

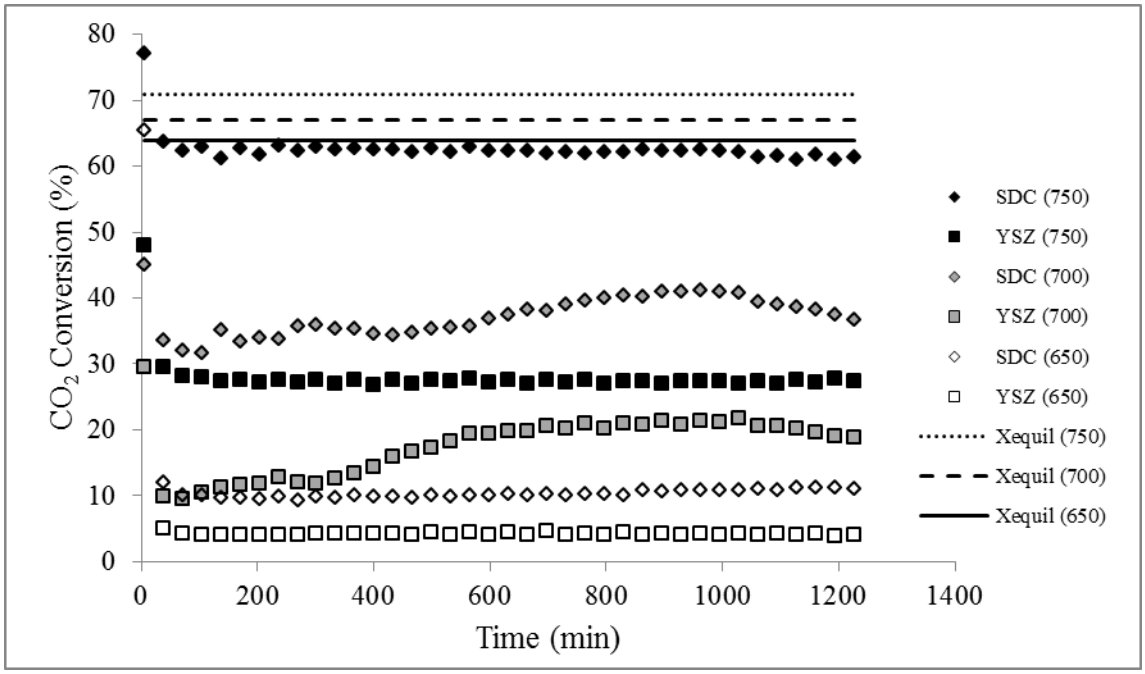

Figure 4.6: CO_2 conversion for reverse WGS reaction over SDC and YSZ at different temperatures (H_2/CO_2 = 3, GHSV ~ 70 h^{-1})

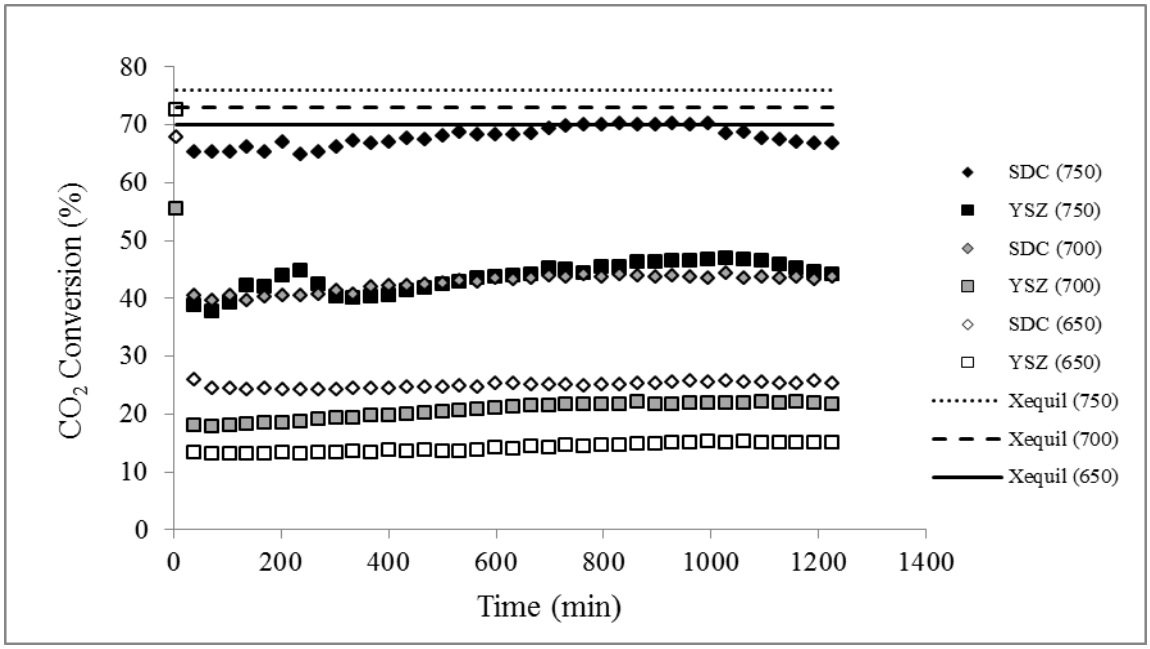

Figure 4.7: CO_2 conversion for reverse WGS reaction over SDC and YSZ at different temperatures (H_2/CO_2 = 4, GHSV ~ 70 h^{-1})

Table 4.1: Ratio of CO_2 conversion over SDC to YSZ

H_2 to CO_2 ratio	Temperature (^oC)	Ratio of CO_2 conversion over SDC to YSZ
1	750	1.5-1.7
	700	1.4-1.5
	650	1.4-1.5
3	750	2.2-2.3
	700	1.9-2.0
	650	2.4-2.5
4	750	1.5-1.6
	700	2.0-2.1
	650	1.7-1.8

Figure 4.8 and Figure 4.9 show the CO_2 conversion for reverse WGS reaction over SDC and YSZ, respectively. For YSZ, the CO_2 conversion is less than 30% for most of the conditions, except for H_2 to CO_2 ratio 4 at 750^{o}C where the CO_2 conversion is about 48%, whereas for SDC the CO_2 conversion is more than 30% for most of the conditions and can go up to 70%. In conclusion, SDC is more active towards reverse WGS reaction. This finding is in accord

with what is proposed in the literature where ceria greatly promotes the WGS reaction (Goguet et al. 2004).

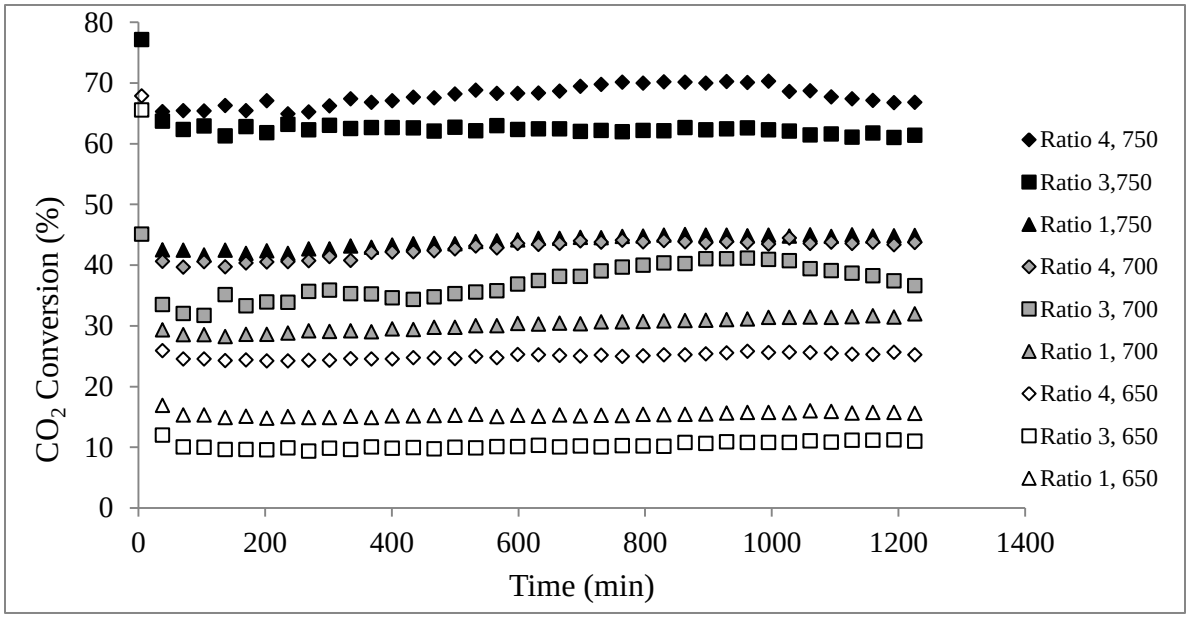

Figure 4.8: CO_2 conversion for reverse WGS reaction over SDC at different temperatures and H_2/CO_2 ratios (GHSV ~ 70 h^{-1})

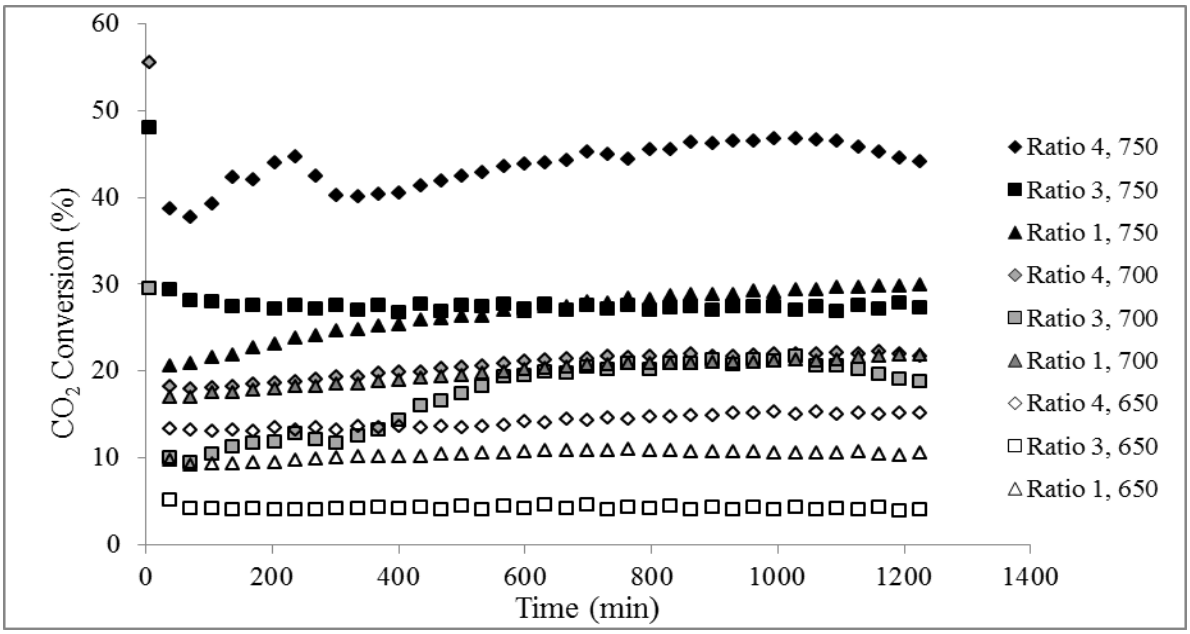

Figure 4.9: CO_2 conversion for reverse WGS reaction over YSZ at different temperatures and H_2/CO_2 ratios (GHSV ~ 70 h^{-1})

The observation about the different activities of the electrolyte material toward the WGS reaction is of importance for the modelling part. Indeed, until now, reaction schemes used in all SOFC modelling studies only took into account the reactions on nickel. In other words, such mechanisms did not take into account the nature of the electrolyte. It is, therefore, important to also take into account possible reactions (related to WGS reaction) on the electrolyte itself, especially on SDC. This was not an issue for Ni-YSZ cermet, since YSZ is not as active as SDC towards WGS. Also for the state-of-the-art high temperature SOFC (800°C or higher), it was usually admitted that the WGS rapidly reaches equilibrium. For lower temperatures it may not be the case, and SDC electrolyte materials have been developed for low to medium temperature SOFC operation. It was therefore decided to conduct a kinetic study of the reverse WGS reaction on SDC to be later implemented in the SOFC button cell model.

4.4 Kinetics of reverse Water Gas Shift Reaction on SDC

The first step of the reverse WGS reaction kinetics study was to determine experimentally the most suitable conditions to ensure that the tests were performed in the kinetically controlled regime. This involved the right selection of GHSV, particle size and amount of catalysts to ensure no diffusion limitation (internal and external), as well as conversions far from equilibrium.

Figure 4.10 shows the effect of flow rate and particle diameter on the reaction rate. As can be seen in Figure 4.10, there is no internal diffusion limitation as the reaction rates are the same for both particle diameters (210 and 300 micrometer) at temperatures 650 and 800^{o}C. The reaction rate is also independent of the gas flow rate for flow rates greater than 287 ml/min, which indicates that for flow rates greater than 287 ml/min, external limitation does not exist. Therefore, all kinetics experiments were performed with particulate diameter of 210 micrometer and a total flow rate of 287 ml/min. The amount of catalyst used in Figure 2.10 was such that for a total flow rate of 287 ml/min, it corresponds to a GHSV of 640 h^{-1}. All experiments were carried out using a constant GHSV of 640 h^{-1}. This was accomplished by varying the amount of catalyst, depending on the composition of the feed flow rate. The

experiments were performed at temperatures of 650, 700, 750 and 800°C. At each temperature, 28 experiments with various feed compositions (mostly in variation of H_2 and CO_2) were considered.

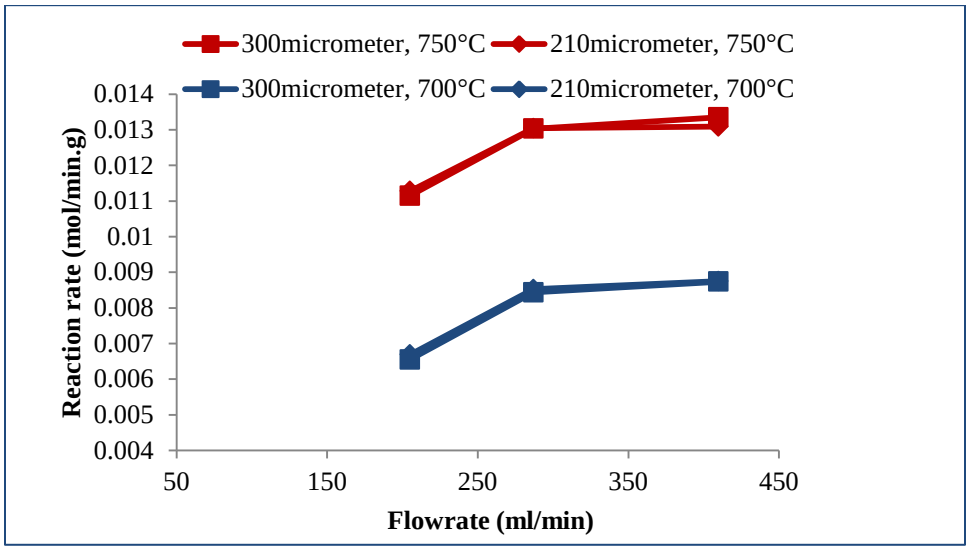

Figure 4.10: Reaction rate versus flow rate for different particle diameters at two different temperatures (CO_2/H_2=1, GHSV=640h^{-1})

It is also important to make sure that the CO_2 conversion is far from the equilibrium for this particular particle size and flow rate. As shown in

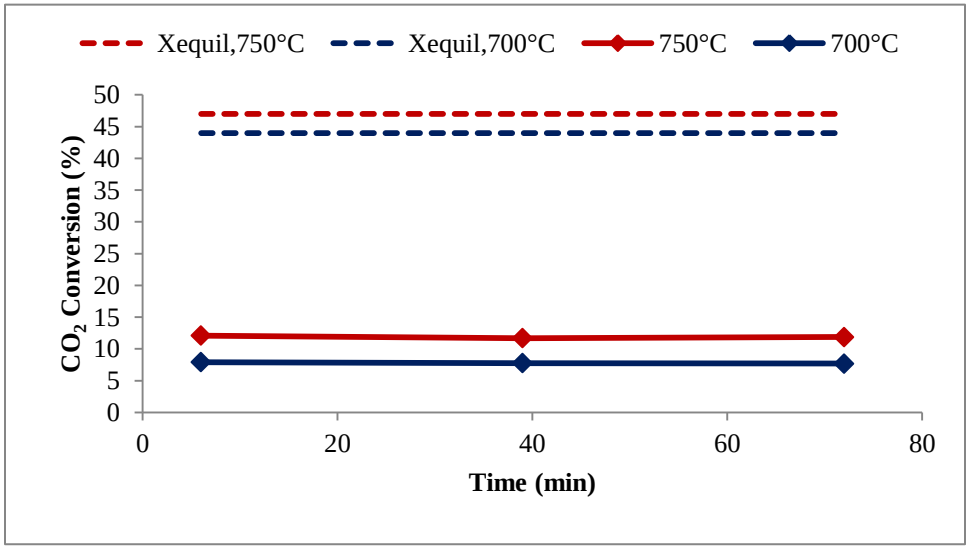

Figure 4.11, the right selection of particle size and flow rate for kinetics study were confirmed as the CO_2 conversions were far from the equilibrium conversion.

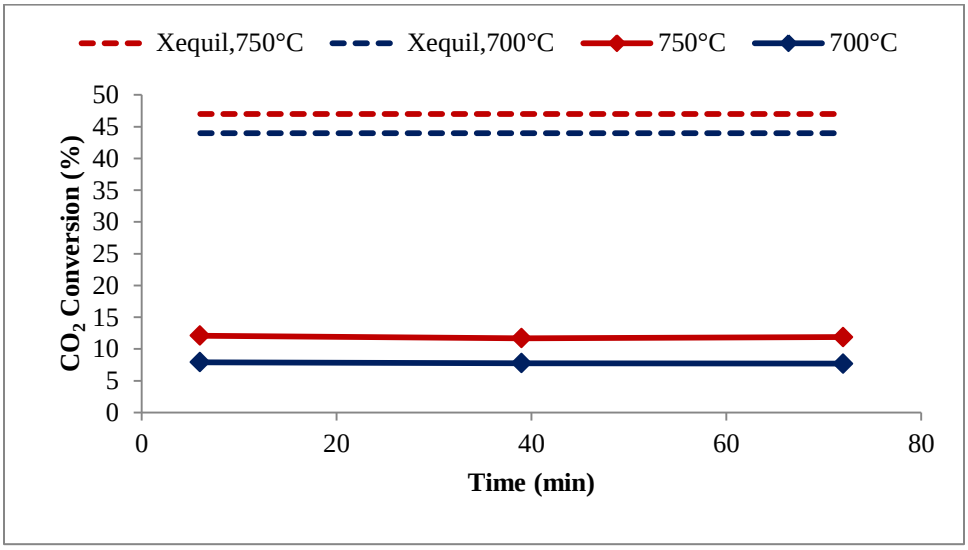

Figure 4.11: Comparison of CO_2 conversion to the equilibrium conversion at two different temperatures for particle size of 210 micrometer and flow rate of 280 ml/min (CO_2/H_2=1, GHSV=640h^{-1})

The experimental data for the kinetic study at different temperatures and different compositions of the feed flow rate is shown Table 4.2.

Table 4.2: Kinetic study experimental data

No.	T (K)	Catalyst Weight (g)	Feed mole fraction					CO_2 Conversion
			x_{H2}	x_{CO2}	x_{CO}	x_{H2O}	x_{N2}	
1	1073	0.01522	0.59	0.08	0.00	0.00	0.33	0.40249
2	1073	0.01844	0.52	0.15	0.00	0.00	0.33	0.26430
3	1073	0.02327	0.42	0.25	0.00	0.00	0.33	0.17986
4	1073	0.02714	0.33	0.33	0.00	0.00	0.33	0.16635
5	1073	0.02549	0.40	0.35	0.00	0.00	0.25	0.18208
6	1073	0.02291	0.40	0.20	0.00	0.00	0.40	0.21635
7	1073	0.02119	0.40	0.10	0.00	0.00	0.50	0.29685
8	1073	0.01997	0.40	0.03	0.00	0.00	0.56	0.48553
9	1073	0.02655	0.32	0.28	0.00	0.00	0.40	0.17485
10	1073	0.03274	0.10	0.28	0.00	0.00	0.62	0.10270
11	1073	0.03004	0.20	0.28	0.00	0.00	0.52	0.08402
12	1073	0.03127	0.20	0.35	0.00	0.00	0.45	0.07707
13	1073	0.02907	0.15	0.15	0.00	0.00	0.70	0.16452

No.	T (K)	Catalyst Weight (g)	Feed mole fraction					CO_2 Conversion
			x_{H2}	x_{CO2}	x_{CO}	x_{H2O}	x_{N2}	
14	1073	0.02636	0.20	0.07	0.00	0.00	0.73	0.35823
15	1073	0.02759	0.20	0.14	0.00	0.00	0.66	0.20048
16	1073	0.02863	0.20	0.20	0.00	0.00	0.60	0.19211
17	1073	0.03232	0.07	0.20	0.00	0.00	0.73	0.11472
18	1073	0.03033	0.14	0.20	0.00	0.00	0.66	0.12673
19	1073	0.02634	0.28	0.20	0.00	0.00	0.52	0.21353
20	1073	0.02435	0.35	0.20	0.00	0.00	0.45	0.21242
21	1073	0.03179	0.07	0.19	0.02	0.00	0.71	0.10746
22	1073	0.02756	0.20	0.20	0.03	0.00	0.57	0.17919
23	1073	0.02649	0.20	0.20	0.07	0.00	0.53	0.22406
24	1073	0.02541	0.20	0.20	0.10	0.00	0.50	0.23685
25	1073	0.03033	0.14	0.20	0.00	0.03	0.66	0.09925
26	1073	0.02863	0.20	0.20	0.00	0.03	0.60	0.10399
27	1073	0.02634	0.28	0.20	0.00	0.03	0.52	0.14488
28	1073	0.02541	0.20	0.20	0.10	0.03	0.50	0.09734
29	1023	0.01522	0.59	0.08	0.00	0.00	0.33	0.31695
30	1023	0.01844	0.52	0.15	0.00	0.00	0.33	0.19234
31	1023	0.02327	0.42	0.25	0.00	0.00	0.33	0.12687
32	1023	0.02714	0.33	0.33	0.00	0.00	0.33	0.10596
33	1023	0.02549	0.40	0.35	0.00	0.00	0.25	0.12664
34	1023	0.02291	0.40	0.20	0.00	0.00	0.40	0.13078
35	1023	0.02119	0.40	0.10	0.00	0.00	0.50	0.18973
36	1023	0.01997	0.40	0.03	0.00	0.00	0.56	0.32052
37	1023	0.02655	0.32	0.28	0.00	0.00	0.40	0.11040
38	1023	0.03274	0.10	0.28	0.00	0.00	0.62	0.05519
39	1023	0.03004	0.20	0.28	0.00	0.00	0.52	0.04199
40	1023	0.03127	0.20	0.35	0.00	0.00	0.45	0.04017
41	1023	0.02907	0.15	0.15	0.00	0.00	0.70	0.08020
42	1023	0.02636	0.20	0.07	0.00	0.00	0.73	0.23165
43	1023	0.02759	0.20	0.14	0.00	0.00	0.66	0.12837
44	1023	0.02863	0.20	0.20	0.00	0.00	0.60	0.12875
45	1023	0.03232	0.07	0.20	0.00	0.00	0.73	0.07767
46	1023	0.03033	0.14	0.20	0.00	0.00	0.66	0.09868
47	1023	0.02634	0.28	0.20	0.00	0.00	0.52	0.15222

No.	T (K)	Catalyst Weight (g)	Feed mole fraction					CO_2 Conversion
			x_{H2}	x_{CO2}	x_{CO}	x_{H2O}	x_{N2}	
48	1023	0.02435	0.35	0.20	0.00	0.00	0.45	0.13029
49	1023	0.03179	0.07	0.19	0.02	0.00	0.71	0.07381
50	1023	0.02756	0.20	0.20	0.03	0.00	0.57	0.13083
51	1023	0.02649	0.20	0.20	0.07	0.00	0.53	0.16591
52	1023	0.02541	0.20	0.20	0.10	0.00	0.50	0.17752
53	1023	0.03033	0.14	0.20	0.00	0.03	0.66	0.05439
54	1023	0.02863	0.20	0.20	0.00	0.03	0.60	0.08111
55	1023	0.02634	0.28	0.20	0.00	0.03	0.52	0.08238
56	1023	0.02541	0.20	0.20	0.10	0.03	0.50	0.04841
57	973	0.01522	0.59	0.08	0.00	0.00	0.33	0.20966
58	973	0.01844	0.52	0.15	0.00	0.00	0.33	0.11552
59	973	0.02327	0.42	0.25	0.00	0.00	0.33	0.07293
60	973	0.02714	0.33	0.33	0.00	0.00	0.33	0.07712
61	973	0.02549	0.40	0.35	0.00	0.00	0.25	0.09566
62	973	0.02291	0.40	0.20	0.00	0.00	0.40	0.08155
63	973	0.02119	0.40	0.10	0.00	0.00	0.50	0.11915
64	973	0.01997	0.40	0.03	0.00	0.00	0.56	0.17482
65	973	0.02655	0.32	0.28	0.00	0.00	0.40	0.06813
66	973	0.03274	0.10	0.28	0.00	0.00	0.62	0.02729
67	973	0.03004	0.20	0.28	0.00	0.00	0.52	0.02166
68	973	0.03127	0.20	0.35	0.00	0.00	0.45	0.00828
69	973	0.02907	0.15	0.15	0.00	0.00	0.70	0.02603
70	973	0.02636	0.20	0.07	0.00	0.00	0.73	0.15403
71	973	0.02759	0.20	0.14	0.00	0.00	0.66	0.08306
72	973	0.02863	0.20	0.20	0.00	0.00	0.60	0.08916
73	973	0.03232	0.07	0.20	0.00	0.00	0.73	0.05488
74	973	0.03033	0.14	0.20	0.00	0.00	0.66	0.06659
75	973	0.02634	0.28	0.20	0.00	0.00	0.52	0.09928
76	973	0.02435	0.35	0.20	0.00	0.00	0.45	0.08450
77	973	0.03179	0.07	0.19	0.02	0.00	0.71	0.05442
78	973	0.02756	0.20	0.20	0.03	0.00	0.57	0.09210
79	973	0.02649	0.20	0.20	0.07	0.00	0.53	0.11808
80	973	0.02541	0.20	0.20	0.10	0.00	0.50	0.12794
81	973	0.03033	0.14	0.20	0.00	0.03	0.66	0.04438

No.	T (K)	Catalyst Weight (g)	Feed mole fraction					CO_2 Conversion
			x_{H2}	x_{CO2}	x_{CO}	x_{H2O}	x_{N2}	
82	973	0.02863	0.20	0.20	0.00	0.03	0.60	0.00000
83	973	0.02634	0.28	0.20	0.00	0.03	0.52	0.05803
84	973	0.02541	0.20	0.20	0.10	0.03	0.50	0.00665
85	923	0.01522	0.59	0.08	0.00	0.00	0.33	0.14287
86	923	0.01844	0.52	0.15	0.00	0.00	0.33	0.06950
87	923	0.02327	0.42	0.25	0.00	0.00	0.33	0.04224
88	923	0.02714	0.33	0.33	0.00	0.00	0.33	0.05738
89	923	0.02549	0.40	0.35	0.00	0.00	0.25	0.07775
90	923	0.02291	0.40	0.20	0.00	0.00	0.40	0.05520
91	923	0.02119	0.40	0.10	0.00	0.00	0.50	0.08075
92	923	0.01997	0.40	0.03	0.00	0.00	0.56	0.09817
93	923	0.02655	0.32	0.28	0.00	0.00	0.40	0.04251
94	923	0.03274	0.10	0.28	0.00	0.00	0.62	0.00976
95	923	0.03004	0.20	0.28	0.00	0.00	0.52	0.00753
96	923	0.03127	0.20	0.35	0.00	0.00	0.45	0.00000
97	923	0.02907	0.15	0.15	0.00	0.00	0.70	0.01855
98	923	0.02636	0.20	0.07	0.00	0.00	0.73	0.10955
99	923	0.02759	0.20	0.14	0.00	0.00	0.66	0.05670
100	923	0.02863	0.20	0.20	0.00	0.00	0.60	0.06155
101	923	0.03232	0.07	0.20	0.00	0.00	0.73	0.04119
102	923	0.03033	0.14	0.20	0.00	0.00	0.66	0.04835
103	923	0.02634	0.28	0.20	0.00	0.00	0.52	0.06777
104	923	0.02435	0.35	0.20	0.00	0.00	0.45	0.05456
105	923	0.03179	0.07	0.19	0.02	0.00	0.71	0.04223
106	923	0.02756	0.20	0.20	0.03	0.00	0.57	0.07197
107	923	0.02649	0.20	0.20	0.07	0.00	0.53	0.10124
108	923	0.02541	0.20	0.20	0.10	0.00	0.50	0.14036
109	923	0.03033	0.14	0.20	0.00	0.03	0.66	0.03446
110	923	0.02863	0.20	0.20	0.00	0.03	0.60	0.03764
111	923	0.02634	0.28	0.20	0.00	0.03	0.52	0.03051
112	923	0.02541	0.20	0.20	0.10	0.03	0.50	0.01488

Procedure to simulate CO_2 conversion and Fitting in Matlab:

The rate and equilibrium constants were determined using Matlab codes involving solving a non-linear least square problem (lsqcurvefit command) where the exit gas composition was calculated assuming an integral reactor. The method consists in writing the mole balance for each species and solving the resulting system of ordinary equations.

H_2 mole balance: $$\frac{dF_{H_2}}{dW} = -r_1 \quad (4.1)$$

CO_2 mole balance: $$\frac{dF_{CO_2}}{dW} = -r_1 \quad (4.2)$$

H_2O mole balance: $$\frac{dF_{H_2O}}{dW} = r_1 \quad (4.3)$$

CO mole balance: $$\frac{dF_{CO}}{dW} = r_1 \quad (4.4)$$

where F_i is the molar flow rate (mol/min) of species i, r_1 the reaction rate (mol/(min.g)) and W the mass of catalyst (g) in the bed.

The molar flow rates of each species were solved. Yet, the rate expressions are a function of partial pressure. Considering ideal gas, the relationship between partial molar flow rate and partial pressure for each species are:

$$P_{H_2} = \frac{F_{H_2}}{F_T} P \quad (4.5)$$

$$P_{CO_2} = \frac{F_{CO_2}}{F_T} P \quad (4.6)$$

$$P_{H_2O} = \frac{P_{H_2O}}{F_T} P \quad (4.7)$$

$$P_{CO} = \frac{P_{CO}}{F_T} P \quad (4.8)$$

$$F_T = F_{H_2} + F_{CO_2} + F_{H_2O} + F_{CO} + F_I \quad (4.9)$$

where F_T is total flow rate and F_I is the flow rate of inert (N_2)

The Matlab codes to solve the non-linear least square problem consist of one main script (RWGS_Fitting-Arrhenius) and five function files (CO2_Conversion_Arrhenius,

RWGS_ODE, Enthalpy, Entropy and RWGS). Further description of those Matlab files, as well as their codes can be found in Appendix A.

All the experimental data in Table 4.2 were used in solving a non-linear least square problem, except the experiment where CO was present in the feed stream and a few experiments were considered as outliers.

The experiments involving CO in the feed stream were omitted from solving the non-linear least square problem because the experimental results showed trends that did not make sense; for the reverse WGS reaction, CO is the product of the reaction, but unexpectedly, increasing the CO content in the feed led to an increase in CO_2 conversion (and this was observed at all temperatures). The reason for this is likely due to carbon formation through the Boudouard reaction (2 CO $\rightarrow$ C + CO_2) upstream of the bed (i.e. before the gas contacts the catalyst). Through the Boudouard reaction, the amount of CO_2 would increase when the feed stream contacts the catalyst. As a consequence, the reaction $H_2 + CO_2 \rightleftarrows H_2O + CO$ would tend to move more in the left direction. This possible effect of the Boudouard reaction upstream from the bed was further reinforced by significant carbon deposit on the feeding tube.

Determination of global rate expressions for the reverse WGS reaction

Reverse WGS reaction (global reaction):

$$H_2 + CO_2 \rightleftarrows H_2O + CO \qquad (4.10)$$

The reaction (4.10) is a gas-solid catalytic reaction and it was assumed that it can be described by a Langmuir-Hinshelwood type of mechanism (adsorption of reactant, surface reaction and desorption of products). The global reaction (4.10) can be decomposed as the following:

$H_2(g) + S \leftrightarrow H_2.S$ Adsorption of H_2 on the surface (4.11)

$CO_2(g) + S \leftrightarrow CO_2.S$ Adsorption of CO_2 on the surface (4.12)

$CO_2.S + S \leftrightarrow CO.S + O.S$ Surface reaction I (4.13)

$$H_2.S + O.S \leftrightarrow H_2O.S + S \quad \text{Surface reaction II} \quad (4.14)$$

$$H_2O.S \leftrightarrow H_2O(g) + S \quad \text{H}_2\text{O desorption} \quad (4.15)$$

$$CO.S \leftrightarrow CO(g) + S \quad \text{CO desorption} \quad (4.16)$$

Based on the reaction mechanism (4.11) to (4.16), rate expressions were determined for each case where each one of the above reaction steps were considered as the rate limiting step. Best fit simulations were carried out for each case of rate determining step. Reaction (4.13) gave the best fit between simulation and experimental results, implying that the surface reaction I is the most likely rate determining step.

Also, the non-linear least square fitting systematically returned a value of zero for the H_2 adsorption constant. This indicates that the concentration of $H_2.S$ is extremely small, or $H_2.S$ reacts very rapidly with O.S in the reaction $H_2.S + O.S \leftrightarrow H_2O.S + S$. Therefore, the reactions $H_2(g) + S \leftrightarrow H_2.S$ and $H_2.S + O.S \leftrightarrow H_2O.S + S$ could then be combined in one reaction:

$$H_2(g) + O.S \rightleftarrows H_2O.S \quad (4.17)$$

This assumption agrees well with that of Lui et al. (2010) as they proposed the following mechanism for the reverse WGS reaction consisting of five steps:

$$CO_2(g) + S \rightleftarrows CO_2.S: \quad \text{Adsorption of } CO_2 \text{ on the surface} \quad (4.18)$$

$$CO_2.S + S \rightleftarrows CO.S + O.S: \quad \text{Surface reaction I} \quad (4.19)$$

$$H_2(g) + O.S \rightleftarrows H_2O.S: \quad \text{Surface reaction II} \quad (4.20)$$

$$H_2O.S \rightleftarrows H_2O(g) + S: \quad \text{H}_2\text{O desorption} \quad (4.21)$$

$$CO.S \rightleftarrows CO(g) + S: \quad \text{CO desorption} \quad (4.22)$$

Based on the Liu et al. (2010) reaction mechanism, the rate expressions were determined for each case where each one of the above reactions steps (4.18 to 4.22) were considered as the rate limiting step. The rate expressions are shown in Table 4.3. As an example of the determination of the rate of reaction, Appendix B shows how the rate of reaction for reaction (4.23) was derived.

Table 4.3: Reverse water-gas shift rate expressions depending on the rate limiting step based on Liu et al. (2010) mechanism

Rate limiting step	Rate of reaction
$CO_2(g) + S \leftrightarrow CO_2.S$	$r_{A1} = \frac{k\left(P_{CO_2} - \frac{P_{CO}P_{H_2O}}{K_p P_{H_2}}\right)}{\left(1 + \frac{K_{CO}K_{H_2O}P_{CO}P_{H_2O}}{K_{s1}K_{s2}P_{H_2}} + K_{CO}P_{CO} + \frac{K_{H_2O}P_{H_2O}}{K_{s2}p_{H_2}} + K_{H_2O}P_{H_2O}\right)}$ Where $k = C_t k_{A1}$ $\quad K_p = \frac{K_{s1}K_{s2}}{K_{CO}K_{H_2O}}$
$CO_2.S + S \leftrightarrow CO.S + O.S$	$r_{s1} = \frac{k\left(P_{CO_2} - \frac{P_{H_2O}P_{CO}}{K_p P_{H_2}}\right)}{\left(1 + K_{CO_2}P_{CO_2} + K_{CO}P_{CO} + \frac{K_{H_2O}P_{H_2O}}{K_{s2}P_{H_2}} + K_{H_2O}P_{H_2O}\right)^2}$ Where $k = {C_t}^2 k_{s1}K_{CO_2}$ $\quad K_p = \frac{K_{CO_2}K_{s1}K_{s2}}{K_{CO}K_{H_2O}}$
$H_2(g) + O.S \leftrightarrow H_2O.S$	$r_{s2} = \frac{k\left(\frac{P_{CO_2}P_{H_2}}{P_{CO}} - \frac{P_{H_2O}}{K_p}\right)}{\left(1 + K_{CO_2}P_{CO_2} + K_{CO}P_{CO} + \frac{K_{CO_2}P_{CO_2}K_{s1}}{K_{CO}P_{CO}} + K_{H_2O}P_{H_2O}\right)}$ *where* $k = \frac{C_t k_{s2}K_{CO_2}K_{s1}}{K_{CO}}$ $\quad K_p = \frac{K_{CO_2}K_{s1}K_{s2}}{K_{CO}K_{H_2O}}$
$H_2O.S \leftrightarrow H_2O(g) + S$	$r_{D1} = \frac{k\left(\frac{P_{CO_2}P_{H_2}}{P_{CO}} - \frac{P_{H_2O}}{K_p}\right)}{\left(1 + K_{CO_2}P_{CO_2} + K_{CO}P_{CO} + \frac{K_{CO_2}P_{CO_2}K_{s1}}{K_{CO}P_{CO}} + \frac{K_{s1}K_{s2}K_{CO_2}P_{H_2}P_{CO_2}}{K_{CO}P_{CO}}\right)}$ Where $k = \frac{k_{D1}K_{s1}K_{s2}K_{CO_2}C_t}{K_{CO}}$ $\quad K_p = \frac{K_{s1}K_{s2}K_{CO_2}}{K_{CO}K_{H_2O}}$
$CO.S \leftrightarrow CO(g) + S$	$r_{D2=} \frac{k\left(\frac{P_{CO_2}P_{H_2}}{P_{H_2O}} - \frac{P_{CO}}{K_p}\right)}{\left(1 + K_{CO_2}P_{CO_2} + K_{H_2O}P_{H_2O} + \frac{K_{H_2O}P_{H_2O}}{K_{s2}P_{H_2}} + \frac{K_{s1}K_{s2}K_{CO_2}P_{H_2}P_{CO_2}}{K_{H_2O}P_{H_2O}}\right)}$ Where $k = \frac{k_{D2}K_{s1}K_{s2}K_{CO_2}C_t}{K_{H_2O}}$ $\quad K_p = \frac{K_{s1}K_{s2}K_{CO_2}}{K_{CO}K_{H_2O}}$

For each case of limiting step, at each temperature, the corresponding rate and equilibrium constant were determined from best fit with the experimental data using a non-linear least square method. Once those constants were determined at temperatures of 650, 700 and 750 and 800°C, Arrhenius plot were constructed to determine the activation energy and pre-exponential factors. All those Arrhenius plots are in Appendix C. Among those plots, that of surface reaction I ($CO_2.S + S \leftrightarrow CO.S + O.S$) yielded the best linear relationship. It was then concluded that the surface reaction I is the most likely rate limiting step for the reverse WGS reaction on SDC. This agrees with the findings of Ernst et al. (1992), Gines et al. (1997) and Goguet et al. (2004), for RWGS on Cu, $CuO/ZnO/Al_2O_3$ and Pt/CeO_2 catalysts.

The reaction rate considered will thus be the following (surface reaction I as rate limiting step):

$$r_{s1} = \frac{k\left(P_{CO_2} - \frac{P_{H_2O}P_{CO}}{K_p P_{H_2}}\right)}{\left(1 + K_{CO_2}P_{CO_2} + K_{CO}P_{CO} + \frac{K_{H_2O}P_{H_2O}}{K_{s2}P_{H_2}} + K_{H_2O}P_{H_2O}\right)^2} \quad (4.23)$$

where

$$k = {C_t}^2 k_{s1} K_{CO_2} \text{and} K_p = \frac{K_{CO_2}K_{s1}K_{s2}}{K_{CO}K_{H_2O}}$$

The various rate and equilibrium constants were then fitted so that the calculated CO_2 conversion matches with the experimental data. To start the simulation, k, K_{CO2}, K_{CO}, K_{S2}, and K_{H2O} were first arbitrarily estimated. The values determined in the first simulation were then used as an initial guess to refine the estimation of k, K_{CO2}, K_{CO}, K_{S2}, and K_{H2O}. This process continued until the best fit with the experimental CO_2 conversion was obtained.

Based on this reaction rate, there are five unknowns to be determined: k, K_{CO2}, K_{CO}, K_{S2}, and K_{H2O}. K_p represents the equilibrium constant for the global reaction and can be calculated from thermodynamics data (e.g. Perry's Chemical Engineer's Handbook).

In the simulation, K_{CO} and K_{CO2} systematically returned a value of zero. Therefore, the terms K_{CO} and K_{CO2} in the denominator were removed from the rate expression and thus these two adsorption equilibrium constants were not determined. The comparison between the experimental results and the simulation in terms of CO_2 conversion is shown in Figure 4.12 to Figure 4.15 at different temperatures. The CO_2 conversion was calculated as:

$$X_{CO_2} = \frac{F_{CO_2,in} - F_{CO_2,out}}{F_{CO_2,in}} \tag{4.24}$$

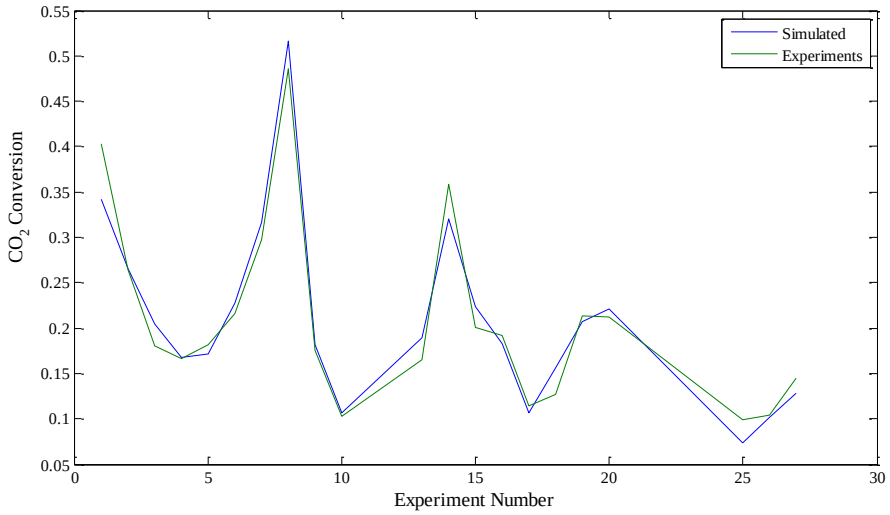

Figure 4.12: Comparison between experiments and simulation for the conversion of CO_2 at 800^{o}C

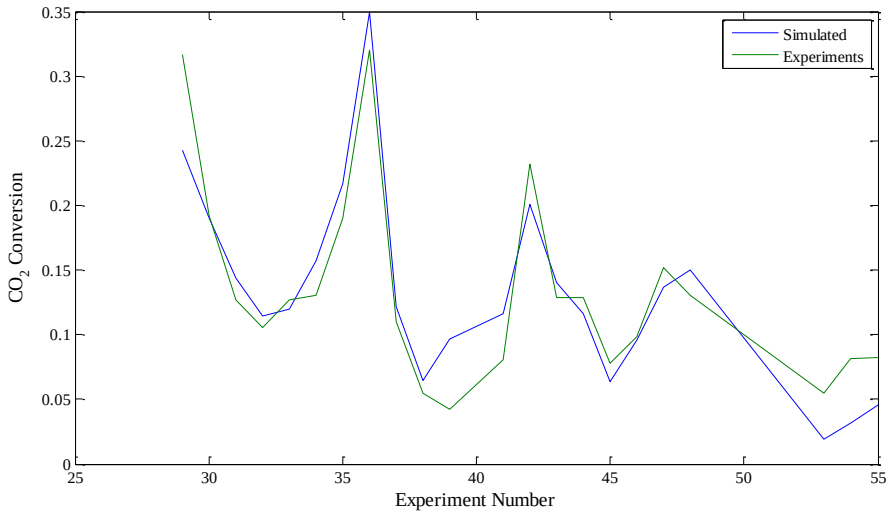

Figure 4.13: Comparison between experiments and simulation for the conversion of CO_2 at 750^{o}C

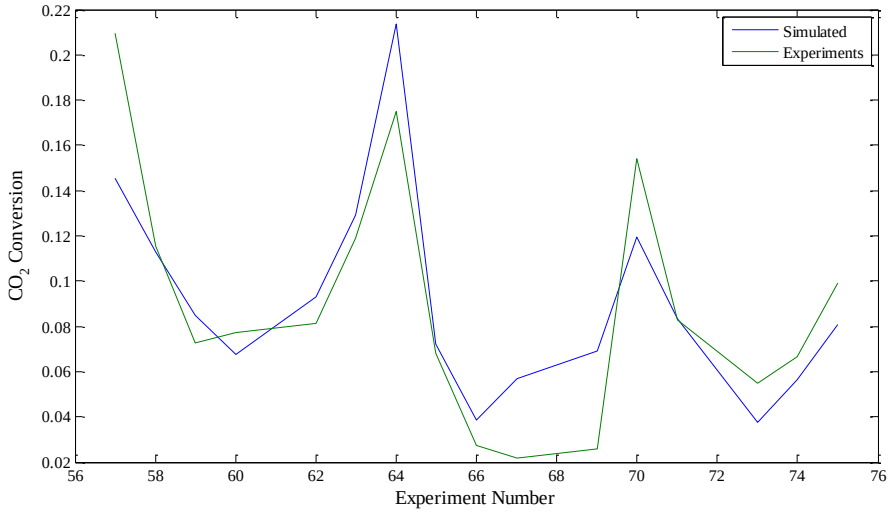

Figure 4.14: Comparison between experiments and simulation for the conversion of CO_2 at 700^{o}C

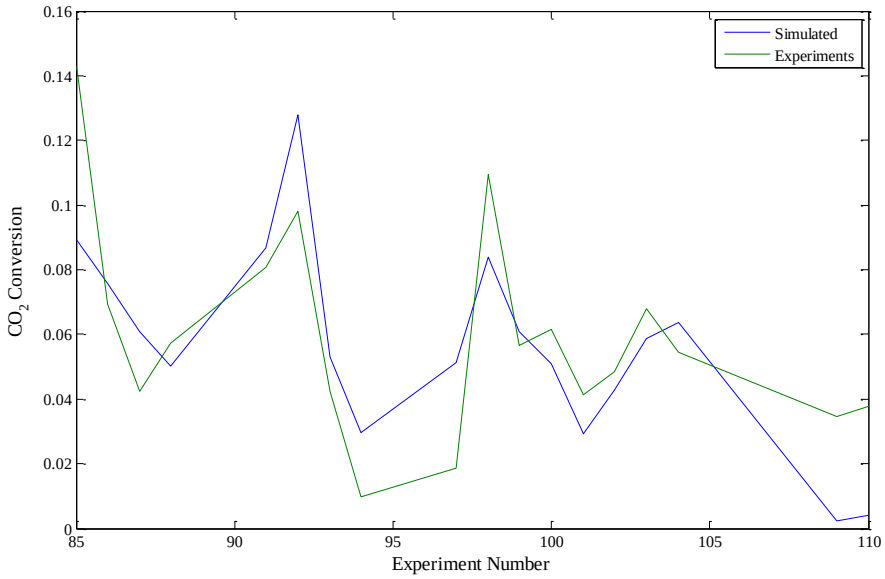

Figure 4.15: Comparison between experiments and simulation for the conversion of CO_2 at 650^oC

The value of kinetic parameters obtained at four temperatures when the surface reaction I is the rate limiting step is given in Table 4.4.

Table 4.4: Kinetic parameters of reverse WGS reaction when the surface reaction I is rate limiting

Temperature (^oC)	k ($molmin^{-1}g^{-1}atm^{-1}$)	K_{S2} atm^{-1}	K_{H2O} atm^{-1}
800	1.1602	0.0120	0.2063
750	0.5445	0.0022	0.0701
700	0.3139	0.0006	0.0332
650	0.1222	0.0001	0.0068

Using the value of k, K_{S2} and K_{H2O} from Table 4.4, the Arrhenius plot is shown in Figure 4.16 to Figure 4.18.

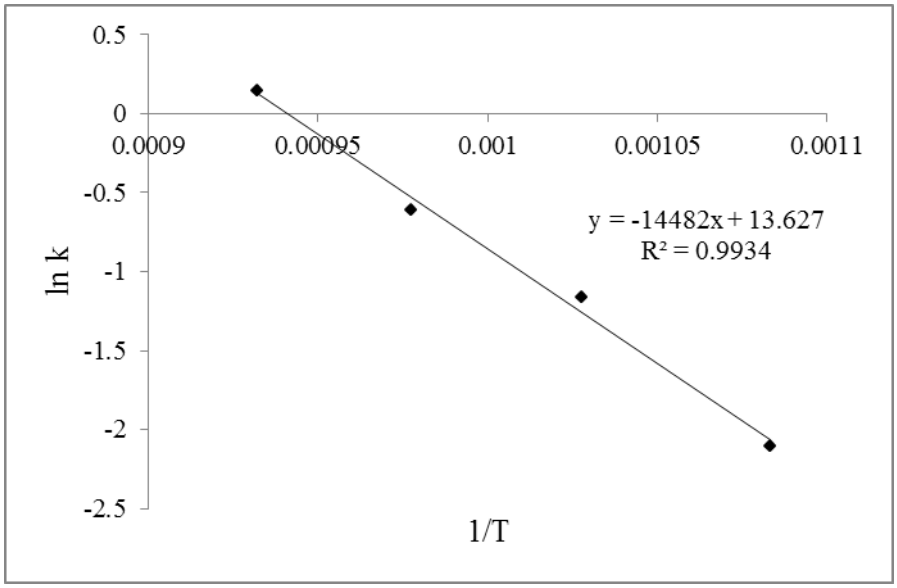

Figure 4.16: Arrhenius plot of k

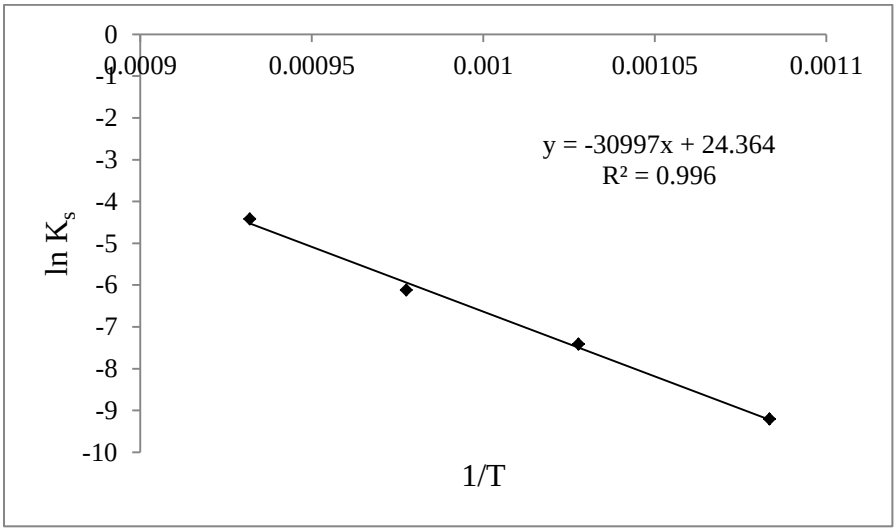

Figure 4.17: Arrhenius plot of K_S

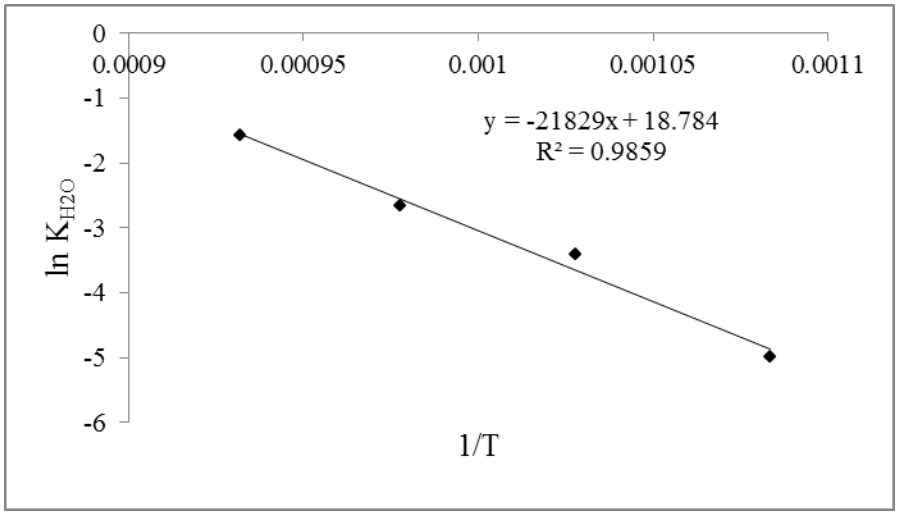

Figure 4.18: Arrhenius plot of K_{H2O}

From the Arrhenius plot, the activation energies were calculated as: E_k= 120kJ/mol, E_{KS}= 257kJ/mol and E_{KH2O}= 181kJ/mol.

To achieve better accuracy, the fitting was repeated, but this time to include all temperatures simultaneously. The rate and equilibrium constants are written as follows:

$$k(T) = k(T_{ref})exp\left(\frac{-E}{R}\left(\frac{1}{T} - \frac{1}{T_{ref}}\right)\right) \tag{4.25}$$

The temperature 750^{o}C was used as a reference temperature. The values of k and K's and their activation energy determined from the fitting at separate temperatures were used as initial guesses.

Figure 4.19 shows the comparison of the experiments and simulations for the conversion of CO_2 for all the temperatures when considering all experiments at once and when using the expression of the rate constant shown in Eq. 4.25.

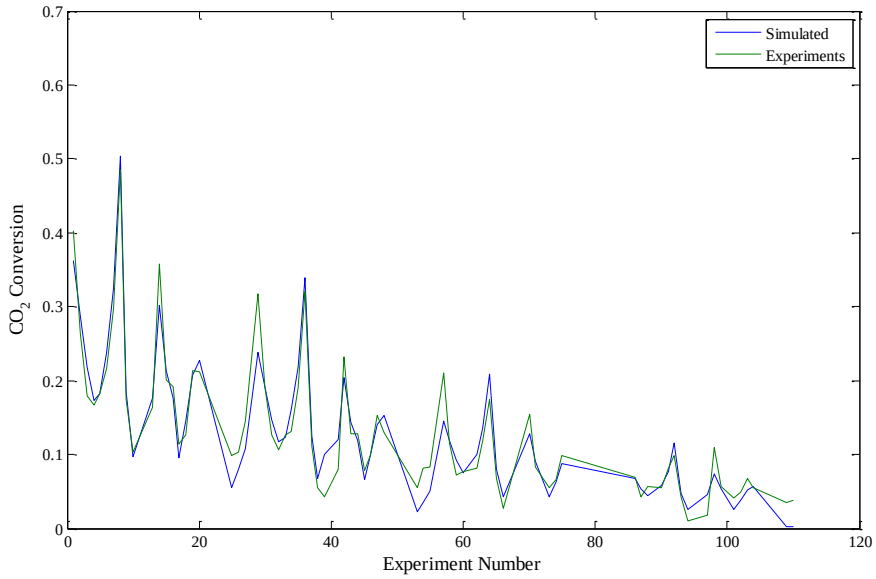

Figure 4.19: Comparison between experiments and simulations for the conversion of CO_2 at temperature of 800-650^{o}C

Based on the simulation involving all temperatures in one simulation, the Arrhenius equations for k, K_S and K_{H2O} are as follows:

$$k = 2.18 \times 10^5 e^{\frac{-111000}{RT}} \quad (4.26)$$

$$K_S = 3.36 \times 10^{10} e^{\frac{-256000}{RT}} \quad (4.27)$$

$$K_{H_2O} = 9.04 \times 10^8 e^{\frac{-197000}{RT}} \quad (4.28)$$

The values of the activation energy in equations 4.26-4.28 are quite similar to the values found when considering temperatures independently which was to be expected because the Arrhenius plot yielded a good linear relationship.

Table 4.5 presents a comparison between the activation energy for the reaction rate constant determined in this study (111 kJ/mol) and values mentioned in the literature for the reverse WGS reaction over different catalysts and different temperature ranges.

Table 4.5: Reverse WGS activation energy from literature

Catalyst	Pressure (atm)	Temperature (^oC)	Activation energy (kJ/mol)	Reference
Ni/Al_2O_3	1	300-500	87.03	Osaki et al. (1997)
Co/Al_2O_3	1	300-500	76.99	Osaki et al. (1997)
Fe/Al_2O_3	1	300-500	78.24	Osaki et al. (1997)
$CuO/ZnO/Al_2O_3$	1	227	100.24	Gines et al. (1997)
Pt/YSZ	1	650-800	65.27	Pekridis et al. (2007)

Because the values reported in the literature are for different materials and sometimes different temperature ranges, it is difficult to make a meaningful comparison with our values. Nonetheless, the values determined here are higher than any reported value, although in the same order of magnitude. This should be expected since SDC alone is less active towards the reverse WGS reaction compared to Ni, Co, Fe, Cu and Pt catalyst due to its higher activation energy.

4.5 Markov Chain Monte Carlo Study

The Matlab simulation discussed in section 4.4 was not able to calculate the uncertainty for the calculated parameters. In order to calculate the uncertainty for each parameters, a Markov Chain Monte Carlo (MCMC) study was conducted. This MCMC study was a collaboration with Professor Thomas A. Duever and his master student Manoj Mathew from the Chemical Department, University of Waterloo, who did the actual calculations and contributed to the writing of this section.

MCMC not only provides reliable parameters estimation but also accurately captures parameter uncertainty. The MCMC method randomly draws around 1,000,000-2,000,000 samples from the parameter probability function. The mean of the generated samples from the MCMC technique is the value of the parameter point estimate. The uncertainty of the parameter point estimate can be calculated using the standard deviation of the simulated samples.

To find the optimal parameter values, the MCMC method randomly draws samples from the parameter likelihood function. It is important to ensure that the simulated samples are coming from the desired probability distribution. One measure of determining whether or not the Markov Chain has converged to its target distribution is to calculate the percent of accepted samples in the MCMC cycle. An acceptance rate around 23% is ideal as shown by Roberts (1997). Another technique is to simply plot the MCMC output and subsequently determine whether or not the discrete samples are stationary.

In MCMC simulation, equations 4.29 and 4.5-4.8 were solved simultaneously. The results from Matlab simulation were used as the starting value for the MCMC. Prior to the MCMC analysis, sensitivity analysis has been conducted to provides information on whether or not the parameters in the equation 4.29 can be estimated. Sensitivity analysis involves calculating the numerical gradient, where the gradient represents the change in the model response after perturbing one of the parameters. The sensitivity of the response variable to changes in parameter values can be illustrated graphically by plotting the gradient as a function of one of the independent variables. Comparison of the magnitude of the gradient values for all the parameters can provide valuable information about whether or not the parameters in the given model can be estimated under the current experimental conditions.

$$r_{s1} = \frac{k\left(P_{CO_2} - \frac{P_{H_2O}P_{CO}}{K_p P_{H_2}}\right)}{\left(1 + K_{CO_2}P_{CO_2} + K_{CO}P_{CO} + \frac{K_{H_2O}P_{H_2O}}{K_{s2}P_{H_2}} + K_{H_2O}P_{H_2O}\right)^2} \tag{4.29}$$

For the purposes of model sensitivity analysis, gradient plots were generated at each temperature. For the sake of brevity, only the gradient plots at a temperature of 1023 K are shown here. The obtained gradient values for parameters k, K_{S2} and K_{H2O} at temperatures from 1023 to 923 K were found to be several orders of magnitude higher than the gradient values for parameters K_{CO2} and K_{CO} (Figure 4.20). This result seems to indicate that at temperatures below 1023K, only k, K_s and K_{H2O} parameter can be estimated. Although the parameters K_{CO} and K_{CO2} do become significant at a temperature of 1073 K (Figure 4.21), the

poor observed ability at low temperatures indicates that these two parameters cannot be estimated using the given model and under the current experimental conditions. Therefore, K_{CO} and K_{CO2} were dropped from the rate expression. These sensitivity analysis findings were similar to the non-linear least square results where the values of K_{CO} and K_{CO2} are significant at 1073 K but have very small values (approaching zero) at lower temperatures. Both methods (non-linear least square and MCMC) point to the impossibility here to determine K_{CO} and K_{CO2} within the experimental conditions used in the present work.

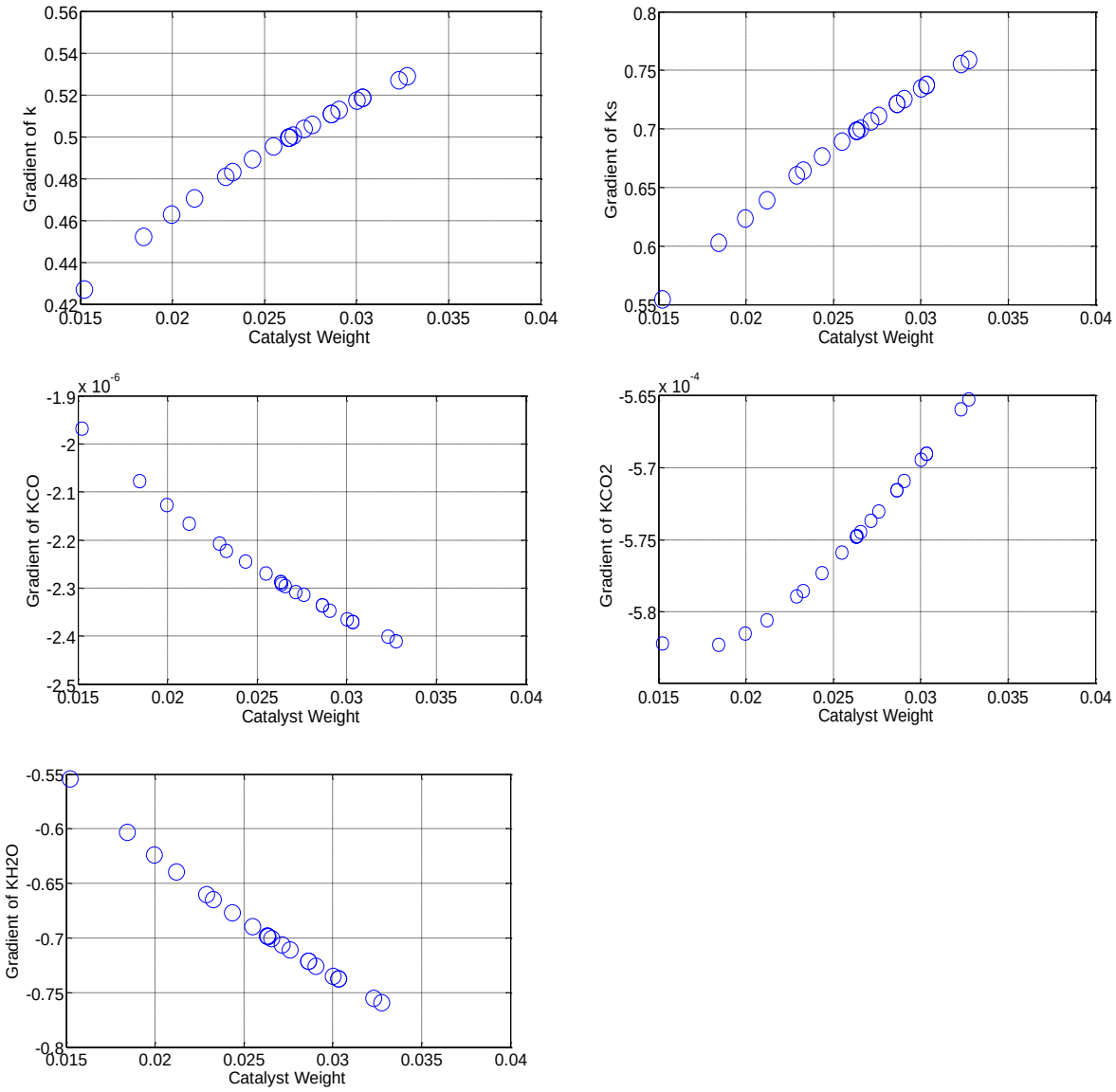

Figure 4.20: The gradient plots for parameters k, K_{s2}, K_{CO}, K_{CO2} and K_{H2O} as a function of the catalyst weight using data points at 1023 K

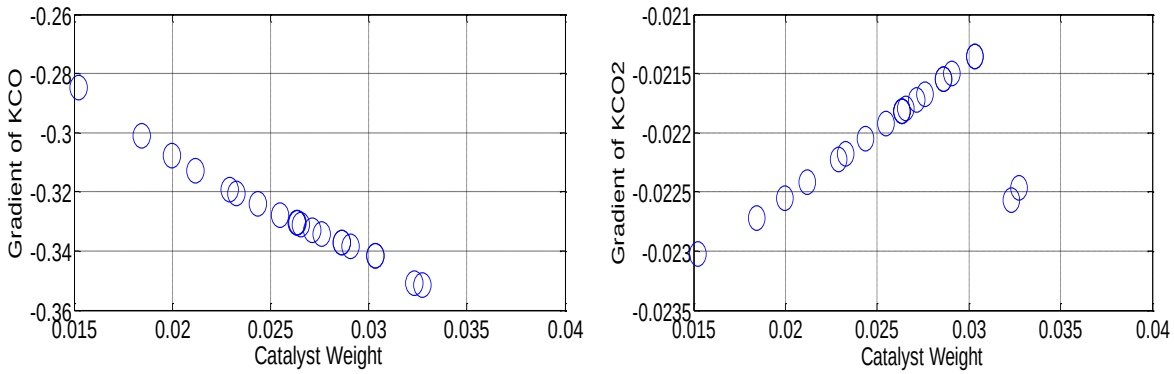

Figure 4.21:The gradient plots for parameters K_{CO} and K_{CO2} as a function of the catalyst weight using data points at 1073 K

After dropping parameters K_{CO} and K_{CO2}, the kinetic model can be simplified to equation:

$$r_{s1} = \frac{k\left(P_{CO_2} - \frac{P_{H_2O}P_{CO}}{K_p P_{H_2}}\right)}{\left(1 + \frac{K_{H_2O}P_{H_2O}}{K_{s2}P_{H_2}} + K_{H_2O}P_{H_2O}\right)^2} \tag{4.30}$$

After the sensitivity analysis was conducted, parameter estimation of the kinetic parameters in equation 4.30 were carried out using Markov Chain Monte Carlo (MCMC). The MCMC run for 100,000 cycles in order to get a good estimate of the sample mean. Although ideally, the number of runs should be around 1,000,000-2,000,000, solving the differential equations were computationally expensive and, therefore, a smaller number of cycles were used.

Once the MCMC output was analyzed, it became evident that Markov Chain for parameters K_{s2} and K_{H2O} were not able to converge to the desired distribution. As shown in Figure 4.22, the sampled MCMC values for these two parameters are not stationary since the mean is not constant throughout. The Markov Chain for the rate constant k, however, appears to have converged since the mean is constant throughout the MCMC cycle.

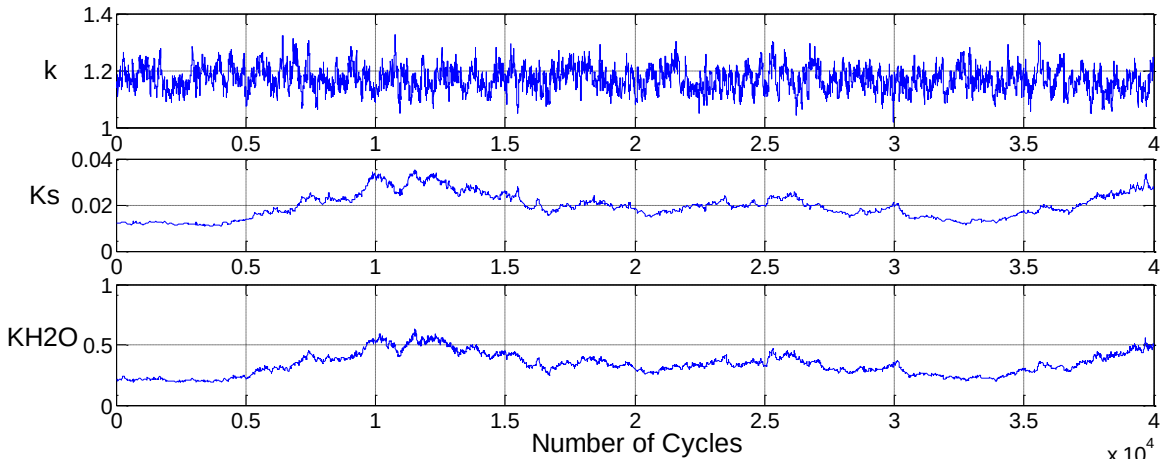

Figure 4.22: MCMC output values for parameters k, Ks and KH2O at a temperature of 1073 K

One possible reason for the lack of convergence for K_s and K_{H2O} might be due to a high degree of correlation between the two parameters. Figure 4.22 reveals that the values for K_s and K_{H2O} move up and down simultaneously. The correlation could be the consequence of the model shown in equation 4.30, where K_{s2} and K_{H2O} appear as a ratio. Therefore, although K_s and K_{H2O} cannot be estimated together, the model can be re-parameterized and the ratio of the two equilibrium constants (written as K_L) can be estimated.

$$r_{s1} = \frac{k\left(P_{CO_2} - \frac{P_{H_2O}P_{CO}}{K_p P_{H_2}}\right)}{\left(1 + K_L\frac{P_{H_2O}}{P_{H_2}} + K_{H_2O}P_{H_2O}\right)^2} \tag{4.31}$$

The model simplification process was once again repeated for the above model and the gradient plots were generated. The obtained gradient values from these plots suggested that the parameter K_{H2O} is not observable. Once again, since the parameter cannot be estimated under the current experimental conditions, the parameter was dropped and the final simplified model is shown below.

$$r_{s1} = \frac{k\left(P_{CO_2} - \frac{P_{H_2O}P_{CO}}{K_p P_{H_2}}\right)}{\left(1 + K_L\frac{P_{H_2O}}{P_{H_2}}\right)^2} \tag{4.32}$$

Finally, the parameters in the final simplified model (equation 4.32) were calculated with MCMC. The point estimates and the standard deviation for all four parameters are shown in Table 4.6. The estimates were obtained by taking the mean of the samples obtained in MCMC analysis. The error of the parameter values can also be quantified using the standard deviation of the samples.

Table 4.6: The parameters estimates and standard deviation obtained from MCMC analysis using all four temperatures with Tref= 998 K

Parameters	Parameter Estimate (MCMC)	Standard Deviation (MCMC)
$k_{Tref}(molmin^{-1}g^{-1}atm^{-1})$	0.3466	0.0279
$K_{L,Tref}$	33.3474	2.9818
E_k (J/mol)	106,830	12,341
E_{KL}(J/mol)	-63,661	13,386

In addition, the MCMC samples can be used to generate joint confidence regions (JCRs). The JCRs for the four sets of temperatures are shown below.

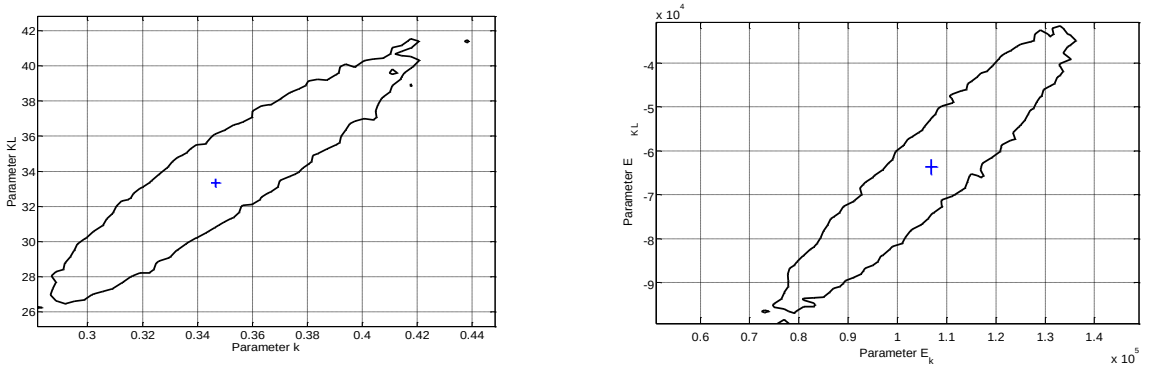

Figure 4.23: A 95% joint confidence region for parameters k and KL and Ek and EKL (below)

Once the parameters are estimated, graphical diagnostic checks can be implemented in order to verify that the model is able to accurately fit the data. Figure 4.24 shows that the simulated values using the parameter estimates give very similar results when compared to the experimental data. This is supported by the residual plot in Figure 4.25 where the residuals are randomly distributed about zero. Both these plots seem to indicate that the model is able to fit the experimental data very well.

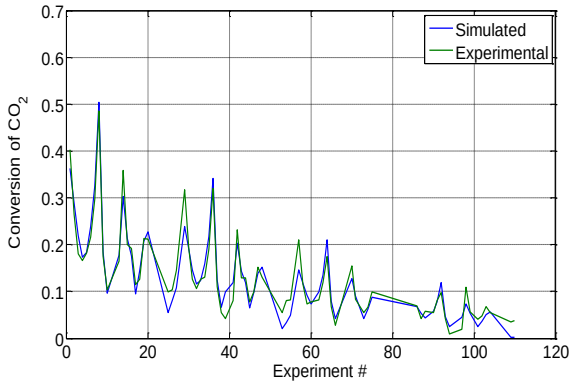

Figure 4.24: A plot of predicted values compared with experimentally observed values

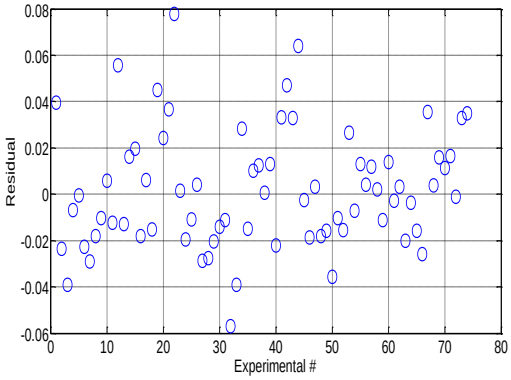

Figure 4.25: Residual plot that measures the difference between the observed and the predicted values

As a conclusion, the parameter values estimation from the MCMC and non-linear least square simulation are very close to each other, as shown in Table 4.7.

Table 4.7: The parameters estimates and standard deviation obtained from MCMC analysis at 998 K

Parameters	Parameter Estimate (MCMC)	Standard Deviation (MCMC)	Parameter Estimate (non-linear least square)
k_{Tref}(molmin^{-1}g^{-1}atm^{-1})	0.3466	0.0279	0.335
$K_{L,Tref}$	33.3474	2.9818	33.075
E_k (J/mol)	106,830	12,341	111,000
E_{KL}(J/mol)	-63,661	13,386	-59,000

Even though the non-linear least square parameter estimation using Matlab was not able to calculate the uncertainty for each parameters estimate, this method was able to estimate the parameters very close to those found using the MCMC method. One of the advantages of the Matlab simulation is that it was able to estimate the K_{S2} and K_{H2O} separately while in MCMC, these two parameters were estimated as a ratio of K_{H2O}/K_{s2} called as K_L. The value of K_L and E_{KL} can be determined from the non-linear least square method as follows:

$$K_L = \frac{K_{H_2O}}{K_{S2}} = \frac{9.04 \times 10^8}{3.36 \times 10^{10}} e^{\frac{-(197000-256000)}{RT}} = 0.027 e^{\frac{-(-59000)}{RT}} \quad (4.33)$$

The corresponding values for K_L and E_{KL} are shown in Table 4.7, and are very similar to those obtained from MCMC.

As mentioned before, the final reaction rate expression from the MCMC simulation is

$$r_{s1} = \frac{k\left(P_{CO_2} - \frac{P_{H_2O}P_{CO}}{K_p P_{H_2}}\right)}{\left(1 + K_L \frac{P_{H_2O}}{P_{H_2}}\right)^2} \quad (4.34)$$

and from non-linear least square simulation is

$$r_{s1} = \frac{k\left(P_{CO_2} - \frac{P_{H_2O}P_{CO}}{K_p P_{H_2}}\right)}{\left(1 + \frac{K_{H_2O}P_{H_2O}}{K_{s2}P_{H_2}} + K_{H_2O}P_{H_2O}\right)^2} \tag{4.35}$$

Note that the value of K_{H2O} is small and the value of P_{H2O} is less than 1. Therefore the value of $K_{H_2O}P_{H_2O}$ in the denominator is negligible compared to 1. If the term $K_{H_2O}P_{H_2O}$ was eliminated in the denominator for the non-linear least square method, both Matlab and MCMC would end up with the same reaction rate expression. Therefore we conclude that the final rate expression for RWGS is the following

$$r_{s1} = \frac{k\left(P_{CO_2} - \frac{P_{H_2O}P_{CO}}{K_p P_{H_2}}\right)}{\left(1 + K_L \frac{P_{H_2O}}{P_{H_2}}\right)^2} \tag{4.36}$$

Chapter 5
Model Formulation

5.1 Introduction

In this chapter, a 1D steady-state model formulation of anode supported SOFC button cell with SDC based electrolyte is presented. This model was implemented in COMSOL Multiphysics, version 4.3b. COMSOL Multiphysics is a software for modeling and solving scientific and engineering problems based on partial differential equations using a finite element method.

This 1D model includes transport equations (mass and charge balance) and electrochemical reactions (H_2 oxidation at the anode and O_2 reduction at the cathode).

The model components for the 1D SOFC button cell are:

- Mass transport in the electrodes.
- Electrochemical reactions (global H_2 oxidation mechanism at the anode and global O_2 reduction at the cathode).
- Charge transport; ionic transport (in the electrodes and electrolyte) and electronic transport (in the electrodes).

The geometry of the button cell is as follows: 650 µm Nickel/Samaria-doped ceria (Ni/SDC) anode, 20 µm SDC electrolyte and 130 µm Strontium-doped samarium cobaltite/SDC (SSC/SDC) cathode. The diameter of the cathode layer is 6 mm and the diameter of the anode and electrolyte layers is 15 mm. The active area for the cell, based on the cathode surface area, is therefore 0.28cm^2.

The model assumptions are listed below:

(a) The button cell operates at steady state.
(b) The gas species are considered as ideal gases.
(c) The model is assumed isothermal.

(d) Convective fluxes in the porous electrode are neglected.

(e) Pressure gradients in the porous electrodes are neglected.

(f) The ionic and electronic conduction in electrodes are assumed to be uniform.

Reversible Fuel Cell Voltage:

The reversible fuel cell voltage (E^o), also referred to as reversible open circuit voltage (OCV) is defined as the potential difference between the anode and cathode when the electrochemical reactions occur reversibly. When H_2 or CO is used as a fuel, the reversible cell voltage, based on the Nernst equation, are expressed as (Li, 2006):

$$E^o_{H_2} = -\frac{1}{2F}\left[\Delta G_{H_2} + RTln\left(\frac{p_{H_2O}}{p_{H_2}p^{0.5}_{O_2,cat}}\right)\right] \quad (5.1)$$

$$E^o_{CO} = -\frac{1}{2F}\left[\Delta G_{CO} + RTln\left(\frac{p_{CO_2}}{p_{CO}p^{0.5}_{O_2,cat}}\right)\right] \quad (5.2)$$

where $E^o_{H_2}$ and E^o_{CO} are the reversible cell voltages involving H_2 and CO electrochemical reactions, respectively. $\Delta G_{H_2}$and ΔG_{CO} are the standard Gibb's energy for H_2 and CO oxidation reactions, respectively. R is the gas constant (8.314JK^{-1}mol^{-1}), T is the operating temperature (K), F is the Faraday's constant (96487 coulomb mol^{-1}), $p_{O_2,cat}$ is the oxygen partial pressure at the cathode side and $p_{H_2O}, p_{H_2}, p_{CO_2}, p_{CO}$ are the partial pressures of H_2O, H_2, CO_2,and CO at the anode side, respectively.

According to thermodynamic data from Daubert (1985) and Balzhiser et al. (1972), the semi-empirical form of $\Delta G^o_{rxn,T}$ for each electrochemical reaction is written as,

$$\Delta G^o_{rxn,T}\left(\frac{J}{mol}\right) = b_o + b_1 TlnT + b_2 T + b_3 T^2 + b_4 T^3 + b_5 T^4 + b_6 T^5 \quad (5.3)$$

where b_1, b_2, …, b_6 are constants depending on the oxidation reaction. These constants are determined thermodynamically using information shown in Table 5.1.

.

Table 5.1: Constant for the semi-empirical form of $\Delta G^{o}_{rxn,T}$

Reaction	b_o	b_1	b_2	b_3	b_4	b_5	b_6
H_2 oxidation	-239113	7.53	-10.79	8.57×10^{-3}	-6.64×10^{-6}	2.34×10^{-9}	-3.4×10^{-13}
CO oxidation	-282394	24.08	-50	-42.8×10^{-3}	17.3×10^{-6}	-4.92×10^{-9}	6.4×10^{-13}

SDC electrolyte is actually a mixed ionic- electronic conducting material (MIEC), because it not only conducts ion, but also the formation of Ce^{3+} cation results in electronic conduction. The ionic and electronic conductivity expressions for SDC are shown in equations 5.4 and 5.5, respectively (Cui et al, 2010):

$$\sigma_i = \sigma_{0,i} exp \frac{\left(-E_{a,i}/(kT)\right)}{T} \tag{5.4}$$

$$\sigma_e = \sigma_{0,e}\left(p_{O2,el}\right)^{-1/4} exp \frac{\left(-E_{a,e}/(kT)\right)}{T} \tag{5.5}$$

where $\sigma_{0,i}$ is the standard ionic conductivity, 1.65×10^{6} S Km^{-1}, $\sigma_{0,e}$ is standard electronic conductivity, 3.148×10^{12} S Km^{-1}, $E_{a,i}$ is activation energy for the ionic conductivity (0.5618eV), $E_{a,e}$ is activation energy for the electronic conductivity (2.8548eV), k is Boltzmann constant 1.38×10^{-23}J K^{-1}, and $p_{O2,el}$ is the local oxygen partial pressure.

The OCV for mixed conductor, OCV_{mix} is then calculated using equation 5.6 (Bove et al, 2005):

$$OCV_{mix} = \frac{E\sigma_i}{\sigma_e + \sigma_i} \tag{5.6}$$

where E is the reversible cell voltage which is calculated based on the Nernst equation (equations 5.1 and 5.2).

5.2 Mass Transport in Anode and Cathode

Mass transport is important to determine the species concentration profile within the porous electrodes. Inside the porous electrodes, the steady state mass transport equation is expressed as:

$$-\nabla . N_i + r_i = 0 \tag{5.7}$$

where N_i and r_i are molar flux of gas species (diffusion rate) and reaction rate inside the porous medium, respectively. The molar flux of the binary gas species inside the porous electrode was calculated based on Fick's law using effective diffusion coefficient for binary systems (i.e. H_2/H_2O and CO/CO_2), and using Stefan-Maxwell Model for multicomponent gas species systems (e.g. syngas composition).

For binary gas species, the molar flux of the gas inside the porous electrode was calculated based on Fick's law which considers both the molecular and Knudsen diffusions using an effective diffusion coefficient, D_i^{eff}.

$$N_i = -D_i^{eff} \nabla c_i \tag{5.8}$$

D_i^{eff} is defined as (Arpino et al., 2008; Suwanwarangkul et al., 2003):

$$D_i^{eff} = \left(\frac{1}{D_{im}^{eff}} + \frac{1}{D_{i,k}^{eff}} \right)^{-1} \tag{5.9}$$

D_{im}^{eff} and $D_{i,k}^{eff}$ are the effective molecular and Knudsen diffusion coefficients, respectively. D_{im}^{eff} is defined as:

$$D_{im}^{eff} = D_{ij} \frac{\varphi}{\tau} \tag{5.10}$$

where φ is the porosity of the porous structure, and τ is the tortuosity factor for molecular diffusion. This relation accounts for the complex pore structure inside the electrode material, where the diffusion path length along the pores is greater than the measurable electrode thickness. This is due to the pores' tortuous nature and pore constrictions, and thus the molecular diffusivity is corrected by a tortuosity factor and porosity (Aguiar et al., 2004).

In this study, the porosity was first calculated based on Bruggeman analytical expression as shown in equation 5.11 (Pharoah et al., 2006).

$$f(\varphi) = \varphi^{1.5} \tag{5.11}$$

D_{ij} is the binary diffusion coefficient. The Chapman-Enskog theory was applied to determine the binary diffusion coefficient (Reid et al., 1987; Yakabe et al., 2000, Geankoplis, 2003, Cayan et al., 2009):

$$D_{ij} = 1.858 \times 10^{-7} \frac{\left[T^3\left(M_i + M_j\right)/M_i M_j\right]^{1/2}}{p\sigma_{ij}^2 \Omega_D} \tag{5.12}$$

where σ_{ij} is the characteristics length, and Ω_D is the collision integral. Using the Lennard-Jones potential model, Ω_D is given by:

$$\Omega_{\mathrm{D}} = \frac{\mathrm{A}}{\mathrm{T_N^B}} + \frac{\mathrm{C}}{\exp(\mathrm{DT_N})} + \frac{\mathrm{E}}{\exp(\mathrm{FT_N})} + \frac{\mathrm{G}}{\exp(\mathrm{HT_N})} \tag{5.13}$$

where the constants *A* to *H* (Reid et al., 1987): *A* = 1.06036, *B* = 0.15610, *C* = 0.19300, *D* = 0.47635, *E* = 1.03587, *F* = 1.52996, *G* = 1.76474, *H* = 3.89411, and T_N is defined by

$$T_N = \frac{kT}{\varepsilon_{ij}} \tag{5.14}$$

where k is the Boltzmann constant and ε_{ij} is the characteristic Lennard-Jones energy.

σ_{ij} and ε_{ij} are given by

$$\begin{aligned} \sigma_{ij} &= \frac{\sigma_i + \sigma_j}{2} \\ \varepsilon_{ij} &= \left(\varepsilon_i \varepsilon_j\right)^{1/2} \end{aligned} \tag{5.15}$$

where σ_i is the diameter of the molecular collision. The values for σ_i and ε_i for gases of interest in this work are shown in Table 5.2.

Table 5.2: Values for σi and εi/k parameters for gases of interest in this work (Reid et al., 1987)

Gas species	σ_i (A^0)	ε_i/k (K)
H_2	2.827	59.7
H_2O	2.641	809.1
CO	3.690	91.7
CO_2	3.941	195.2
CH_4	3.756	148.6
N_2	3.798	71.4
O_2	3.467	106.7

The effective Knudsen diffusion coefficient was calculated using equation 5.16 (Cayan et al., 2009; Yakabe et al., 2000) :

$$D_{i,k}^{eff} = \frac{\varepsilon}{\tau}\bar{r}\frac{2}{3}\sqrt{\frac{8RT}{\pi M_i}} \tag{5.16}$$

Where $\bar{\boldsymbol{r}}$ is pore radius and M_i is molecular weight of species *i*.

For multicomponent systems, the steady state mass transport equation was expressed using the Stefan Maxwell Model:

$$-\nabla . N_i + r_i = 0 \tag{5.17}$$

$$N_i = -\left(\rho\omega_i \sum_i D_{ik}\mathbf{d}_k\right)$$

ρ is density in kg/m^3, ω_i is mass fraction of species *i*, $D_{ik}$is multicomponent diffusivities in m^2/s, $\mathbf{d}_k$ is the diffusional driving force acting on species *k* in (1/m).

$\mathbf{d}_k$=∇x_k, where $x_k = \frac{\omega_k}{M_k}M_n$

$M_n = \left(\sum_i \frac{\omega_i}{M_i}\right)^{-1}$ is the mean molar mass (kg/mol).

D_{ik} is the Maxwell-Stefan diffusivity matrix (m^2/s). For a simulation involving Q species, the Maxwell-Stefan diffusivity matrix is a Q by Q symmetric matrix, where the diagonal components are 1.

The binary diffusion for Maxwell-Stefan model was calculated using equation 5.18:

$$D_{ij} = 3.16 \times 10^{-8}[pa.\frac{m^2}{s}]\frac{T^{1.75}}{p\left(v_i^{1/3} + v_j^{1/3}\right)^2}\left[\frac{1}{M_i} + \frac{1}{M_j}\right]^{1/2} \quad (5.18)$$

p is the total pressure (Pa), v_i is molar diffusion volume of species i (m^3/mol), M_i is molecular weight (kg/mol), and T is the temperature (K). The diffusion volumes are given in Table 5.3.

Table 5.3: Gas Diffusion Volume (m^3/mol)

Species	Diffusion Volume (m^3/mol)
H_2	$7.1x10^{-6}$
H_2O	$12.7x10^{-6}$
CO	$18.9x10^{-6}$
CO_2	$26.9x10^{-6}$
CH_4	$24.4x10^{-6}$
N_2	$17.9x10^{-6}$

5.2.1 Reaction Rate Calculation

The reaction term in mass transport (equation 5.7) consists of chemical reaction and electrochemical reaction rate expressions. Both reaction expressions are discussed in the following section.

Chemical Reaction Rate

Global chemical reactions for methane steam reforming (MSR) and WGS reactions (on SDC and on Ni) were incorporated in the model simulating syngas operation. The reaction rate for the MSR and WGS on Ni are given as follows:

$$R_{WGSR} = k_{WGSR}\left(p_{CO}p_{H_2O} - \frac{p_{H_2}p_{CO_2}}{K_{eq,MSR}}\right) \tag{5.19}$$

$$R_{MSR} = k_{MSR}\left(p_{CH_4}p_{H_2O} - \frac{{p_{H_2}}^3 p_{CO}}{K_{eq,MSR}}\right) \tag{5.20}$$

where $k_{MSR}$and k_{WGSR} are rate constants of the MSR and WGSR, respectively. The correlations for the rate constants are given by Haberman and Young (2004) as:

$$k_{MSR} = 2.395 \times 10^{13}\exp(-\frac{231266}{RT}) \tag{5.21}$$

$$k_{WGSR} = 1.71 \times 10^{8} exp\left(-\frac{103191}{RT}\right) \tag{5.22}$$

$K_{eq,MSR}$ and $K_{eq,WGSR}$ are equilibrium constant for the MSR and WGSR, respectively. The correlation for these equilibrium constants are given as (Haberman and Young, 2004):

$$K_{eq,MSR} = 1.0267 \times 10^{10} \times \exp(-0.2513Z^4 + 0.3665Z^4 + 0.5810Z^2 - 27.134Z + 3.2770) \tag{5.23}$$

$$K_{eq,WGSR} = exp(-0.2935Z^3 + 0.6351Z^2 + 4.1788Z + 0.3169)$$

Where

$$Z = \frac{1000}{T(K)} - 1 \tag{5.24}$$

The reaction rate for WGS on SDC is shown in equation 4.36 in Chapter 4.

$$r_{s1} = \frac{k\left(P_{CO_2} - \frac{P_{H_2O}P_{CO}}{K_p P_{H_2}}\right)}{\left(1 + K_L\frac{P_{H_2O}}{P_{H_2}}\right)^2}$$

Electrochemical Reaction Rate

The current density at the electrodes is based on the Butler-Volmer equation, as shown in equation 5.25 (Shi et al., 2007):

$$J = i_o \left[\frac{c_{react}}{c^I_{react}} exp\left(\alpha \frac{n_e F \eta}{RT}\right) - \frac{c_{prod}}{c^I_{prod}} exp\left(-(1-\alpha)\frac{n_e F \eta}{RT}\right)\right] \quad (5.25)$$

where i_o is exchange current density, α is exchange transfer coefficient, F is Faraday constant, c_{react} is the reactant concentration in the electrode, c^I_{react} is the reactant concentration in the fuel stream, c_{prod} is the product concentration in the electrode, c^I_{prod} is the product concentration in the fuel stream, and η is local overpotential.

$$\eta = V_e - V_i - V_{ref} \quad (5.26)$$

V_{ref} is the relative potential difference between the electronic and ionic conductors at the reference state. OCV is chosen as the reference state where V_{ref} for anode is equal to zero, and V_{ref} for cathode is equal to the OCV.

The exchange current density at the anode for H_2 oxidation reaction, $i_{o,an,H2}$is expressed as in equation 5.27.

$$i_{o,an,H2} = \frac{\beta_{an,H_2} RT}{3F}\left(\frac{c_{H_2}}{c_{ref,H_2}}\right) exp\left(-\frac{E_{H_2}}{RT}\right)\left(p_{o_2,an,H2}\right)^{0.133} \quad (5.27)$$

β_{an,H_2} is an adjustable parameter to fit the experimental data and $p_{o_2,an,H2}$ is the oxygen partial pressure at the anode.

The exchange current density at the anode for CO oxidation reaction, $i_{o,an,CO}$ is expressed as in equation 5.28:

$$i_{o,an,CO} = \frac{0.3\beta_{an,CO} RT}{3F}\left(\frac{c_{CO}}{c_{ref,CO}}\right) exp\left(-\frac{E_{CO}}{RT}\right)\left(p_{o_2,an,CO}\right)^{0.133} \quad (5.28)$$

The exchange current density at the cathode for O_2 reduction, $i_{o,ca}$ is expressed as in equation 5.29 (Zhu et al., 2005)

$$i_{o,ca} = i^*_{O_2}\left[\frac{\left(p_{O_2}/p^*_{O_2}\right)^{1/4}}{1+\left(p_{O_2}/p^*_{O_2}\right)^{1/2}}\right] \quad (5.29)$$

$i^*_{O_2}$is a fitting parameter, $p_{O_2}$is the oxygen partial pressure inside the cathode, and $p^*_{O_2}$is expressed in Arrhenius form as follows:

$$p_{O_2}^{*} = A_{O_2}\exp(-\frac{E_{O_2}}{RT}) \tag{5.30}$$

$A_{O_2} = 9 \times 10^{13} Pa$, $E_{O_2} = 200\ kJ/mol$.

Table 5.4: List of boundary conditions for mass-transport

Boundary region	Boundary conditions
Fuel and air inlet	C_i=C_{inlet}
Electrode/Electrolyte interface	$\mathbf{n}.\vec{N}_i = 0$

5.3 Charge Transport

Charge transport plays an important role in estimating the ohmic overpotential inside the electrodes and the electrolyte. At the electrodes, both ionic and electron transports are considered. Electron transport depends on electric potential variations within the electron conducting phase, whereas ionic transport depends on electric potential variations within the ionic conducting phase. The charge balance can be expressed as:

$$\begin{pmatrix} Rate\ of\ accumulation \\ of\ electric\ charge \end{pmatrix} \tag{5.31}$$

$$= \begin{pmatrix} Net\ change\ of\ current \\ (IN - OUT) \end{pmatrix} + \begin{pmatrix} Rate\ of\ production \\ or\ consumption\ of \\ electric\ charge\ due \\ to\ electrochemical \\ reaction \end{pmatrix}$$

For the steady state process, this formulation can be expressed mathematically as

$$0 = \nabla.(J) + \dot{S}_c \tag{5.32}$$

where J is the current density and $\dot{S}_c$ is the rate of production or consumption of electric charge. Converting the current density into an electronic potential through the Ohm's law:

$$J = \sigma E = -\sigma \nabla V \tag{5.33}$$

where E is the electric field (V m^{-1}) and σ is the conductivity (S/m) will give:

$$\nabla.(-\sigma\nabla V) + \dot{S} = 0 \tag{5.34}$$

where is $\dot{S} = J \times S_{TPB}$, S_{TPB} being the triple phase boundary (TPB) active area per unit volume (m^2/m^3).

Ionic Charge Balance

In the cathode:

$$\nabla.(-\sigma_i^c\nabla V_i) + \dot{S}_c = 0 \tag{5.35}$$
$$\nabla.(-\sigma_i^c\nabla V_i) = -\dot{S}_c = -J_c S_{TPB}$$

In the anode:

$$\nabla.(-\sigma_i^a\nabla V_i) - \dot{S}_a = 0 \tag{5.36}$$
$$\nabla.(-\sigma_i^a\nabla V_i) = \dot{S}_a = J_a S_{TPB}$$

In the electrolyte:

$$\nabla.(-\sigma_i^e\nabla V_i) = 0 \tag{5.37}$$

Electron Charge Balance

At the cathode:

$$\nabla.(-\sigma_e^c\nabla V_e) - \dot{S}_c = 0 \tag{5.38}$$
$$\nabla.(-\sigma_e^c\nabla V_e) = \dot{S}_c = J_c S_{TPB}$$
$$\frac{\partial}{\partial z}\left(-\sigma_e^c\frac{\partial V_i}{\partial z}\right) + \frac{1}{r}\frac{\partial}{\partial r}\left(-r\sigma_e^c\frac{\partial V_i}{\partial r}\right) = J_c S_{TPB}$$

At the anode:

$$\nabla.(-\sigma_e^a\nabla V_e) + \dot{S}_a = 0 \tag{5.39}$$
$$\nabla.(-\sigma_e^a\nabla V_e) = -\dot{S}_a = -J_a S_{TPB}$$
$$\frac{\partial}{\partial z}\left(-\sigma_e^a\frac{\partial V_i}{\partial z}\right) + \frac{1}{r}\frac{\partial}{\partial r}\left(-r\sigma_e^a\frac{\partial V_i}{\partial r}\right) = -J_a S_{TPB}$$

The oxygen ion conductivity (S/cm) through pure SDC can be estimated as a function of temperature using equation 5.4.

The electronic conductivity (S/cm) through the Ni is calculated as:

$$\sigma_{e,Ni} = 3.27 \times 10^4 - 10.653T \tag{5.40}$$

The electronic conductivities (S/cm) through the SSC are based on Figure 5.1 (Hui et al., 2010):

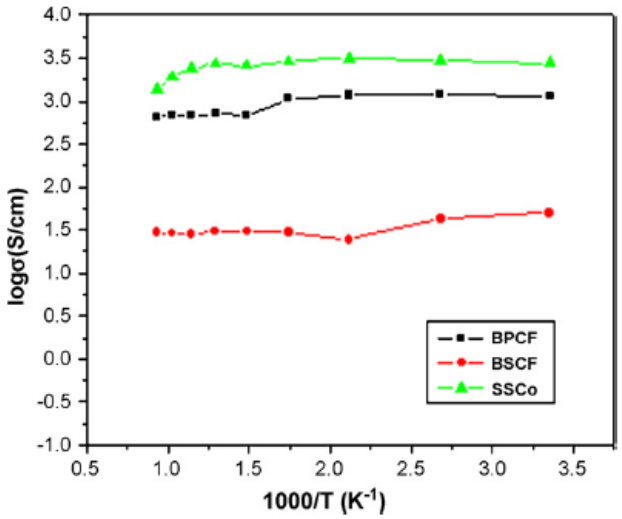

Figure 5.1: Electron conductivity of SSC (Hui et al., 2010)

The boundary conditions for ionic and electronic transport equations are given in Table 5.5 and Table 5.6 respectively.

Table 5.5: List of boundary conditions for the ionic transport equations

Boundary region	Boundary conditions
Interface of fuel channel and anode	$\mathbf{n}.\vec{J} = 0$
Interface of anode and electrolyte	Continuity
Interface of cathode and electrolyte	Continuity
Interface of air channel and cathode	$\mathbf{n}.\vec{J} = 0$

Table 5.6: List of boundary conditions for the electronic transport equations

Boundary region	Boundary conditions
Interface of fuel channel and anode	V_{an}
Interface of anode and electrolyte	$\mathbf{n}.\vec{J} = 0$
Interface of cathode and electrolyte	$\mathbf{n}.\vec{J} = 0$
Interface of air channel and cathode	V_{ca}

The model describes the implicit relationship between cell current and voltage. The model can be used to simulate steady-state current density-voltage-power curves by solving *J* when specifying E. In order to generate the full polarization curve, the calculation should be done over a range of cell voltages to calculate the corresponding average current density.

Chapter 6
SOFC Modelling, Calibration and Validation

In this chapter, the cell performance obtained from the model for various gas compositions were compared with experimental data. The gas compositions considered here were the followings: 97%H_2/3%H_2O, 20%CO/80%CO_2 and several syngas compositions (diesel, biomass, pre-reformed natural gas). The experiments were carried out by another PhD student from the SOFC group, Miss Asmida Ideris. The results were first validated against experimental results obtained with the H_2/H_2O system (where a few unknown microstructural parameters such as porosity and tortuosity were determined through fitting, as well as kinetics parameters for the H_2 electrochemical reaction), then with the CO/CO_2 system (where kinetics parameters for the CO electrochemical reaction were fitted), and finally with syngas (where no fitting was required). For the syngas compositions, a comparison with and without incorporating the WGS reaction on SDC were made. The kinetics parameters for the WGS on SDC were taken from the results shown in in Chapter 4.

The model input parameters for the simulation are summarized in Table 6.1.

Table 6.1: Simulation parameter at 700°C

	Value
Pressure	1 atm
Temperature (°C)	700, 650, 600
Fuel gas composition	Various mixtures of H_2, H_2O, CO, CO_2, CH_4, N_2
Oxidant	Air
Ionic conductivity of SDC (S/m)	2.7
Electronic conductivity of Ni (S/m)	$2.9x10^6$
Electronic conductivity of SSC (S/m)	$2.7x10^5$
Binary diffusivity of H_2-H_20 (m^2/s)	$6.95x10^{-4}$
Binary diffusivity of H_2-CO (m^2/s)	$5.87x10^{-4}$
Binary diffusivity of H_2-CO_2 (m^2/s)	$5.04x10^{-4}$

Binary diffusivity of H_2-CH_4 (m^2/s)	$6.00x10^{-4}$
Binary diffusivity of H_2-N_2 (m^2/s)	$5.44x10^{-4}$
Binary diffusivity of H_2O-CO (m^2/s)	$2.05x10^{-4}$
Binary diffusivity of H_2O-CO_2(m^2/s)	$1.67x10^{-4}$
Binary diffusivity of H_2O-CH_4 (m^2/s)	$2.12x10^{-4}$
Binary diffusivity of H_2O-N_2 (m^2/s)	$2.09x10^{-4}$
Binary diffusivity of CO-CO_2 (m^2/s)	$1.28x10^{-4}$
Binary diffusivity of CO-CH_4 (m^2/s)	$1.71x10^{-4}$
Binary diffusivity of CO-N_2 (m^2/s)	$1.62\ x10^{-4}$
Binary diffusivity of CO_2-CH_4 (m^2/s)	$1.42x10^{-4}$
Binary diffusivity of CO_2-N_2 (m^2/s)	$1.3x10^{-4}$
Binary diffusivity of CH_4-N_2 (m^2/s)	$1.74x10^{-4}$

6.1 H_2/H_2O Model Validation and Discussion

To calibrate this model, the following parameters were considered as free fit parameters: porosity, tortuosity and exchange current density fit parameter, $\beta_{an,H2}$. The best results, in term of good fit with the experimental results were obtained using the following values for the fitted parameters: porosity = 0.2, tortuosity = 13, $\beta_{an,H2} = 56 \times 10^5\ \Omega^{-1}m^{-2}$. A comparison between the model and experimental results using 3% humidified H_2 at three different operating temperatures (700, 650 and 600°C) is presented in Figure 6.1. The model results agree well with the experimental data at 700 and 650^{o}C while somewhat over predicted the experimental values at 600^{o}C, particularly at high current density.

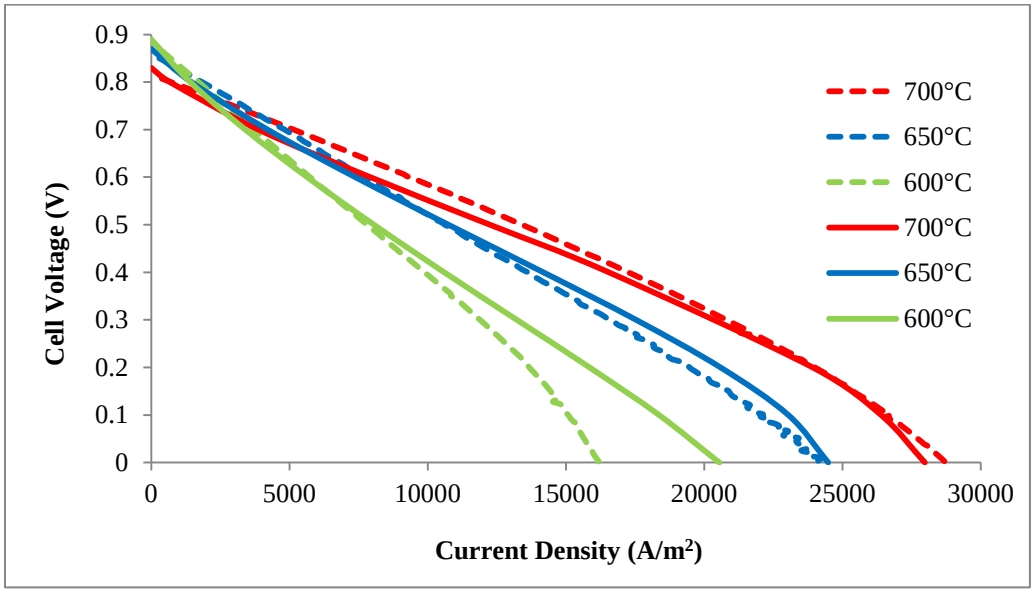

Figure 6.1: Experimental (dotted lines) and simulated (solid lines) cell performance using 3% humidified H2 as fuel source at 700, 650 and 600°C

The cell performance shown in Figure 6.1 agrees well with the theory where, as the temperature is increased, the current density should increase and the OCV should decrease. The molar fraction of H_2 and H_2O along the anode thickness when the cell was operated at 700°C at two different cell voltages (0.7 and 0.5 V) is depicted in Figure 6.2. For all Figures depicting some parameters along the anode thickness, the left hand side of such figure represents the interface between the fuel channel and the anode, whereas the right-hand side represents the interface between the anode and the electrolyte.

Because we used a button cell test station and thus used large excess of hydrogen, fuel consumption usually remains small, as seen in concentration profiles for H_2 and H_2O in Figure 6.2. As can be seen in Figure 6.2, the molar fraction gradient of H_2 and H_2O are greater at lower cell voltage (when the current density is higher) because more H_2 has been consumed and more H_2O has been generated at higher current density.

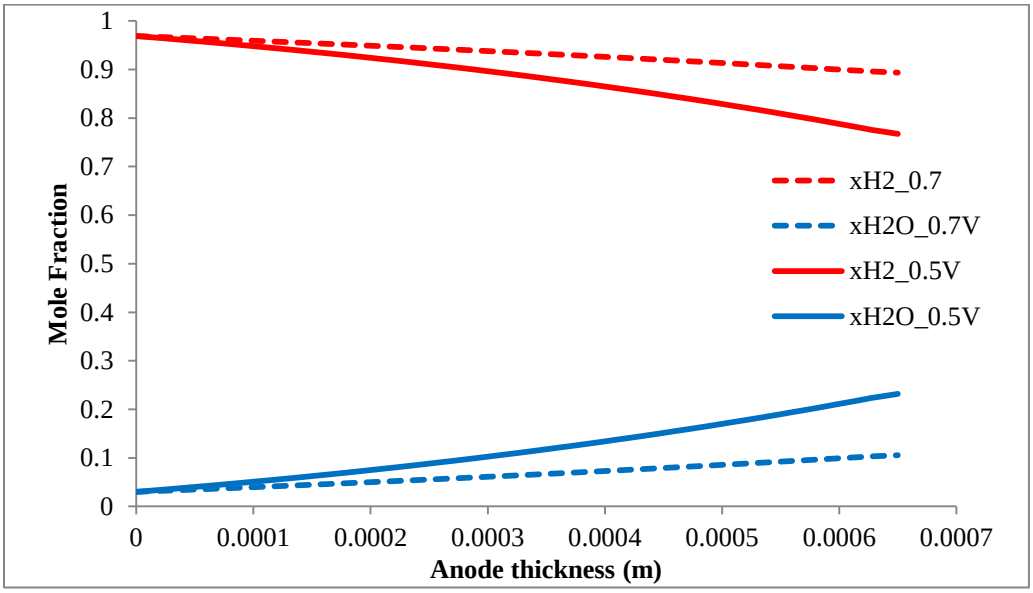

Figure 6.2: H_2 and H_2O molar fractions at 700°C for two different cell voltages (0.7 and 0.5V)

The oxygen molar fraction along the cathode thickness follows the expected trend where O_2 concentration should decrease more at higher current density (i.e. lower cell voltage), as shown in Figure 6.3 for an operating temperature of 700°C.

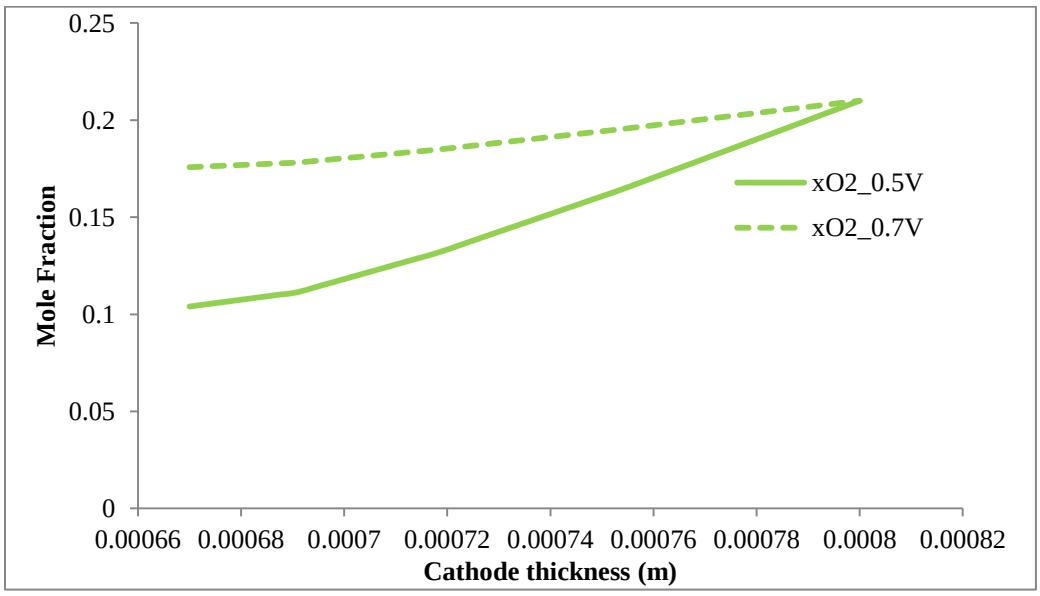

Figure 6.3: O_2 molar fractions at 700°C for two different cell voltages (0.7 and 0.5V)

For all Figures depicting some parameters along the cathode thickness, the left hand side of such figure represents the interface between the electrolyte and the cathode, whereas the right-hand side represents the interface between the cathode and the air channel.

Figures 6.4 and 6.5 show the H_2 and O_2 molar fraction along the anode and cathode thickness, respectively, for three different temperatures at a cell voltage of 0.5V. As expected, H_2 and O_2 were consumed more at higher temperatures. This is due to the higher current density generated at higher operating temperature. As a result, more H_2O was produced at higher temperature.

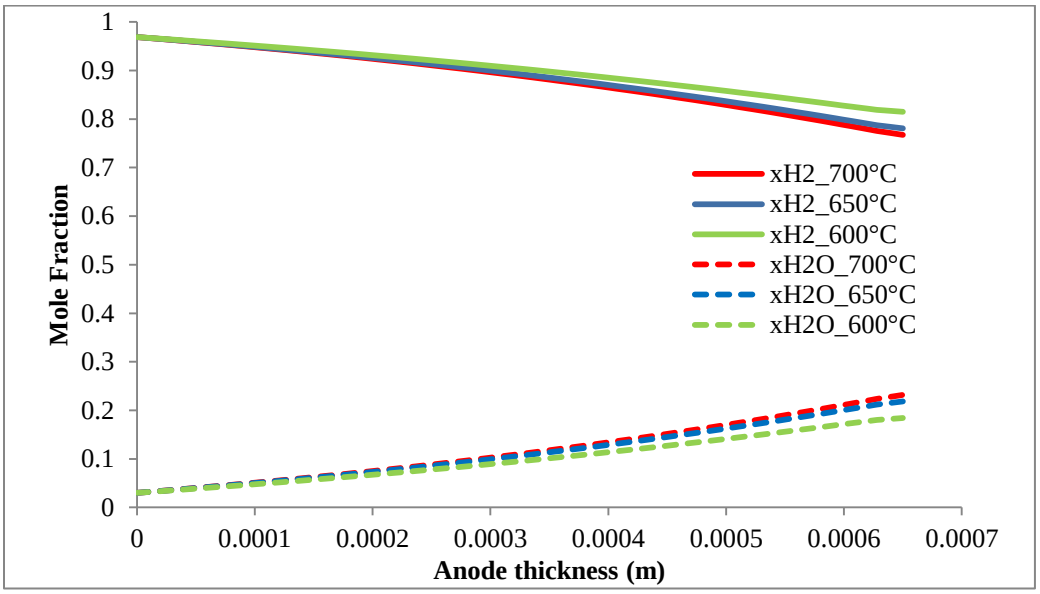

Figure 6.4: H_2 and H_2O molar fractions at a cell voltage of 0.5 V for three different temperatures

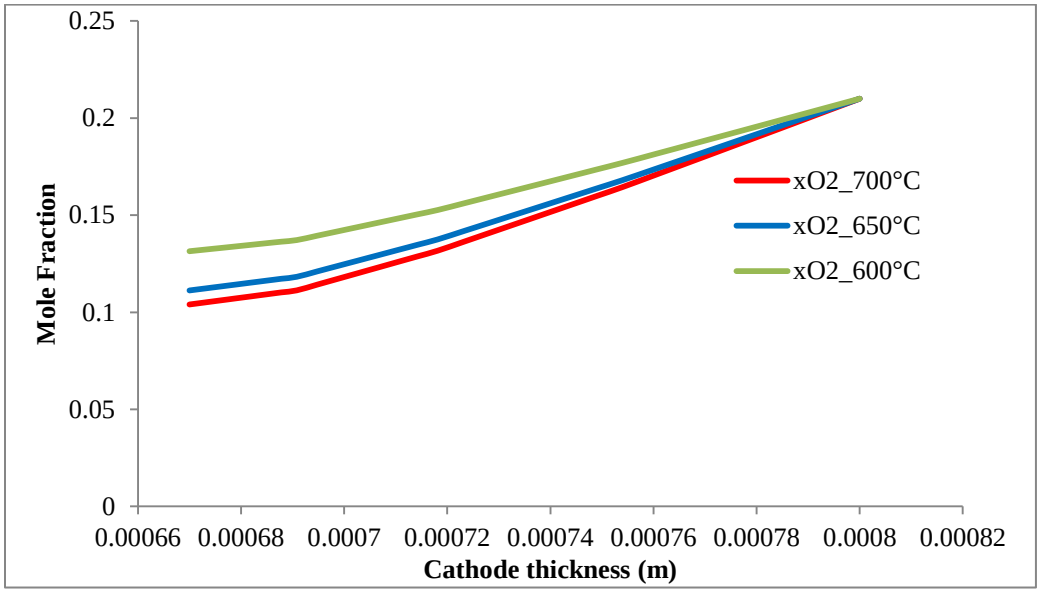

Figure 6.5: O_2 molar fractions at a cell voltage of 0.5 V for three different temperatures

Figure 6.6 gives the profile of local current density in the case of humidified hydrogen at 700°C. This shows that the current is generated within a distance of 40 μm from the electrolyte, with 80% of the current being generated in the first 10 μm away from the electrolyte.

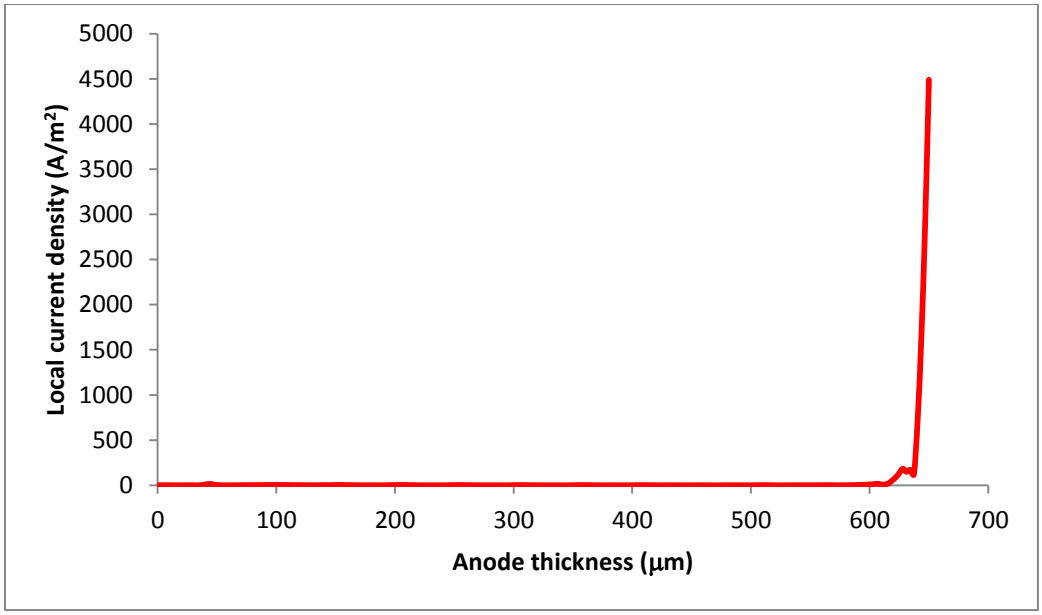

Figure 6.6: local current density profile along the anode thickness for humidified H_2 at 700°C.

6.2 CO/CO_2 Model Validation and Discussion

The cell microstructure parameters determined using the H_2/H_2O system were kept the same for the CO/CO_2 modelling, as well as for syngas modelling. For the CO/CO_2 system, only one kinetic parameter related to CO electrochemical oxidation was considered as free fit parameters, that is the exchange current density fit parameter, $\beta_{an,CO}$ ($\Omega^{-1}m^{-2}$). Comparison between model and experimental results (polarization curve) is depicted in Figure 6.7 for a gas composition of 20%CO/80%CO_2 at three different operating temperatures (700, 650 and 600°C). The composition 20%CO/80%CO_2 was chosen because thermodynamics calculations indicated that carbon deposition through the Boudouard reaction should not be favoured, which was particularly important for the experiments.

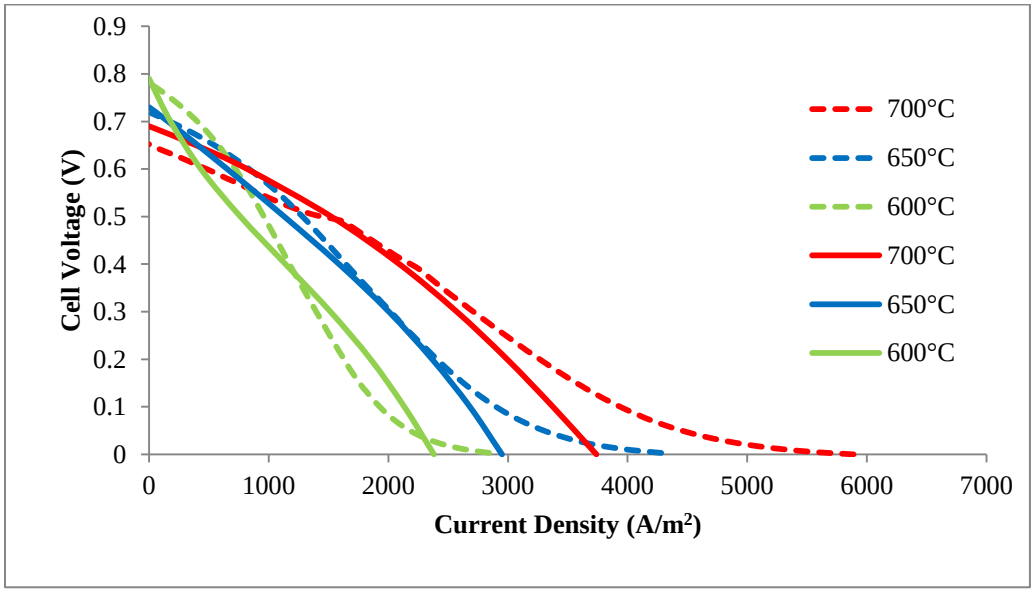

Figure 6.7: Experimental (dotted lines) and simulated (solid lines) cell performance using 20%CO/80%CO_2 at 700, 650 and 600°C

The experiments for the CO/CO_2 system showed a trend at high current density that was different from what was observed for the H_2/H_2O, and even the syngas systems; instead of the voltage to rapidly drop at high current density, the rate of voltage drop actually decreased at those high current densities. The experiments with CO/CO_2 were repeated and that trend at high current density remained consistent. At the present time, the reason for this

experimental observation is not clear. The way the button cell model was developed was such that it cannot represent such a trend. This is why the discrepancies between experimental and simulation results increases when increasing the current density. For current densities up to ~2500 A/m^2 (i.e. voltage between 0.2 and 0.8V) the simulation results show good agreement with the experimental data at 700 and 650°C. The fit between simulation and experimental results at 600°C was not as good: the simulation shows a much faster decrease in voltage than the experiment does at low current densities.

The molar fraction for CO and CO_2 inside the anode operating at 700°C for two different cell voltages (0.5V and 0.7V) is plotted in Figure 6.8. A cell voltage of 0.7 V corresponds to a relatively small current density (20A/m^2), and this why very little CO is consumed throughout the cell. For a cell voltage of 0.5 V, the CO consumption was more noticeable.

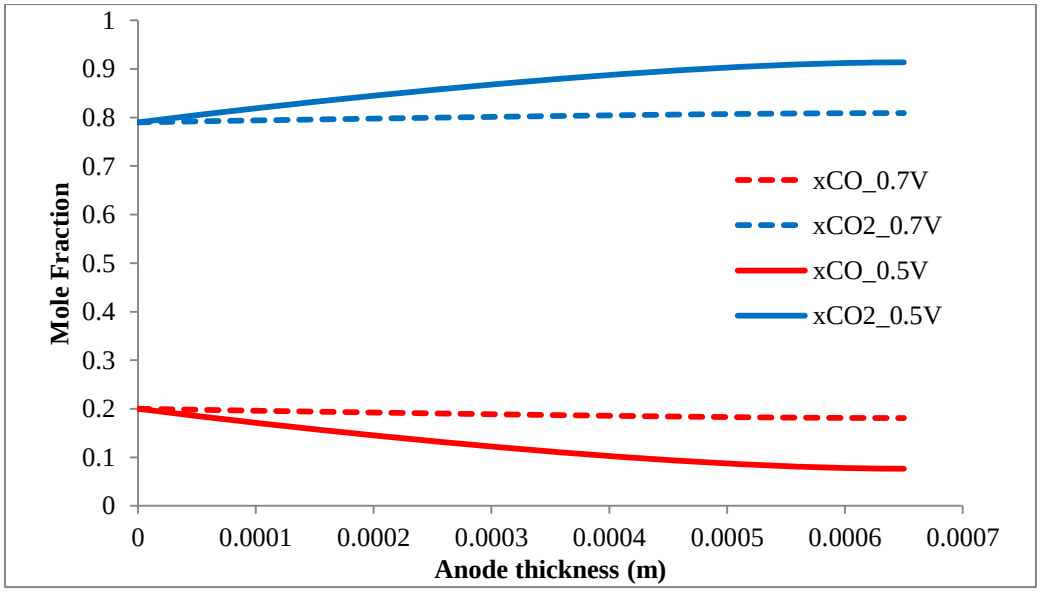

Figure 6.8: CO and CO_2 molar fractions at 700°C for two different cell voltages (0.7 and 0.5V) and a feed gas composition of 20%CO/80%CO_2

The profile of the O_2 molar fraction along the cathode is shown in Figure 6.9. Not surprisingly, the gradient of O_2 concentration increases as the current density increases (or cell voltage decreases).

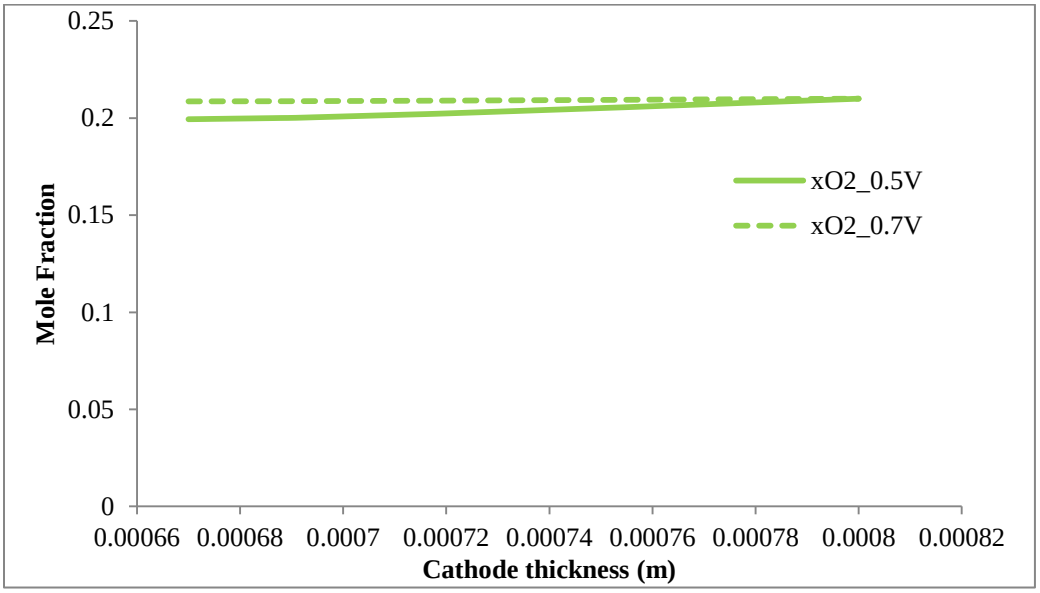

Figure 6.9: O_2 molar fraction at 700°C for two different cell voltages (0.7 and 0.5V) and a feed gas composition of 20%CO/80%CO_2

Figures 6.10 and 6.11 show the molar fractions along the anode and cathode thicknesses, respectively, for three different temperatures (600, 650 and 700°C) at a cell voltage of 0.5V. Because of higher current density at higher temperature, the consumption of CO and O_2 increases as the temperature increases. Consequently, more CO_2 is produced at higher temperatures.

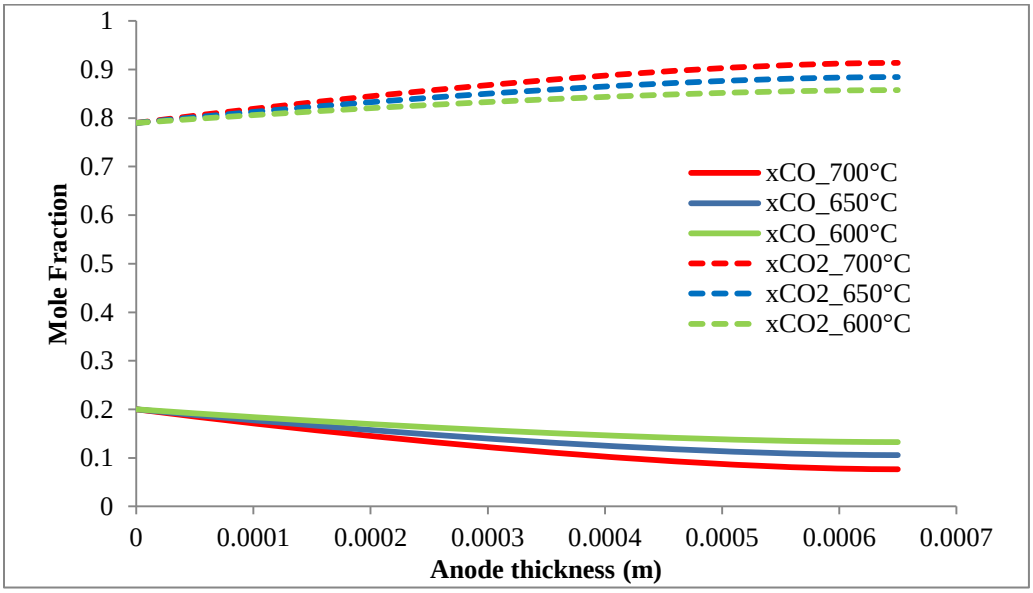

Figure 6.10: CO and CO_2 molar fractions at a cell voltage of 0.5V for three different temperatures and for a feed gas composition of 20%CO/80%CO_2

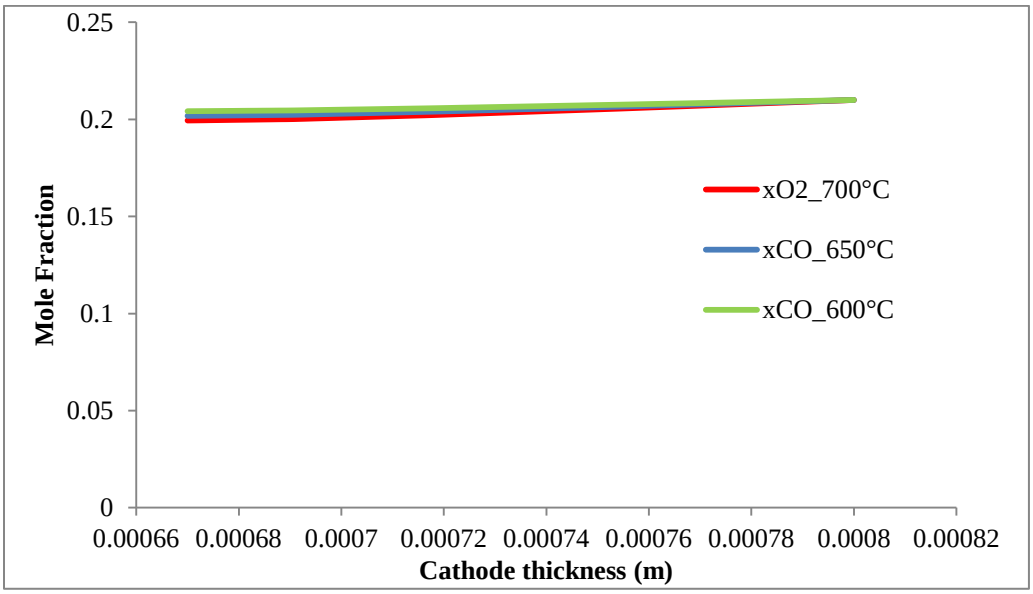

Figure 6.11: O_2 molar fractions at a cell voltage of 0.5V for three different temperatures and for a feed gas composition of 20%CO/80%CO_2

6.3 Comparison between H_2 and CO Electrochemical Oxidation

There have been debates in the literature regarding the relative importance of the CO electrochemical oxidation compared to that of H_2. Some authors considered that CO electrochemical oxidation is much slower than that of H_2 and when doing cell modeling, CO is assumed to be consumed only through the water-gas shift reaction. Other authors consider that the rate of CO electrochemical oxidation is of the same order of magnitude as that of H_2, or eventually a bit lower, in which case CO electrochemical oxidation is usually considered in cell modeling. Note that the above discussion is only for Ni/YSZ, as to our knowledge, we have not seen such discussion in the case of Ni/SDC anode.

Figure 6.12 shows a comparison between the polarization curves obtained for 20%H_2/80%H_2O and for 20%CO/80%CO_2 at three different temperatures. It is clear from this figure that the performance with H_2 is considerably higher than with CO. For example, the limiting current density at 600°C is about 4 times greater with H_2 than with CO, whereas at 700°C it is close to being 3 times higher.

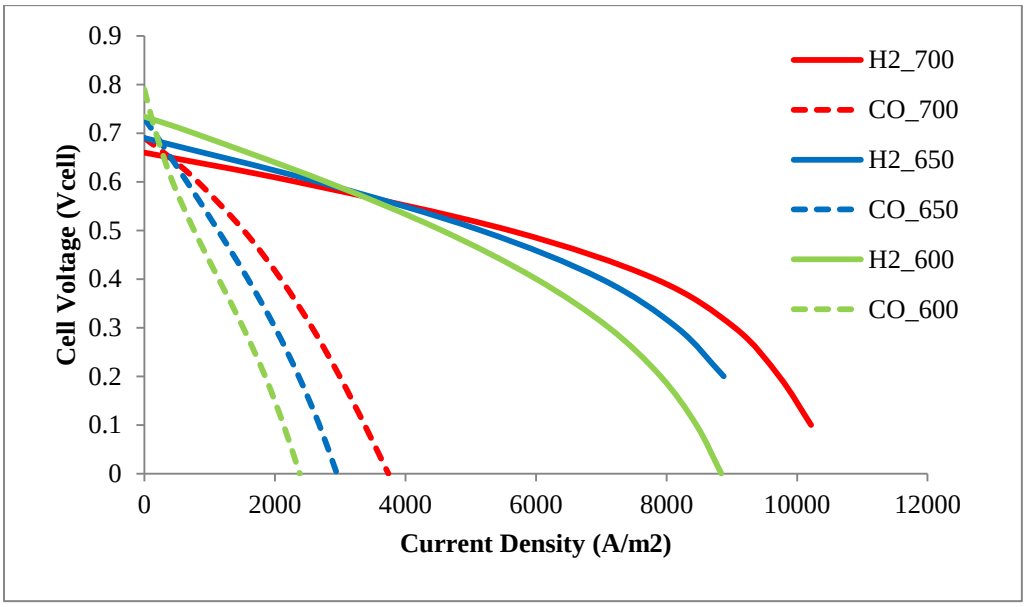

Figure 6.12: Polarization curve for 20%H_2/80%H_2O (shown as "H_2" in the figure legend) and for 20%CO/80%CO_2 (shown as "CO" in the figure legend)

6.4 Syngas Model Validation and Discussion

For the syngas modelling, three different compositions were selected depending on whether the syngas originates from diesel reforming, natural gas pre-reforming or biomass gasification (Aravind et al., 2001). The pre-reformed natural gas syngas composition corresponds to the case part of the exhaust from the anode side is used to pre-reform the feed natural gas (see W. Zhang, 2006). The composition for each syngas is listed in Table 6.2:

Table 6.2: Species composition of syngas

	Species Composition (%)					
	H_2	H_2O	CO	CO_2	CH_4	N_2
Diesel	65.0	3.0	21.4	8.3	2.3	-
Natural gas	28.1	27.3	6.2	22.8	9.5	6.1
Biomass	20.0	2.5	20	12	2.5	43

The cell performance (polarization curve) obtained from the simulation for these syngas compositions were compared with the experimental performance at 700°C and is presented in Figure 6:13. Note that the simulation results presented in Figure 6.13 take into account the WGS reaction over SDC, using the rate expression derived in Chapter 4. Since, methane was present in those compositions, albeit in small amount, methane steam reforming was also considered in those simulations, using the rate expression found in Haberman and Young (2004). Also, recall that no parameters were fitted for the syngas simulation; the parameters determined in sections 6.1 and 6.2 were kept the same here.

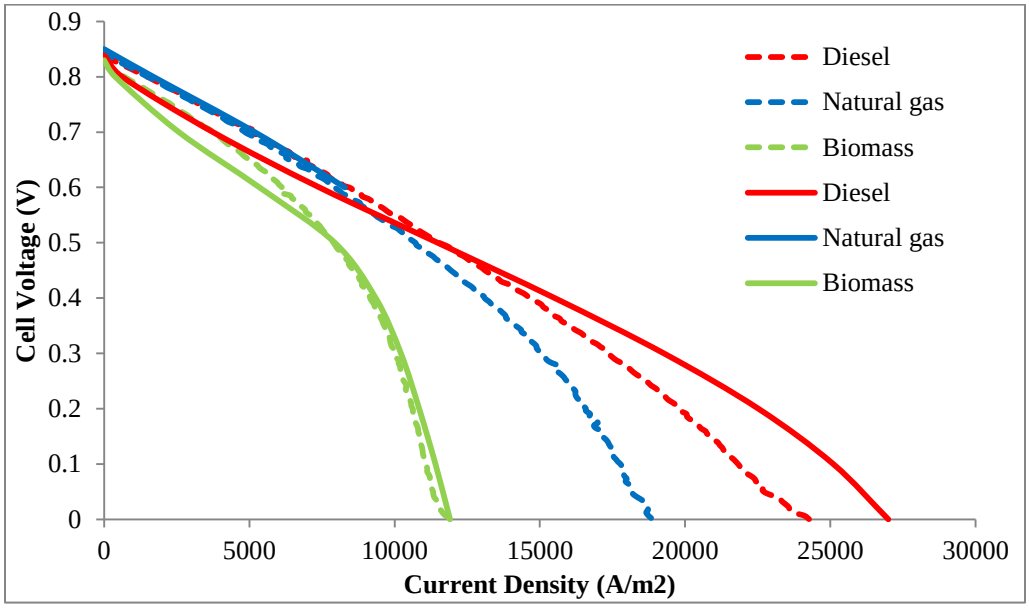

Figure 6.13: Experimental (dotted lines) and simulated (solid lines) cell performance for syngas from diesel, pre-reformed natural gas and biomass gasification at 700°C

The results for pre-reformed natural gas fit the experimental data very well for a current density up to 10,000 A/m^2. Unfortunately, the model failed to converge at current densities greater than 10,000 A/m^2. For biomass syngas, the model results fit the experimental data very well, especially at high current density, but somewhat underestimate the experimental data at lower current density. Larger discrepancies between the model results and experimental data were observed for diesel syngas, especially at higher current density. One possible reason of the over prediction of cell voltage at high current density may be due to eventual carbon deposition that may have reduced the pore size, hence affecting the transport of species, especially at higher current density. Carbon deposition effects were not included in the model.

Diesel syngas yielded the highest cell performance due to higher H_2 content (65%) than in pre-reformed natural gas (28.1%) or biomass syngas (20%). H_2 is the most effective fuel for fuel cell operation. Biomass syngas produced the lowest current density because it contains the lowest H_2 and highest N_2 contents. N_2 contributed to fuel dilution in the fuel cell as well

as to reduce gas diffusion inside the anode. Even though the biomass syngas contains more CO (20%) than the pre-reformed natural gas syngas (6.2%), it produced a lower current density because the pre-reformed natural gas syngas also contains more CH_4 and H_2O in the fuel. Therefore, methane steam reforming was more active and produced more H_2 (and CO) via MSR and WGS reactions.

As shown in chapter 4, SDC itself is active toward the water-gas shift (WGS) reaction. Simulation considering WGS only on Ni (which has been the common way in the literature to take into account the WGS reaction) showed that in the conditions considered here, the WGS does not reach equilibrium. This means that adding another WGS reaction term representing this reaction on SDC could potentially affect the simulation results. Therefore, simulations with and without the term representing the WGS reaction on SDC had been performed and the results are shown in Figure 6.14.

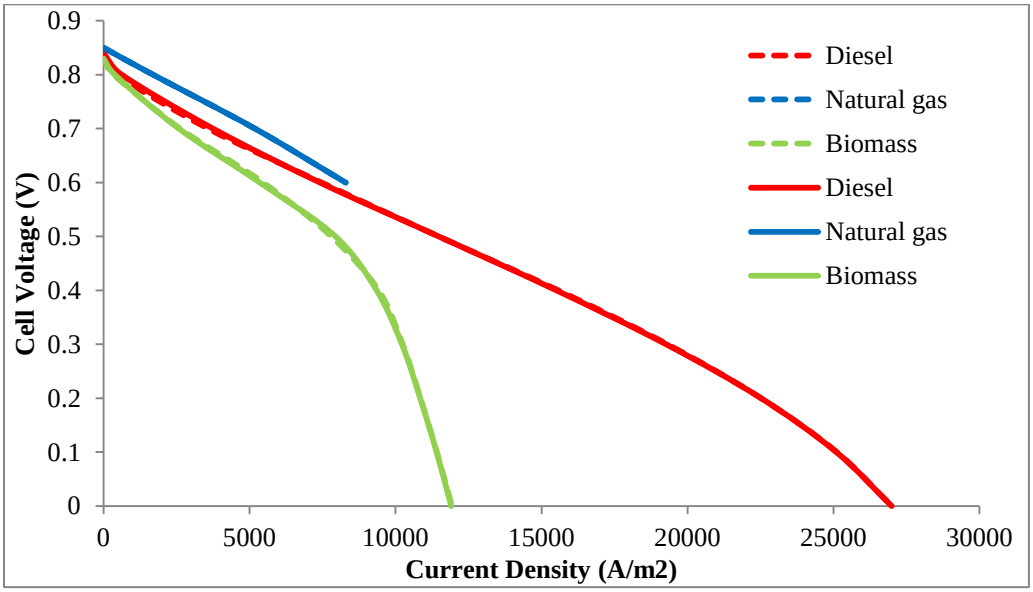

Figure 6.14: Simulation results without WGS on SDC (dotted lines) and with WGS on SDC (solid lines) at 700°C

Figure 6.14 shows that adding the term for the WGS reaction on SDC does not make any difference on the polarization curve. This finding looks contradictory to the findings from Chapter 4 where SDC itself was active toward the WGS reaction. To understand the reason behind this, the profile of molar fractions of H_2 and CO, profile of the WGS reaction quotient $[(P_{H2}*P_{CO2})/(P_{CO}/P_{H2O})]$ and profile of reaction rates of WGS on SDC and on Ni will be discussed next. These plots are for biomass and diesel syngas composition at 700°C and at two different cell voltages (0.7V and 0.4V) and for pre-reformed natural gas at only a cell voltage of 0.7V since the simulation could not converge for a cell voltage of 0.4V.

The simulated molar fractions of H_2 and CO for biomass syngas, diesel syngas and pre-reformed natural gas are plotted in Figures 6.15 and 6.16, respectively, for cases with and without WGS on SDC.

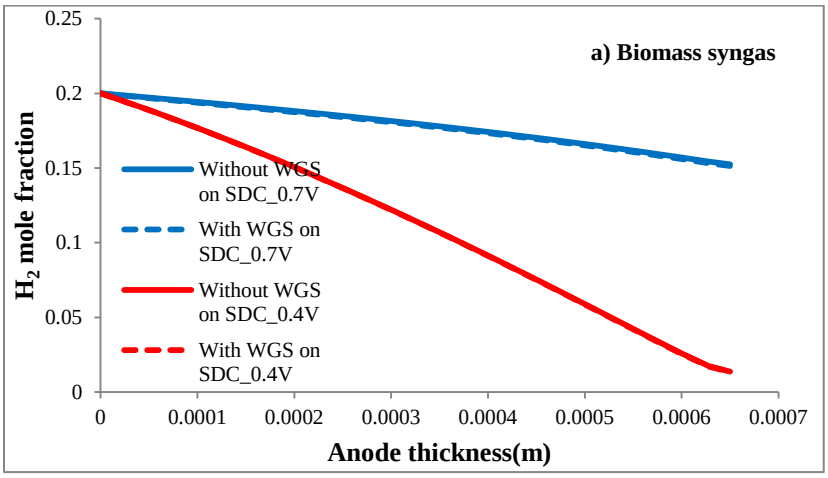

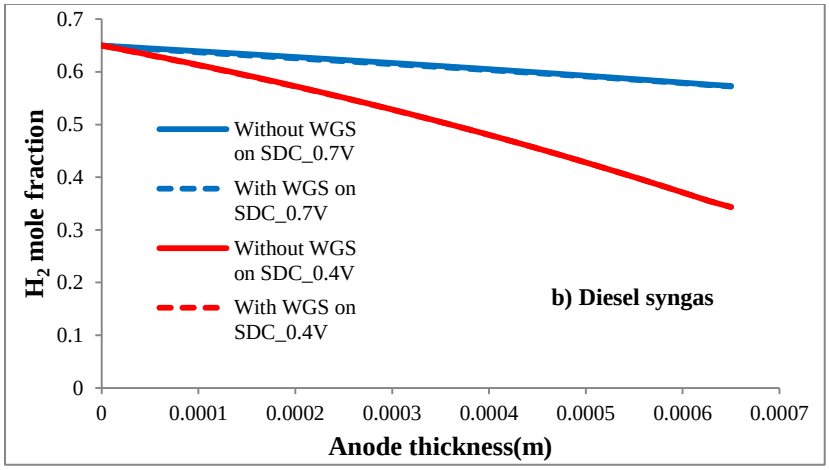

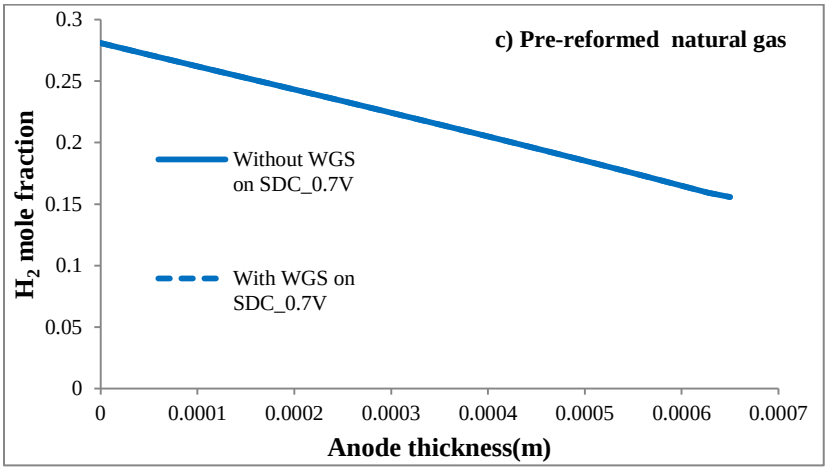

Figure 6.15: H_2 mole fraction without WGS on SDC (solid lines) and with WGS on SDC (dotted lines) incorporation at 700°C and at two different cell voltages (0.7V and 0.4V). a) biomass syngas, b) diesel syngas, c) pre-reformed natural gas

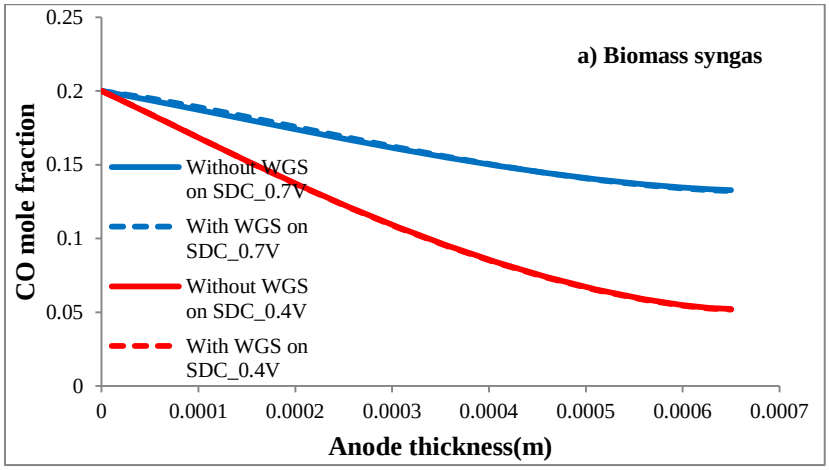

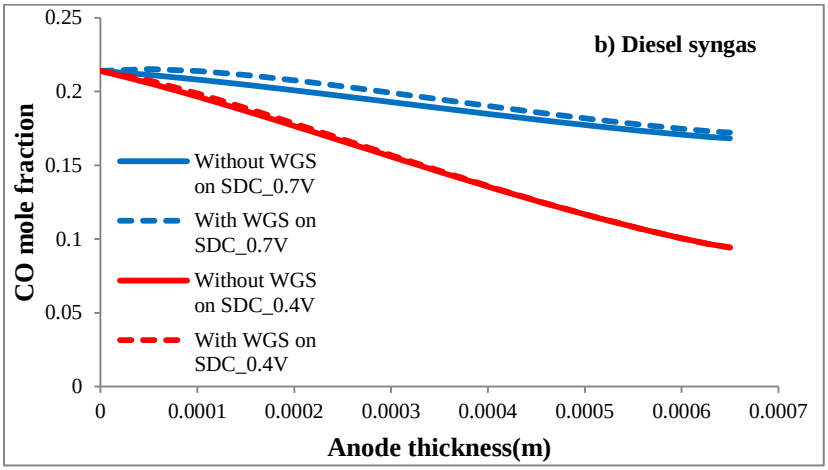

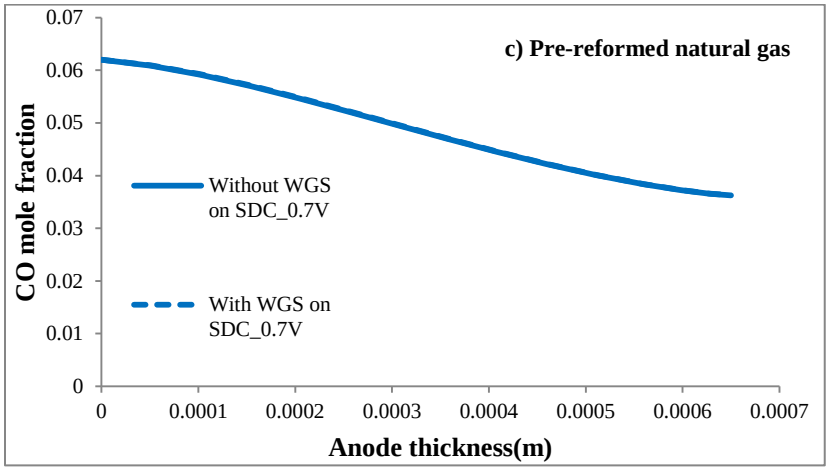

Figure 6.16: CO mole fraction without WGS on SDC (solid lines) and with WGS on SDC (dotted lines) incorporation at two different cell voltages (0.7V and 0.4V). a) biomass syngas, b) diesel syngas, c) pre-reformed natural gas.

From Figure 6.15 it is clear that the inclusion of the WGS on SDC does not make much difference for H_2 mole fraction for all fuels considered. From Figure 6.16, there are also no differences in CO mole fraction for biomass syngas and pre-reformed natural gas, no matter the cell voltage, whether the WGS on SDC in included or not. However, Figure 6.16b indicates that, in the case of diesel reforming, inclusion of the WGS on SDC for a cell voltage of 0.7 V does have an effect on the CO mole fraction, which it is slightly higher than without WGS on SDC. This actually means that the reaction that actually occurs is the reverse WGS, as confirmed by the negative value of the rate of the WGS reaction seen in Figure 6.18b. The reason why the WGS reaction on SDC had a more noticeable effect on the CO mole fraction for diesel syngas at 0.7 V and not for biomass syngas and pre-reformed natural gas is likely because the composition of the diesel syngas is such that the driving force for the reaction to proceed in the reverse WGS direction is greater than for the other two syngas compositions. This is actually confirmed by looking at the reaction quotient for the reverse WGS reaction $[(P_{H2}*P_{CO2})/(P_{CO}/P_{H2O})]$ plotted in Figure 6.17: indeed this reaction quotient is much greater through most of the anode for the diesel syngas than for the biomass syngas and pre-reformed natural gas. Higher reaction quotient for the reverse WGS means

greater tendency for the reaction to proceed in the direction of the reverse WGS. Comparison between the three figures in Figure 6.17 shows that, at 0.7 V, the effect of the WGS on SDC increases as the reaction quotient increases: this effect is indeed greatest for diesel syngas, followed by biomass syngas and finally by pre-reformed natural gas, with value of reaction quotient at the fuel channel/anode interface of 8.4, 4.7 and 3.8 respectively. To bring those numbers into perspective, the equilibrium constant (i.e. reaction quotient at equilibrium) is 1.6 at 700°C.

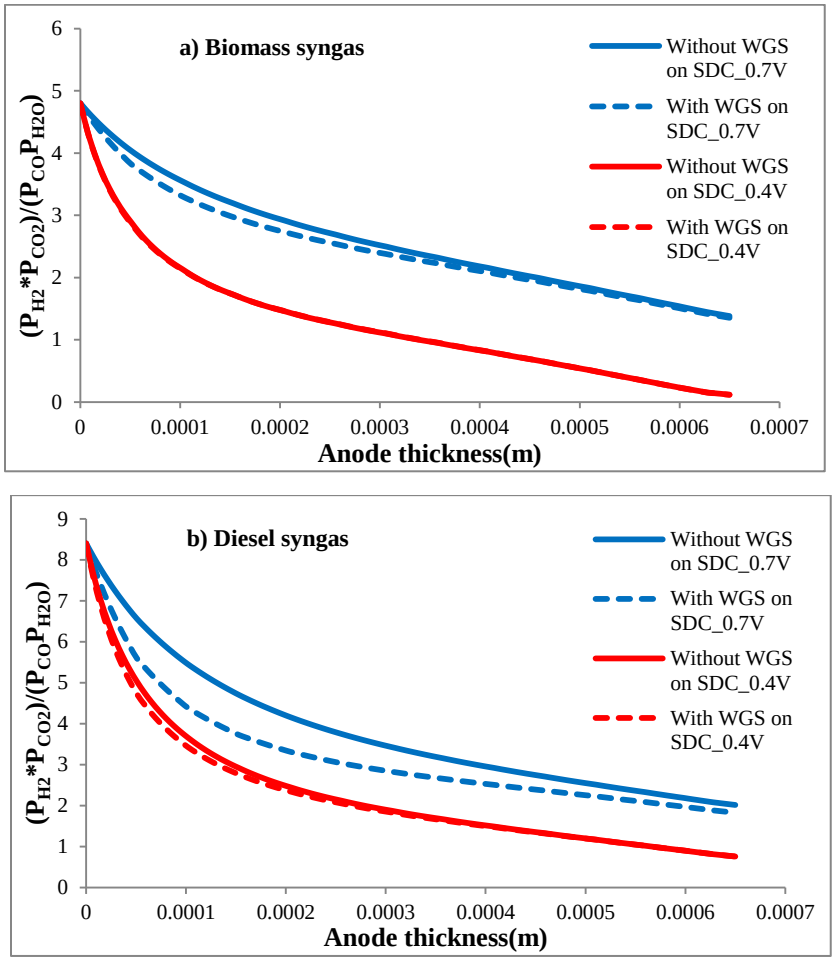

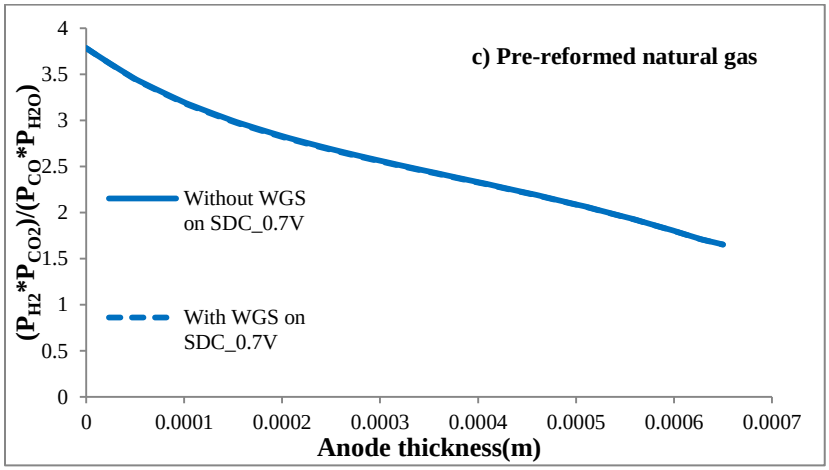

Figure 6.17: Reaction quotient without WGS on SDC (solid lines) and with WGS on SDC (dotted lines) at 700°C and for two different cell voltages (0.7V and 0.4V). a) biomass syngas, b) diesel syngas, c) pre-reformed natural gas

From Figure 6.17, it can be seen that near the anode/electrolyte interface (right-hand side of the figure), the reaction quotient at a cell voltage of 0.7 V is much closer to the equilibrium value (1.6) in all syngas cases; the values of the reaction quotient at the electrolyte interface being equal to 1.4, 1.9 and 1.7 for biomass syngas, diesel syngas, and pre-reformed natural gas, respectively. It can thus be assumed that the WGS reaction was closed to equilibrium at the TPB for a cell voltage of 0.7 V at 700°C. Except for pre-reformed natural gas (reaction quotient closes to equilibrium), one would remark that incorporation of the WGS on SDC did make a small difference regarding the reaction quotient during approximately the first half section of the anode, where the WGS on SDC helped to bring the reaction quotient closer to its equilibrium value. At a cell voltage of 0.4V, the effect of the WGS on SDC could be seen only for the diesel syngas, again because it corresponded to the initial reaction quotient furthest away from equilibrium. At 0.4 V, the WGS reaction does not reach equilibrium near the anode/electrolyte interface, where the reaction quotient is much lower than the equilibrium value of 1.62 (reaction quotient values of 0.1 and 0.8 for biomass and diesel syngas, respectively). This is likely due to the large amount of H_2O produced. Since the WGS is far from equilibrium, one would expect that the addition of another term describing

the WGS reaction, should make a difference. However, as seen in Figure 6.17, inclusion of the water gas shift reaction at 700°C and cell voltage of 0.4V did make no (case of biomass syngas) or little difference (case of diesel syngas).

The fact that inclusion of the WGS reaction on SDC does not make much difference points out to the possibility of this reaction to occur at a much lower rate than the WGS on Ni. The WGS reaction rates on SDC and on Ni are shown in Figure 6.18. Negative values of the WGS reaction indicate that the reaction proceeds in the direction of the reverse WGS reaction. Figures 6.18a and 6.18b show that near the fuel channel (left-hand side of the figure), the WGS over SDC dominates for both biomass and diesel syngas, and this at cell voltage of 0.7 and 0.4 V, where the absolute value of the WGS rate is indeed greater over SDC than over Ni. In the case of pre-reformed natural gas, the opposite was observed, that is the WGS reaction over Ni dominated compared to that over SDC. The reader should be cautioned to pay attention to the y-axis value when comparing the three fuels. For a cell voltage of 0.7V, near the anode/electrolyte interface, the rates of WGS over SDC and over Ni are of the same order of magnitude for both biomass and diesel syngas fuels. Recall that in this case, the reason why inclusion of WGS on SDC did not make any difference was because that reaction was closed to equilibrium at the TPB. However, for a cell voltage of 0.4 V, and for both biomass and diesel syngas, near the TPB, the rate of the WGS over Ni is much higher than that over SDC, which explains why the inclusion of the WGS on SDC did not show any difference in the polarization curve.

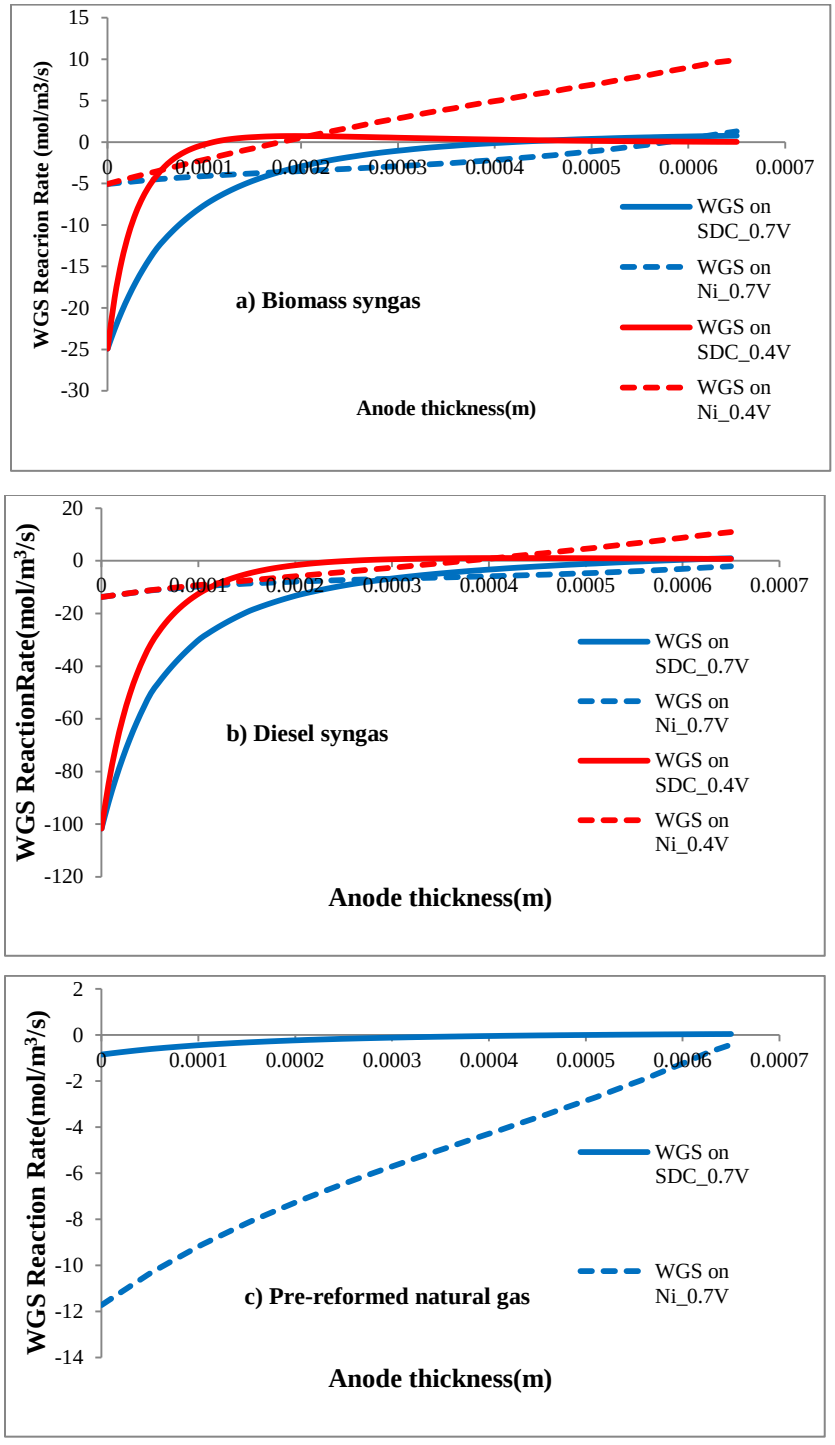

Figure 6.18: Reaction rate of WGS on SDC (solid lines) and reaction rate of WGS on Ni (dotted lines) at 700°C and at two different cell voltages (0.7V and 0.4V). a) biomass syngas, b) diesel syngas, c) pre-reformed natural gas

One would remark from Figure 6.18 that for all cases, the rate of the WGS on SDC becomes very small near the anode/electrolyte interface, where most of the reaction products from the electrochemical reactions (H_2O and CO_2) are produced. It remains unclear whether the results obtained are indeed a true representation of the reality or if it is an artefact due to the expression of the WGS (or reverse WGS) rate. Mathematically, the reverse WGS reaction rate is represented by:

$$r_{s1}=k\left(P_{CO_2}-\frac{P_{H_2O}P_{CO}}{K_pP_{H_2}}\right)/\left(1+K_L\frac{P_{H_2O}}{P_{H_2}}\right)^2 \qquad (6.1)$$

In the denominator, the ratio P_{H2O}/P_{H2} is very important because, as this ratio increases, the rate will decrease (all the more important that there is a square in the denominator). As the cell voltage decreases, along with current density increase, there is a higher conversion of H_2 to H_2O (as well as CO to CO_2) and thus an increase in the P_{H2O}/P_{H2} ratio. Because of experimental limitation when studying the kinetics of the WGS reaction over SDC, the highest P_{H2O}/P_{H2} possible was 0.21. For the cell voltage of 0.7V, the maximum P_{H2O}/P_{H2} was well within the limit of validity of the WGS on SDC rate expression. However, for higher current density, as it was the case corresponding to cell voltage 0.4 V, the maximum P_{H2O}/P_{H2} was well above the value of 0.21, which leads to question the validity of our rate expression under these conditions. This does not necessarily mean that at higher P_{H2O}/P_{H2} ratio, WGS on SDC is not important, but this points to the need of expanding the limit of validity of the rate expression, especially to higher water content.

Chapter 7
Conclusions and Recommendations

7.1 Conclusions

Methane Steam reforming on YSZ/Ni-YSZ and SDC/Ni-SDC

- Experiments were carried out on a fixed bed reactor to investigate the activity of YSZ and SDC electrolytes toward methane steam reforming (MSR). The MSR results indicated very similar low activities between the two electrolyte materials: methane conversion for the two materials varied from ~0% at 650°C to about ~2-3% at 750°C.

- It was expected that methane steam reforming on Ni-YSZ and Ni-SDC should yield similar performance. However, Ni-YSZ showed different conversions than Ni-SDC where H_2 yield was higher for Ni-SDC than for Ni-YSZ (the opposite trend was observed for the CO yield). These results pointed out to differences in activity toward the water-gas shift (WGS) reaction or reverse water-gas shift (RWGS) reaction, which was confirmed experimentally: for the RWGS reaction, SDC was more active than YSZ.

- To test the different activities toward WGS reactions between SDC and YSZ, reverse WGS experiments were conducted at 650, 700 and 750°C over SDC and YSZ materials in the absence of Ni catalyst at three different H_2/CO_2 ratios (1, 3 and 4) for 20 hours. The results indicate that SDC is more active towards the reverse WGS reaction compared to YSZ at all temperatures and H_2/CO_2 ratios, with CO_2 conversion on SDC being about 1.4-2.5 higher than CO_2 conversion on YSZ. This result confirms the findings from the MSR experiments that a likely reason contributing to the difference of MSR activity between Ni-SDC and Ni-YSZ is due to the different WGS activity over SDC and YSZ.

- The observation about the different activities of the electrolyte material toward the WGS reaction is of importance for the modelling part. Therefore, a kinetic study of the reverse WGS reaction on SDC was conducted and then implemented in the SOFC button cell model.

Kinetics of reverse Water Gas Shift Reaction on SDC:

- All kinetics experiments were performed with particulate diameter of 210 micrometer and a total flow rate 287 ml/min. The amount of catalyst used was varied so that for a total flow rate of 287 ml/min, it corresponded to a GHSV of 640 h^{-1}. At these conditions, there was no diffusion limitation (internal and external), as well as conversions far from equilibrium.

- The rate and equilibrium constants for RWGS were determined using Matlab codes involving solving a non-linear least square problem (lsqcurvefit command) where the exit gas composition was calculated assuming an integral reactor.

- The detailed mechanism for the reverse WGS reaction was based on Liu et al. (2010) that consisted of the five following steps:

$CO_2(g) + S \rightleftarrows CO_2.S$: Adsorption of CO_2 on the surface (7.1)

$CO_2.S + S \rightleftarrows CO.S + O.S$: Surface reaction I (7.2)

$H_2(g) + O.S \rightleftarrows H_2O.S$: Surface reaction II (7.3)

$H_2O.S \rightleftarrows H_2O(g) + S$: H_2O desorption (7.4)

$CO.S \rightleftarrows CO(g) + S$: CO desorption (7.5)

- Based on the Liu et al. (2010) reaction mechanism, the rate expressions were determined for each case where each one of the above reactions step were considered as the rate limiting step. The finding was that surface reaction I ($CO_2.S + S \leftrightarrow CO.S + O.S$) is the rate limiting step for the reverse WGS reaction on SDC.

- The various rate and equilibrium constants were then fitted using Matlab simulation so that the calculated CO_2 conversion matched the experimental data. The values of k, K_s and K_{H2O} are as follows:

$$k = 2.18 \times 10^5 e^{\frac{-111000}{RT}} \tag{7.6}$$

$$K_S = 3.36 \times 10^{10} e^{\frac{-256000}{RT}} \tag{7.7}$$

$$K_{H_2O} = 9.04 \times 10^8 e^{\frac{-197000}{RT}} \tag{7.8}$$

- The Matlab simulation was not able to calculate the uncertainty for the calculated parameters. In order to calculate the uncertainty for each parameters, a Markov Chain Monte Carlo (MCMC) study was conducted. This MCMC study was a collaboration with Professor Thomas A. Duever and his master student, Manoj Mathew from Chemical Department, University of Waterloo. It was determined that the expression of the rate of the reverse water-gas shift is:

$$r_{s1} = \frac{k\left(P_{CO_2} - \frac{P_{H_2O}P_{CO}}{K_p P_{H_2}}\right)}{\left(1 + K_L \frac{P_{H_2O}}{P_{H_2}}\right)^2} \tag{7.9}$$

- Even though the non-linear least square parameter estimation using Matlab was not able to calculate the uncertainty for each parameters estimate, this method was able to estimate the parameters very closely to those found using the MCMC method.

SOFC Modelling, Calibration and Validation:

- The cell performance obtained from the model for various gas compositions were compared with experimental data. The gas compositions were the followings: 97%H_2/3%H_2O, 20%CO/80%CO_2 and several syngas compositions (diesel, biomass, pre-reformed natural gas).

- For 97%H_2/3%H_2O fuel, the model results agreed well with the experimental data at 700 and 650^oC while somewhat over predicted the experimental values at 600^oC, particularly at high current density. For 20%CO/80%CO_2 fuel, the simulation results also showed good agreement with the experimental data at 700 and 650°C. However the fit between simulation and experimental results at 600°C was not as good: the simulation shows a much faster decrease in voltage than the experiment does at low current densities.

- A comparison between the polarization curves obtained for 20%H_2/80%H_2O and for 20%CO/80%CO_2 at three different temperatures (700, 650 and 600°C) was made. The finding is that the performance with H_2 is considerably higher than with CO. For example, the limiting current density at 600°C is about 4 times greater with H_2 than with CO, whereas at 700°C it is close to being 3 times higher.

- From the local current density plot for 97%H_2/3%H_2O at 700°C, it was seen that current is generated within a distance of 40 μm from the electrolyte, with 80% of the current being generated in the first 10 μm away from the electrolyte.

- For the syngas modelling, three different compositions were selected depending on whether the syngas originates from diesel reforming, natural gas pre-reforming or biomass gasification. Simulations of syngas took into account the WGS reaction over SDC, WGS on Ni and methane steam reforming. The cell performance (polarization curve) obtained from the simulation for these syngas compositions were compared with the experimental performance at 700°C. Diesel syngas produced higher performance, followed by pre-reformed natural gas and biomass.

- The results for pre-reformed natural gas fit the experimental data very well for a current density up to 10,000 A/m^2. Unfortunately, the model failed to converge at current densities greater than 10,000 A/m^2.

- For biomass syngas, the model results fit the experimental data very well, especially at high current density, but somewhat underestimate the experimental data at lower current density.

- Larger discrepancies between the model results and experimental data were observed for diesel syngas, especially at higher current density. One possible reason of the over prediction of cell voltage at high current density may be due to eventual carbon deposition that may have reduced the pore size, hence affecting the transport of species, especially at higher current density. Carbon deposition effects were not included in the model.

- Simulations with and without the term representing the WGS reaction on SDC for syngas were performed. Even though SDC itself is active toward the water-gas shift (WGS) reaction as shown in chapter 4, adding the term for the WGS reaction on SDC did not make any difference on the polarization curve. This is maybe due to the validity of the WGS rate expression in the SOFC operation condition, especially when the P_{H2O} is high (produced from the electrochemical reaction), under which condition, rate of WGS on SDC is very low.

7.2 Recommendations

- To see the effect of WGS on SDC to the SOFC performance, it is suggested to expand the kinetic study to higher concentration of water in order to increase the validity of the WGS on SDC in the SOFC modelling. This was not possible with the current experimental setup.

- For syngas involving methane, in addition to considering MSR, it is also worth to also include methane cracking in the model. We had problems to get the methane model converge, likely due to low methane conversion because of low MSR reaction, but the experimental data with pure methane were able to yield decent polarization curve. In addition, there seem to be some experimental evidence that, in the case of pure methane, carbon is being deposited mostly at the fuel channel/anode interface. This further point out to methane cracking, and thus adding methane cracking in the model should be more representative of what is happening for pure methane feed and help with the convergence issues for the methane model.

- The model can be extend to 2D model and include momentum and energy balances that are solved to predict pressure, velocity and temperature profiles inside the fuel channel.

- Increase the cell performance by applying graded anode design, where the anode is composed of two layers: the first one is the active layer in contact with the electrolyte. This is a thin layer designed to maximize electrochemical performance. The second layer is a thick layer used for mechanical strength, called the conduction layer. This second layer should conduct the electrons, should not present much resistance to the transport of the reactant to the active sites, and ideally should be quite inert to carbon deposition reactions.

- Finally, the model should be expanded to incorporate a detailed reaction mechanism for the chemical reactions on Ni, as well as on SDC. Such model would inherently be capable of identifying operating conditions and locations within the cell, where carbon deposition is more likely to occur.

Appendix A

Matlab Codes

The Matlab codes to solve the non-linear least square curve fitting problem consist of one main script (RWGS_Fitting-Arrhenius) and five function files (CO2_Conversion_Arrhenius, RWGS_ODE, Enthalpy, Entropy and RWGS).

A-1: RWGS_Fitting_Arrhenius Script

The main file (RWGS_Fitting-Arrhenius) was used to find the optimum model's parameters for the curve fitting where the CO_2 conversions from the simulation were compared to the experimental data to get the lowest resnorm (sum of squares of error). The key function of this script for solving the non-linear least square curve fitting is `lsqcurvefit`. CO_2 conversion was called from CO2_Conversion_Arrhenius file. In this main file, the experimental data number that need to be taken into account in each simulation at a given temperature, the initial guesses, upper and lower bounds of fitting parameters were set. The codes is given below:

```
% Step 1
% Determine k, K1, KH2 and KCO2 at a given temperature

clear
clc
clf

global P T Wt FT0 xH2 xCO2 xH2O xCO xI FH2 FCO2 FH2O FCO FI XCO2

%xCO2: mole fraction of CO2
%XCO2: conversion of CO2

% constants
R = 8.314;

Data =  xlsread('Experimental data.xlsx');

P = Data(:,2);
T = Data(:,3);
Wt = Data(:,4);
```

```
FT0 = Data(:,5);
xH2 = Data(:,6);
xCO2 = Data(:,7);
xCO = Data(:,8);
xH2O = Data(:,9);
xI = Data(:,10);
XCO2 = Data(:,11);
FH2 = Data(:,12);
FCO2 = Data(:,13);
FCO = Data(:,14);
FH2O = Data(:,15);
FI = Data(:,16);

% Selection of experiments to take into account
Expt = [57:60, 62:67, 69:71, 73:75];     % each number corresponds to the
Experiment# (see Excel spreadsheed "Experimental data.xlsx")
% Just enter the experiment # that need to be taken into account in Expt

% Selection of the corresponding experimental results
% Do not forget to make the selection change as well at the end of
Step1fun1.m

for i = 1:length(Expt)
    ydata(i) = XCO2(Expt(i));
end

% Initial guesses
x0 = [10 10 10 10 10];  % 1 to 6 parameters to estimate

% lower and upper bounds
lb =  [0 0 0 0 0];     % here must be positive
ub = [10000 10000 10000 10000 10000];      % arbitrary, might need to be
modified eventually

%options = optimset('TolFun',1e-8);
[x,resnorm] = lsqcurvefit(@CO2_Conversion_Arrhenius,x0,Expt,ydata,lb,ub)

% Plot comparision experiments/calculation

conversion = CO2_Conversion_Arrhenius(x,Expt);
plot(Expt,conversion,Expt,ydata)
legend('Simulated','Experiments')
xlabel('Experiment #')
title('CO2 Conversion')
```

A-2: CO2_Conversion_Arrhenius Function

The purpose of CO2_Conversion_Arrhenius file is to calculate CO_2 conversion based on CO_2 exit flow rate where the exit flow rate is called from RWGS file. CO2_Conversion_Arrhenius file was also used for the fitting parameters selection. The function is given below:

```
function conversion = CO2_Conversion_Arrhenius(x,Expt)
% Determine the conversion of CO2 at the bed exit

global P T Wt FT0 xH2 xCO2 xH2O xCO xI

% constants
R = 8.314;

% parameters to tune (can add more and put them as constant, eventually
% equal to zero not be taken into account
Tref = 973;

k_Tref =x(1);
E_k = 0;
Ks_Tref =x(2);
E_Ks = 0;
KH2_Tref = 0;
E_KH2 = 0;
KCO2_Tref =x(3);
E_KCO2 = 0;
KCO_Tref = x(4);
E_KCO = 0;
KH2O_Tref =x(5);
E_KH2O = 0;

for i = 1:length(Expt)
    k = k_Tref*exp(-E_k/R*(1/T(Expt(i))-1/Tref));
    Ks = Ks_Tref*exp(-E_Ks/R*(1/T(Expt(i))-1/Tref));
    KH2 = KH2_Tref*exp(-E_KH2/R*(1/T(Expt(i))-1/Tref));
    KCO2 = KCO2_Tref*exp(-E_KCO2/R*(1/T(Expt(i))-1/Tref));
    KCO = KCO_Tref*exp(-E_KCO/R*(1/T(Expt(i))-1/Tref));
    KH2O = KH2O_Tref*exp(-E_KH2O/R*(1/T(Expt(i))-1/Tref));

    K = [Ks;KH2;KCO2;KCO;KH2O];    % column vector for the adsorption
equilibrium constant

    [W,F] =
RWGS(T(Expt(i)),P(Expt(i)),Wt(Expt(i)),FT0(Expt(i)),xH2(Expt(i)),xCO2(Expt
(i)),xH2O(Expt(i)),xCO(Expt(i)),xI(Expt(i)),k,K);
```

```
    conversion(i) = (F(1,2)-F(end,2))/F(1,2);  % Determine CO2 conversion
XCO2

end
```

A-3: RWGS Function

The flow rate of gas species were calculated from RWGS file by solving a system of ordinary differential equations using ODE45 solver. RWGS file was also used to calculate equilibrium constant for global reaction from thermodynamics data where the enthalpy and entropy were calculated from Enthalpy and Entropy files, respectively. The function is given below.

```
function [W,F] = RWGS(T,P,Wt,FT0,xH2,xCO2,xH2O,xCO,xI,k,K)
% Determine the partial molar flow rate as a function of catalyst
% weight for H2, CO2, H2O and CO by solving a system of ODEs

% F(:,1) = H2
% F(:,2) = CO2
% F(:,3) = H2O
% F(:,4) = CO

% constants
R = 8.314;

% Calculation of Kp1
DH = enthalpy('H2O',T) + enthalpy('CO',T) - enthalpy('H2',T) -
enthalpy('CO2',T);
DS = entropy('H2O',T) + entropy('CO',T) - entropy('H2',T) -
entropy('CO2',T);
DG = DH - T*DS;
Kp = exp(-DG/R/T);

% Initial flow rate
FI = FT0*xI;                    % flow rate of inert
F0 = FT0*[xH2;xCO2;xH2O;xCO];   % vector of initial flow rate of reactive
species

% span over catalyst weight
Wspan = linspace(0,Wt,50);

[W,F] = ode45('RWGS_ODE',Wspan,F0,[],P,FI,k,Kp,K);
```

A-4: RWGS_ODE Function

In this file, the ordinary differential equations for gas species were set. In this file, the reaction rate expression for the simulation was also defined. The function is given below:

```
function Fdot = RWGS_ODE(W,F,flag,P,FI,k,Kp,K)
% H2 = 1
% CO2 = 2
% H2O = 3
% CO = 4
FT = F(1)+F(2)+F(3)+F(4)+FI;
PH2 = F(1)/FT*P;
PCO2 = F(2)/FT*P;
PH2O = F(3)/FT*P;
PCO = F(4)/FT*P;

%Use rs1 as limiting reaction
%DEN = 1+ K(3)*PCO2 + K(4)*PCO + K(5)*PH2O + K(1)*PH2O/PH2;
%DEN = 1+ K(2)*PH2 + K(3)*PCO2 + K(4)*PCO + K(5)*PH2O +
K(5)*PH2O/(K(1)*K(2)*PH2);
%DEN = 1+ K(2)*PH2 + K(3)*PCO2 + K(4)*PCO + K(5)/K(1)/K(2)*PH2O/PH2 +
K(5)*PH2O;
%DEN = 1+ PCO*PH2O/PH2/Kp + K(4)*PCO + K(5)*PH2O + K(5)/K(1)*PH2O/PH2;
DEN = 1+ K(3)*PCO2 + K(4)*PCO + K(5)*PH2O + K(5)/K(1)*PH2O/PH2;
%DEN = PH2O+ K(3)*PCO2*PH2O + K(5)*PH2O^2 + K(5)*PH2O^2/K(1)/PH2 +
Kp*K(4)*PH2*PCO2;
%DEN = PCO+ K(3)*PCO2*PCO + K(4)*PCO^2 + K(3)*PCO2*K(1)/K(4) +
K(5)*PH2O*PCO;
%DEN = PCO+ K(3)*PCO2*PCO + K(4)*PCO^2 + K(3)*PCO2*K(1)/K(4) +
Kp*K(5)*PH2*PCO2;

r1 = k*(PCO2-PCO*PH2O/PH2/Kp)/DEN^2;

Fdot = [-r1;-r1;r1;r1];
```

A-5: Enthalpy Function

The purpose of Enthalpy file was to calculate the enthalpy of formation of gas species at a given temperature.

```
function  H = enthalpy(species,T)
% Calculate the enthalpy of formation (J/mol) at temperature T

switch species
    case 'H2'
        i = 1;
    case 'CO2'
```

```
        i = 2;
    case 'CO'
        i = 3;
    case 'H2O'
        i = 4;
    otherwise
        error('species not recognized')
end

% Ideal gas heat capacity coeficients - Cp in J/(kmol.K) (from Perry's
handbook Table 2-156)
c = [27617 9560 2466 3760 567.6
    29370 34540 1428 26400 588
    29108 8773 3085.1 8455.3 1538.2
    33363 26790 2610.5 8896 1169];

% Enthalpy (J/mol) at 298.15K (from Perry's handbook Table 2.179)
H0 = [0;-393510;-110530;-241814];

Tspan = linspace(298.15,T,100);   % integration performed over 100 points

% Heat capacity at T (J/mol-K) - Formula from Perry's Handbook
Cp =
(c(i,1)+c(i,2)*(c(i,3)./Tspan./sinh(c(i,3)./Tspan)).^2+c(i,4)*(c(i,5)./Tsp
an./cosh(c(i,5)./Tspan)).^2)/1000;

% Enthalpy of formation at T (J/mol)
H = H0(i) + trapz(Tspan,Cp);
```

A-6: Entropy Function

The purpose of Entropy file was to calculate the entropy of gas species at a given temperature.

```
function S = entropy(species,T)
% Calculate the entropy (J/mol-K) at temperature T

switch species
    case 'H2'
        i = 1;
    case 'CO2'
        i = 2;
    case 'CO'
        i = 3;
    case 'H2O'
        i = 4;
    otherwise
        error('species not recognized')
```

```
end

% Ideal gas heat capacity coeficients - Cp in J/(kmol.K) (from Perry's
handbook Table 2-156)
c = [27617 9560 2466 3760 567.6
    29370 34540 1428 26400 588
    29108 8773 3085.1 8455.3 1538.2
    33363 26790 2610.5 8896 1169];

% Entropy (J/mol-K) at 298.15K (from Perry's handbook Table 2.179)
S0 = [130.571;213.677;197.556;188.724];

Tspan = linspace(298.15,T,100);   % integration performed over 100 points

% Heat capacity at T (J/mol-K)
Cp =
(c(i,1)+c(i,2)*(c(i,3)./Tspan./sinh(c(i,3)./Tspan)).^2+c(i,4)*(c(i,5)./Tsp
an./cosh(c(i,5)./Tspan)).^2)/1000;

% Entropy at T (J/mol-K)
S = S0(i) + trapz(Tspan,Cp./Tspan);
```

Appendix B

Derivation of r_{s1} rate expression

A global reverse WGS reaction can be decomposed as:

$CO_2(g) + S \rightleftarrows CO_2.S$ Adsorption of CO_2 on the surface (B.1)

$CO_2.S + S \rightleftarrows CO.S + O.S$ Surface reaction I (B.2)

$H_2(g) + O.S \rightleftarrows H_2O.S$ Surface reaction II (B.3)

$H_2O.S \rightleftarrows H_2O(g) + S$ H_2O desorption (B.4)

$CO.S \rightleftarrows CO(g) + S$ CO desorption (B.5)

The rate expressions for each elementary reaction are:

Adsorption of CO_2 on the surface:

$$r_{A1} = k_{A1}\left(P_{CO_2}C_v - \frac{C_{CO_2.S}}{K_{CO_2}}\right) \quad \text{(B.6)}$$

where

K_{CO_2} = adsorption equilibrium constant

C_v = concentration of vacant sites

$C_{CO_2.S}$ = concentration of sites with adsorbed CO_2

P_{CO_2} = partial pressure of CO_2

Surface reaction I:

$$r_{S1} = k_{S1}(C_{CO_2.S}C_v - \frac{C_{CO.S}\,C_{O.S}}{K_{S1}}) \quad \text{(B.7)}$$

where

K_{S1} = surface reaction I equilibrium constant

$C_{CO.S}$ = concentration of sites with adsorbed CO

$C_{O.S}$ = concentration of sites with adsorbed O

Surface reaction II:

$$r_{S2} = k_{S2}(P_{H_2}C_{O.S} - \frac{C_{H_2O.S}}{K_{S2}}) \quad \text{(B.8)}$$

where

K_{S2} = surface reaction II equilibrium constant

$C_{H_2O.S}$ = concentration of sites with adsorbed H_2O

P_{H_2} = partial pressure of H_2

Desorption of H_2O:

$$r_{D1} = k_{D1}\left(C_{H_2O.S} - \frac{P_{H_2O.}C_v}{K_{D_{H_2O}}}\right) \tag{B.9}$$

$$= k_{D1}\left(C_{H_2O.S} - K_{H_2O}P_{H_2O}C_v\right) \quad ; K_{H_2O}$$

$$= \frac{1}{K_{D_{H_2O}}}$$

where

K_{H_2O} = adsorption equilibrium constant

P_{H_2O} = partial pressure of H_2O

Desorption of CO

$$r_{D2} = k_{D2}\left(C_{CO.S} - \frac{P_{CO.}C_v}{K_{D_{CO}}}\right) \tag{B.10}$$

$$= k_{D2}(C_{CO.S} - K_{CO}P_{CO}C_v) \quad ; K_{CO} = \frac{1}{K_{D_{CO}}}$$

where

K_{CO} = adsorption equilibrium constant

P_{CO} = partial pressure of CO

Because surface reaction I is rate limiting, we have:

$$r = r_{S1} \tag{B.11}$$

$$\frac{r_{A1}}{k_{A1}} \approx 0 \qquad \text{so, } C_{CO_2.S} = K_{CO_2}P_{CO_2}C_v \tag{B.12}$$

$$\frac{r_{D1}}{k_{D1}} \approx 0 \qquad \text{so, } C_{H_2O.S} = K_{H_2O}P_{H_2O}C_v \tag{B.13}$$

$$\frac{r_{D2}}{k_{D2}} \approx 0 \qquad \text{so, } C_{CO.S} = K_{\mathrm{CO}}P_{\mathrm{CO}}C_v \tag{B.14}$$

$$\frac{r_{A2}}{k_{A2}} \approx 0 \qquad \text{so, } C_{O.S} = \frac{C_{H_2O.S}}{P_{H_2}K_{S2}} = \frac{K_{H_2O}P_{H_2O}C_v}{P_{H_2}K_{S2}} \tag{B.15}$$

Let the total concentration of active site be C_t:

$$C_t = C_v + C_{CO_2.S} + C_{CO.S} + C_{O.S} + C_{H_2O.S} \tag{B.16}$$

$$C_t = C_v + K_{CO_2}P_{CO_2}C_v + K_{\mathrm{CO}}P_{\mathrm{CO}}C_v + \frac{K_{H_2O}P_{H_2O}C_v}{P_{H_2}K_{S2}} + K_{H_2O}P_{H_2O}C_v \tag{B.17}$$

$$C_t = C_v[1 + K_{CO_2}P_{CO_2} + K_{\mathrm{CO}}P_{\mathrm{CO}} + \frac{K_{H_2O}P_{H_2O}}{P_{H_2}K_{S2}} + K_{H_2O}P_{H_2O}] \tag{B.18}$$

$$C_v = \frac{1}{1 + K_{CO_2}P_{CO_2} + K_{\mathrm{CO}}P_{\mathrm{CO}} + \frac{K_{H_2O}P_{H_2O}}{P_{H_2}K_{S2}} + K_{H_2O}P_{H_2O}} \tag{B.19}$$

Replacing the expression of the concentration of adsorption species into equation:

$$r_{S1} = k_{S1}(C_{CO_2.S}C_v - \frac{C_{CO.S}\,C_{O.S}}{K_{S1}}) \tag{B.20}$$

Will give us

$$r_{S1} = k_{S_1}\left(K_{CO_2}P_{CO_2}{C_v}^2 - \frac{K_{\mathrm{CO}}P_{\mathrm{CO}}C_vK_{H_2O}P_{H_2O}C_v}{K_{S1}K_{S2}P_{H_2}}\right) \tag{B.21}$$

$$= k_{S_1}{C_v}^2\left(K_{CO_2}P_{CO_2} - \frac{K_{\mathrm{CO}}K_{H_2O}P_{\mathrm{CO}}P_{H_2O}}{K_{S1}K_{S2}P_{H_2}}\right)$$

$$r_{S1} = k_{S_1}{C_v}^2K_{CO_2}\left[P_{CO_2} - \frac{K_{\mathrm{CO}}K_{H_2O}P_{\mathrm{CO}}P_{H_2O}}{K_{CO_2}K_{S1}K_{S2}P_{H_2}}\right] \tag{B.22}$$

$$= k_{S_1}{C_v}^2K_{CO_2}\left[P_{CO_2} - \frac{P_{\mathrm{CO}}P_{H_2O}}{K_PP_{H_2}}\right]$$

$$K_P = \frac{K_{CO_2}K_{S1}K_{S2}}{K_{\mathrm{CO}}K_{H_2O}} \tag{B.23}$$

$$r_{S1} = \frac{k_{\mathrm{S1}}{C_t}^2K_{CO_2}[P_{CO_2} - \frac{P_{\mathrm{CO}}P_{H_2O}}{K_{\mathrm{P}}P_{H_2}}]}{[1 + K_{CO_2}P_{CO_2} + K_{\mathrm{CO}}P_{\mathrm{CO}} + \frac{K_{H_2O}P_{H_2O}}{P_{H_2}K_{\mathrm{S2}}} + K_{H_2O}P_{H_2O}]^2} \tag{B.24}$$

$$r_{S1} = \frac{k[P_{CO_2} - \frac{P_{\mathrm{CO}}P_{H_2O}}{K_{\mathrm{P}}P_{H_2}}]}{[1 + K_{CO_2}P_{CO_2} + K_{\mathrm{CO}}P_{\mathrm{CO}} + \frac{K_{H_2O}P_{H_2O}}{P_{H_2}K_{\mathrm{S2}}} + K_{H_2O}P_{H_2O}]^2} \tag{B.25}$$

where $k = k_{\mathrm{S1}}{C_t}^2K_{CO_2}$

Appendix C

Arrhenius Plots for Each Limiting Steps

C-1: Arrhenius plots for adsorption of CO_2 on the surface rate limiting step

Rate limiting step	Rate of reaction
$CO_2(g) + S \leftrightarrow CO_2.S$	$r_{A1} = \frac{k\left(P_{CO_2} - \frac{P_{CO}P_{H_2O}}{K_p P_{H_2}}\right)}{\left(1 + \frac{K_{CO}K_{H_2O}P_{CO}P_{H_2O}}{K_{s1}K_{s2}P_{H_2}} + K_{CO}P_{CO} + \frac{K_{H_2O}P_{H_2O}}{K_{s2}p_{H_2}} + K_{H_2O}P_{H_2O}\right)}$ Where $k = C_t k_{A1}$ $K_p = \frac{K_{s1}K_{s2}}{K_{CO}K_{H_2O}}$

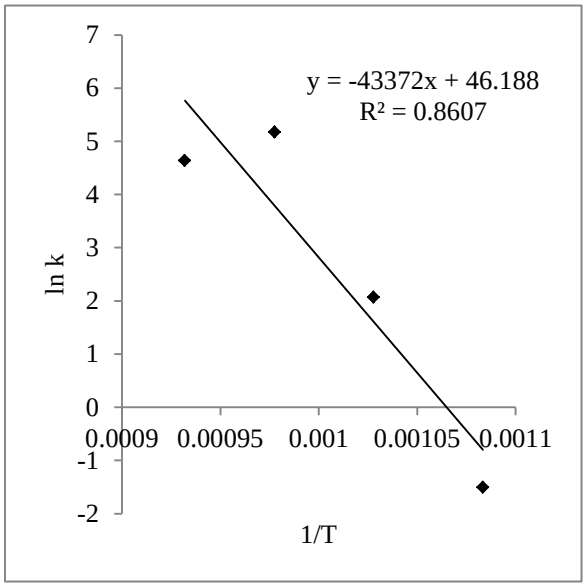

Figure C-1: Arrhenius plot of k

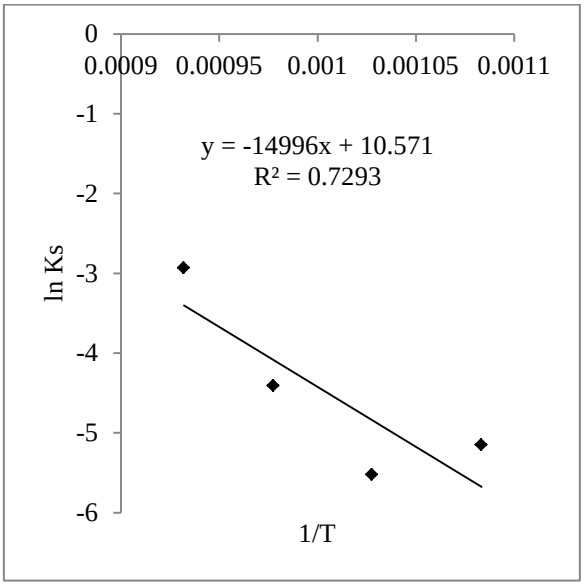

Figure C-2: Arrhenius plot of K_s

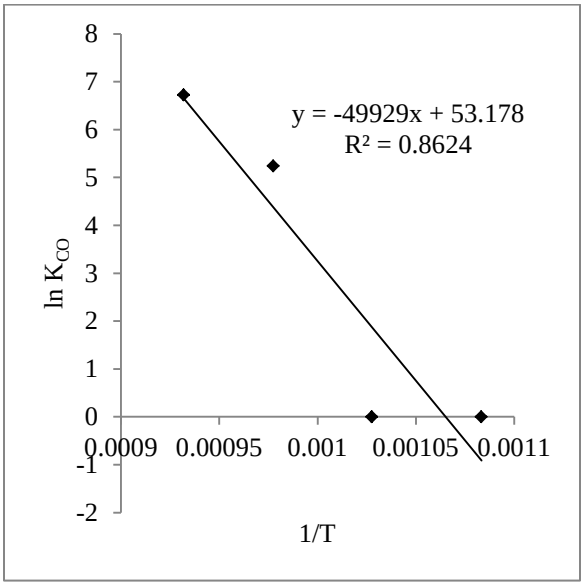

Figure C-3: Arrhenius plot of K_{CO}

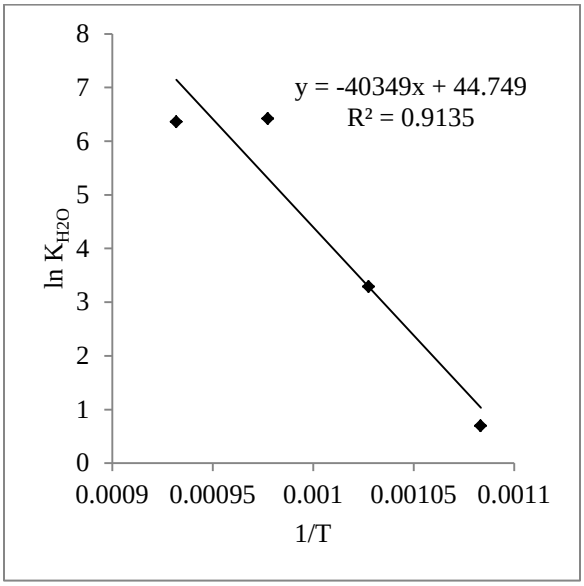

Figure C-4: Arrhenius plot of K_{H2O}

C-2: Arrhenius plots for surface reaction I rate limiting step

Rate limiting step	Rate of reaction
$CO_2.S + S \leftrightarrow CO.S + O.S$	$r_{s1} = \frac{k\left(P_{CO_2} - \frac{P_{H_2O}P_{CO}}{K_p P_{H_2}}\right)}{\left(1 + K_{CO_2}P_{CO_2} + K_{CO}P_{CO} + \frac{K_{H_2O}P_{H_2O}}{K_{s2}P_{H_2}} + K_{H_2O}P_{H_2O}\right)^2}$ Where $k = {C_t}^2 k_{s1} K_{CO_2}$ $K_p = \frac{K_{CO_2}K_{s1}K_{s2}}{K_{CO}K_{H_2O}}$

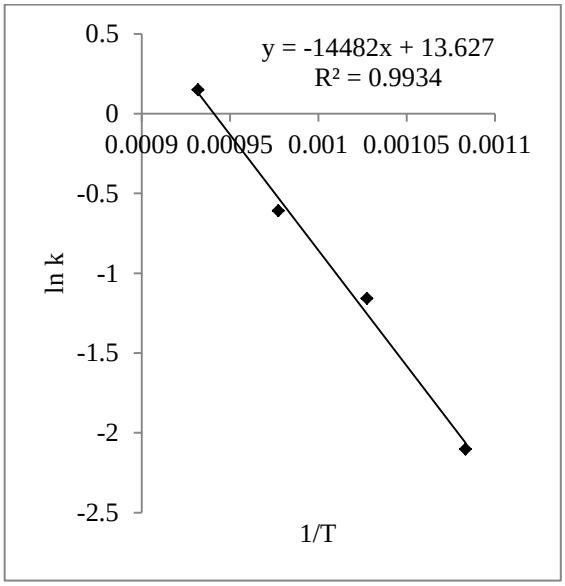

Figure C-5: Arrhenius plot of k

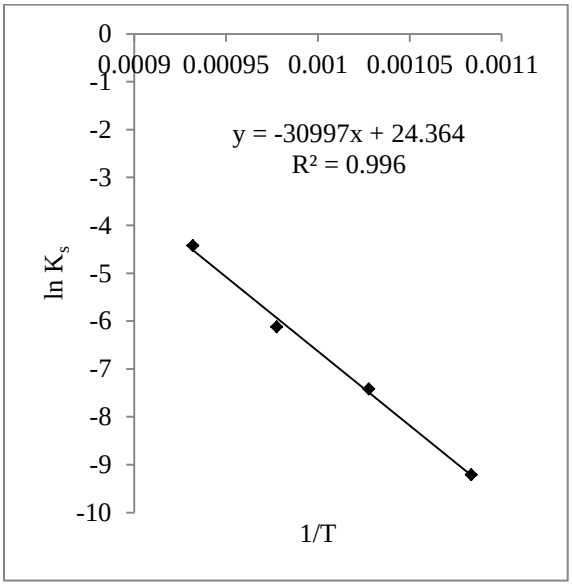

Figure C-6: Arrhenius plot of K_s

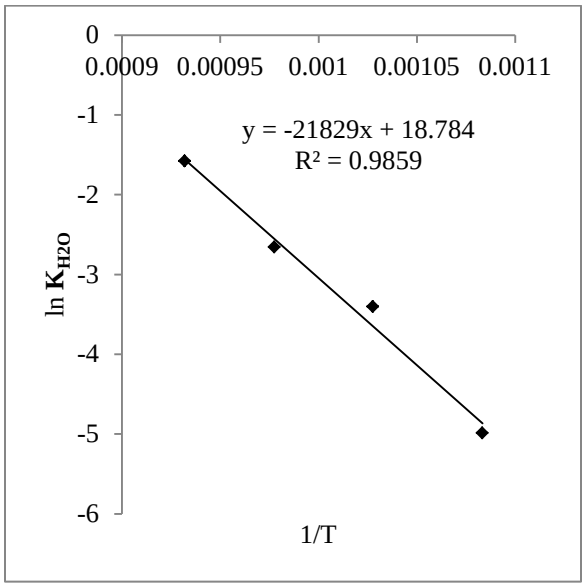

Figure C-7: Arrhenius plot of K_{H2O}

C-3: Arrhenius plots for surface reaction II rate limiting step

Rate limiting step	Rate of reaction
$H_2(g) + O.S \leftrightarrow H_2O.S$	$r_{s2} = \frac{k\left(\frac{P_{CO_2}P_{H_2}}{P_{CO}} - \frac{P_{H_2O}}{K_p}\right)}{\left(1 + K_{CO_2}P_{CO_2} + K_{CO}P_{CO} + \frac{K_{CO_2}P_{CO_2}K_{s1}}{K_{CO}P_{CO}} + K_{H_2O}P_{H_2O}\right)}$ $where\ \ k = \frac{C_t k_{s2} K_{CO_2} K_{s1}}{K_{CO}} \qquad K_p = \frac{K_{CO_2}K_{s1}K_{s2}}{K_{CO}K_{H_2O}}$

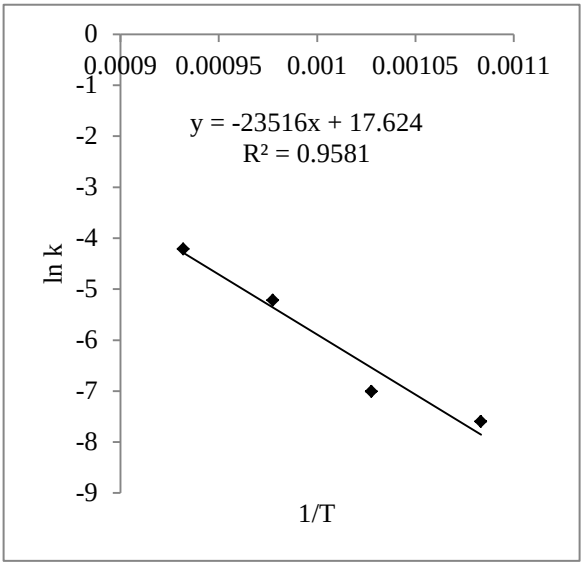

Figure C-8: Arrhenius plot of k

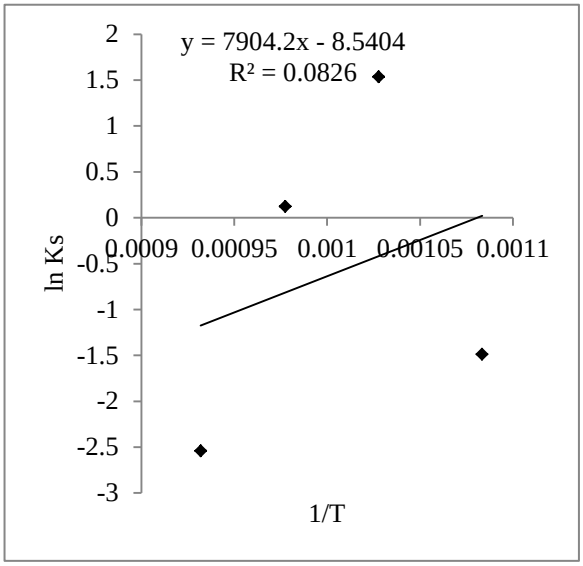

Figure C-9: Arrhenius plot of K_s

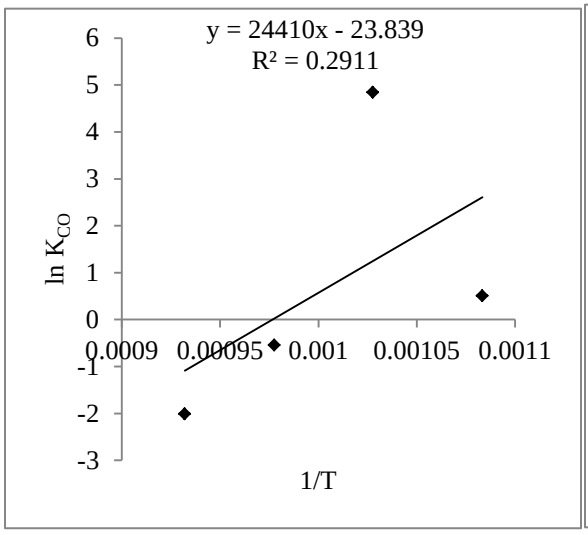

Figure C-10: Arrhenius plot of K_{CO}

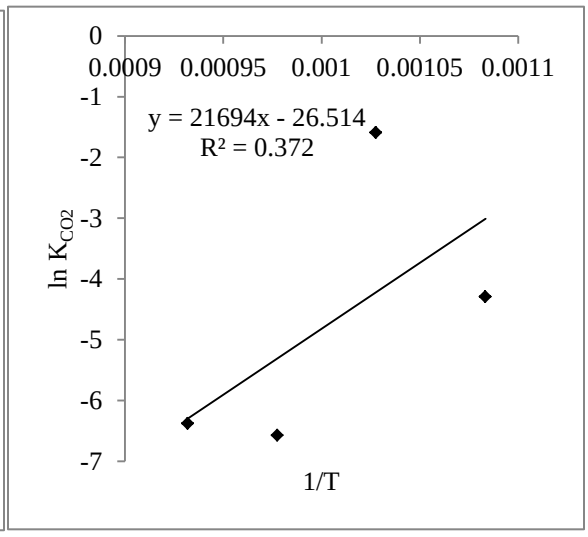

Figure C-11: Arrhenius plot of K_{CO2}

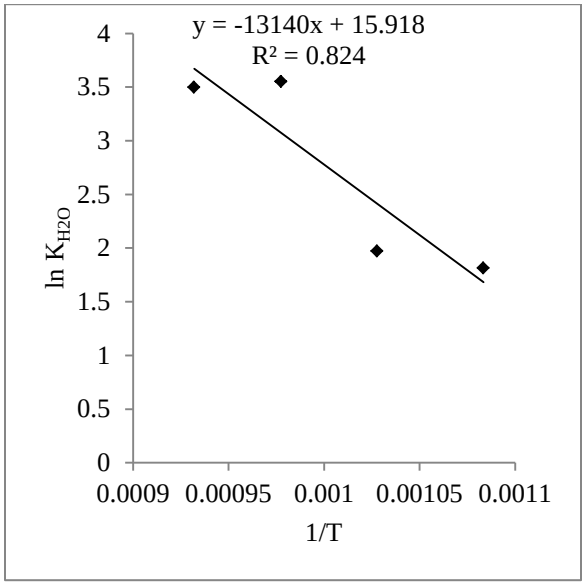

Figure C-12: Arrhenius plot of K_{H2O}

C-4: Arrhenius plots for H_2O desorption rate limiting step

Rate limiting step	Rate of reaction
$H_2O.S \leftrightarrow H_2O(g) + S$	$r_{D1} = \frac{k\left(\frac{P_{CO_2}P_{H_2}}{P_{CO}} - \frac{P_{H_2O}}{K_p}\right)}{\left(1 + K_{CO_2}P_{CO_2} + K_{CO}P_{CO} + \frac{K_{CO_2}P_{CO_2}K_{s1}}{K_{CO}P_{CO}} + \frac{K_{s1}K_{s2}K_{CO_2}P_{H_2}P_{CO_2}}{K_{CO}P_{CO}}\right)}$ Where $k = \frac{k_{D1}K_{s1}K_{s2}K_{CO_2}C_t}{K_{CO}}$ $K_p = \frac{K_{s1}K_{s2}K_{CO_2}}{K_{CO}K_{H_2O}}$

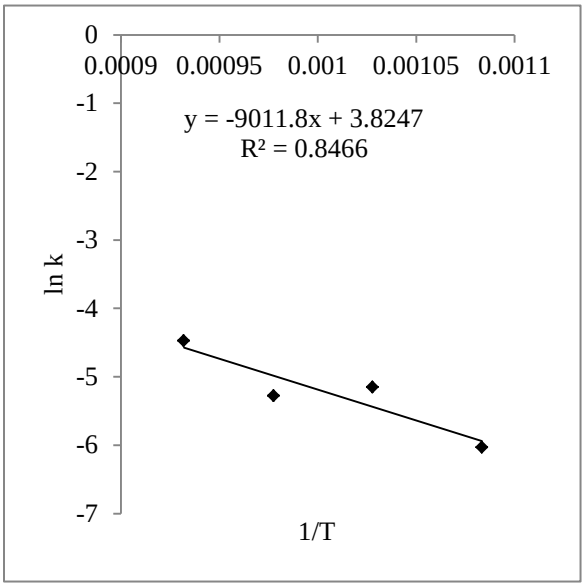

Figure C-13: Arrhenius plot of k

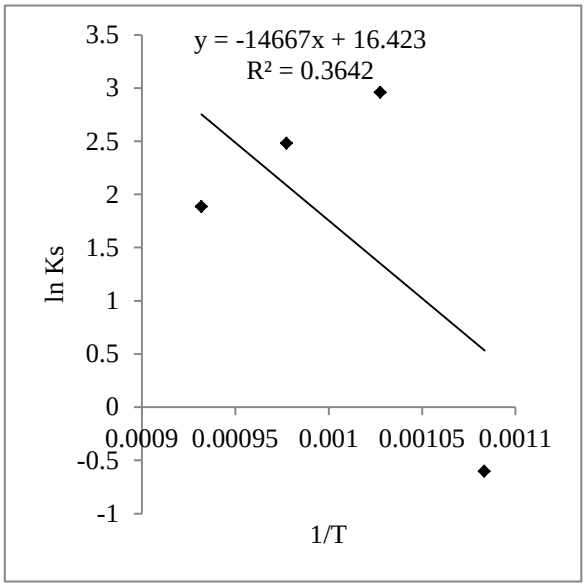

Figure C-14: Arrhenius plot of K_s

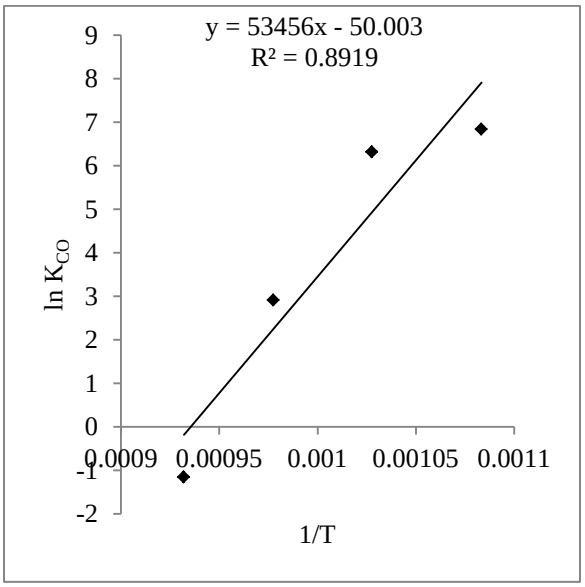

Figure C-15: Arrhenius plot of K_{CO}

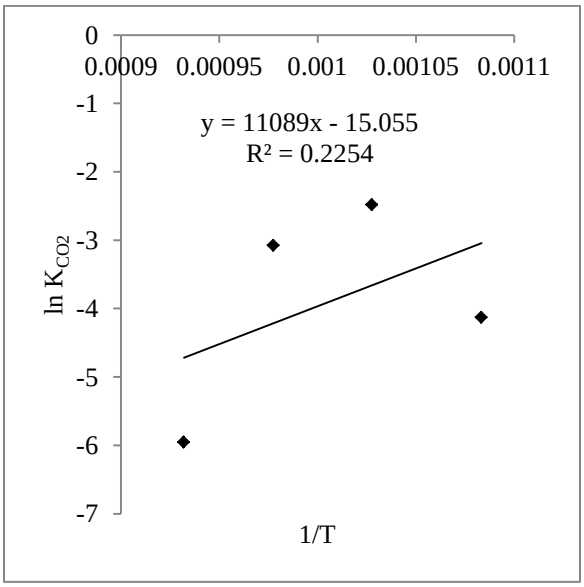

Figure C-16: Arrhenius plot of K_{CO2}

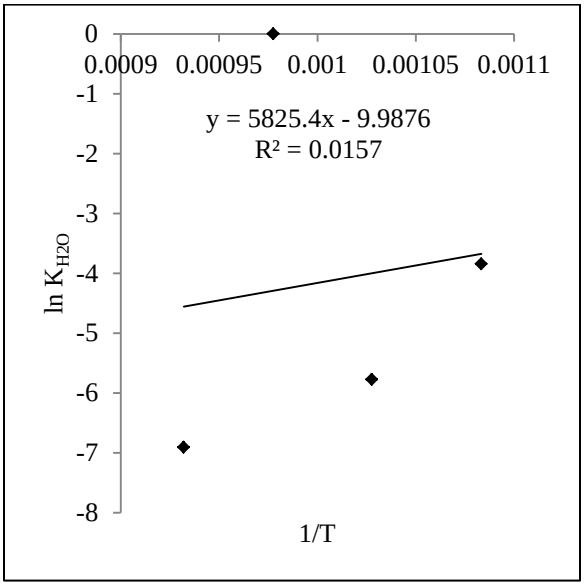

Figure C-17: Arrhenius plot of K_{H2O}

C-5: Arrhenius plots for CO desorption rate limiting step

Rate limiting step	Rate of reaction
$CO.S \leftrightarrow CO(g) + S$	$r_{D2}= \dfrac{k\left(\frac{P_{CO_2}P_{H_2}}{P_{H_2O}} - \frac{P_{CO}}{K_p}\right)}{\left(1 + K_{CO_2}P_{CO_2} + K_{H_2O}P_{H_2O} + \frac{K_{H_2O}P_{H_2O}}{K_{s2}P_{H_2}} + \frac{K_{s1}K_{s2}K_{CO_2}P_{H_2}P_{CO_2}}{K_{H_2O}P_{H_2O}}\right)}$ Where $k = \frac{k_{D2}K_{s1}K_{s2}K_{CO_2}C_t}{K_{H_2O}}$ $\quad K_p = \frac{K_{s1}K_{s2}K_{CO_2}}{K_{CO}K_{H_2O}}$

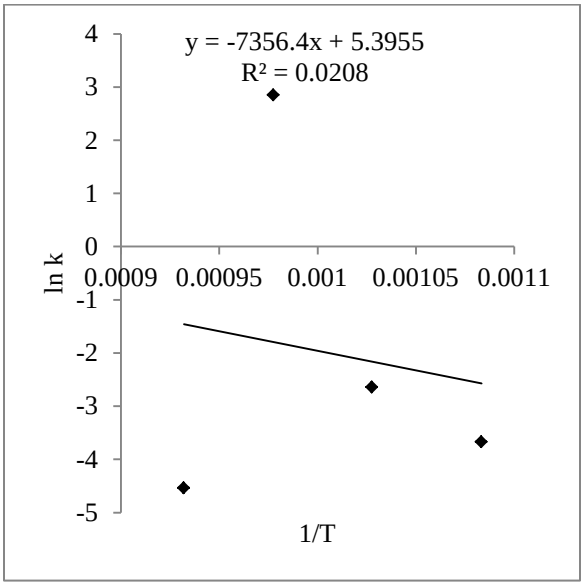

Figure C-18: Arrhenius plot of k

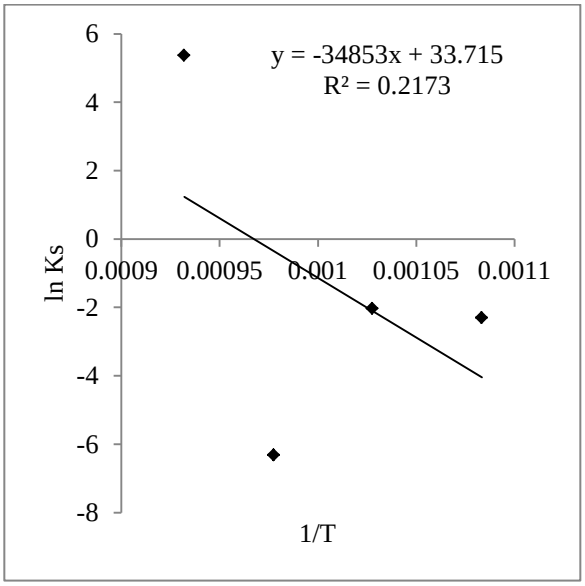

Figure C-19: Arrhenius plot of K_s

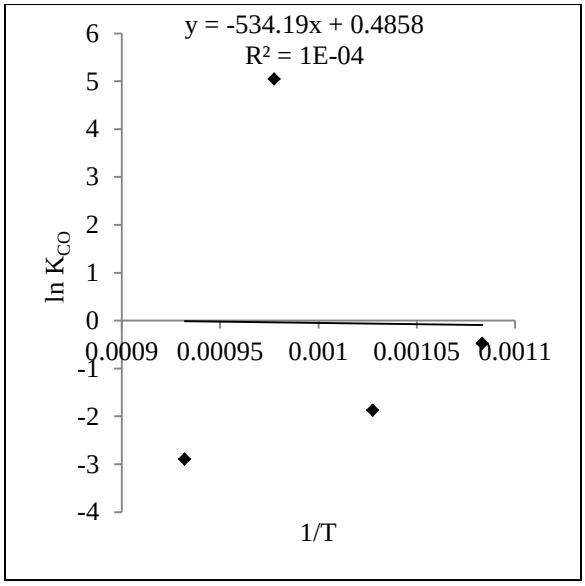

Figure C-20: Arrhenius plot of K_{CO}

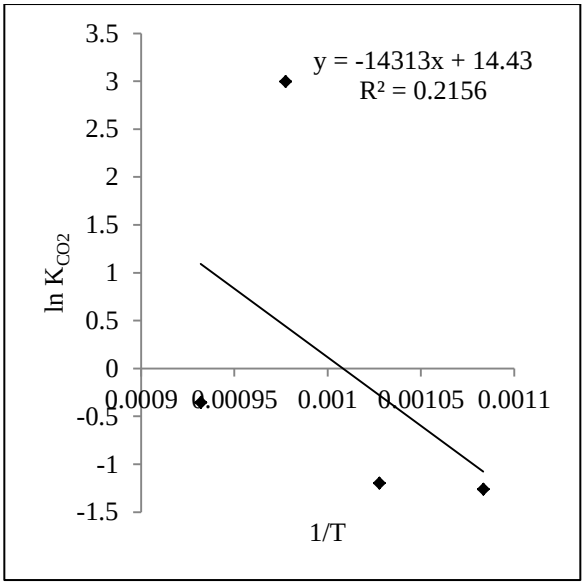

Figure C-21: Arrhenius plot of K_{CO2}

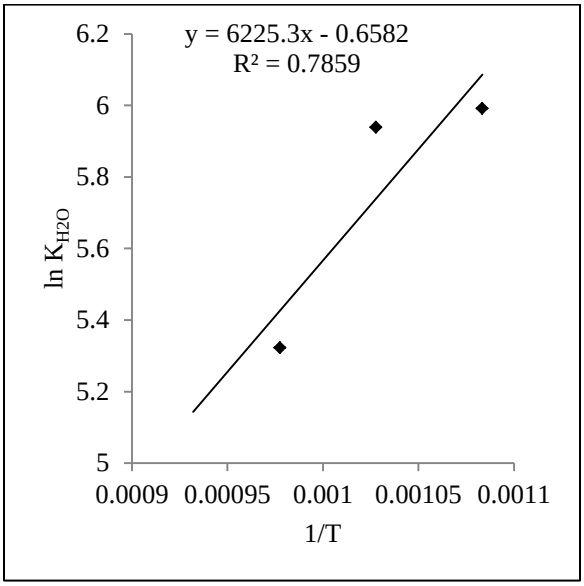

Figure C-22: Arrhenius plot of K_{H2O}

Bibliography

Aguiar, P., Adjiman, C. S., and Brandon, N. P. (2004). Anode-supported intermediate temperature direct internal reforming solid oxide fuel cell. I: Model-based steady-state performance. *Journal of Power Sources, 138*(1-2), 120-136.

Ahmed, K. and Foger, K. (2000). Kinetics of internal steam reforming of methane on Ni/YSZ based anodes for solid oxide fuel cells. *Catalysis Today, 63*(2-4), 479-487.

Aravind, P., Ouweltjes, J. P., Woudstra, N. and Rietveld, B., (2004), "SOFC Performance with Biomass-Derived Gas", in *Proceedings of 6th European Solid Oxide Fuel Cell Forum*, M. Morgensen (Ed.), Lucerne, Switzerland, 1514-1523.

Arpino, F., Carotenuto, A., Massarotti, N., and Nithiarasu, P. (2008). A robust model and numerical approach for solving solid oxide fuel cell (SOFC) problems. *International Journal of Numerical Methods for Heat and Fluid Flow, 18*(7-8), 811-834.

Badwal, S.P.S and Foger, K., (1996), Solid Oxide Electrolyte Fuel Cell Review, *Ceramics International*, 22, 257-265.

Badwal, S.P.S., (2001), Stability of Solid Oxide Fuel Cell Components, *Solid State Ionics*, 143, 39-46.

Balzhiser, R.E., Samuels, M.R. and Eliassen, J.D., (1972), Chemical Engineering Thermodynamics, Prentice-Hall, New Jersey, USA.

Blaylock, D. W., Teppei Ogura, D. W., William H. Green, D. W. and Gregory J. O. Beran, D.Wayne. (2009). Computational investigation of thermochemistry and kinetics of steam methane reforming on ni(111) under realistic conditions. *Journal of Physical Chemistry C, 113*(12), 4898-4908.

Boder, M., and Dittmeyer, R. (2006). Catalytic modification of conventional SOFC anodes with a view to reducing their activity for direct internal reforming of natural gas. *Journal of Power Sources, 155*(1), 13-22.

Bove, R., Lunghi, P., & M. Sammes, N. (2005). SOFC mathematic model for systems simulations. part one: From a micro-detailed to macro-black-box model. *International Journal of Hydrogen Energy, 30*(2), 181-187.

Cayan, F. N., Pakalapati, S. R., Elizalde-Blancas, F., and Celik, I. (2009). On modeling multi-component diffusion inside the porous anode of solid oxide fuel cells using fick's model. *Journal of Power Sources, 192*(2), 467-474.

Cheekatamarla, P.K., Finnerty,C. M. and Cai, Jun (2008) Internal reforming of hydrocarbon fuels in tubular solid oxide fuel cells. *International Journal of Hydrogen Energy*, 33 1853 – 1858.

Chen, M., Kim, B.H., Xu, Q., Ahn, B.K., Kang, W.J, and Huang, D.P., (2009). Synthesis an Electrical Properties of $Ce_{0.8}Sm_{0.2}O_{1.9}$ Ceramics for IT-SOFC Electrolytes by Urea-combustion technique. *Ceramic International*, 35, 1335–1343.

Chick, L. A., Pederson, L. R., Maupin, G. D., Bates, J. L., Thomas, L. E., & Exarhos, G. J. (1990). Glycine-nitrate combustion synthesis of oxide ceramic powders. *Materials Letters*, 10(1–2), 6-12.

Chou, Y., and Stevenson, J. W. (2002). Thermal cycling and degradation mechanisms of compressive mica-based seals for solid oxide fuel cells. *Journal of Power Sources, 112*(2), 376-383.

Clarke, S. H. Dicks, A. L., Pointon, K., Smith, T. A. and Swann, A., (1997). Catalytic Aspects of the Steam Reforming of Hydrocarbons in Internal Reforming Fuel Cells. *Catalysis Today, 38*(4), 411-423.

Cui, D., Liu, Q., Chen, F. (2010). Modeling of anode-supported SOFCs with samaria doped-ceria electrolytesoperating at 500–600^{o}C. *Journal of Power Sources*, 195, 4160–4167.

Danilov, V. A. and Tade, M. O. (2009). A CFD-based model of a planar SOFC for anode flow field design. *International Journal of Hydrogen Energy, 34*(21), 8998-9006.

Daubert, T.E., (1985). Chemical Engineering Thermodynamics, McGraw-Hill, New York, USA.

Deseure, J., Bultel, Y., Dessemond, L., and Siebert, E. (2005). Theoretical optimisation of a SOFC composite cathode. *Electrochimica Acta, 50*(10), 2037-2046.

Ding, J. and Liu, J. (2008). An anode-supported solid oxide fuel cell with spray-coated yttria-stabilized zirconia (YSZ) electrolyte film, *Solid State Ionics*, 179(21-26), 1246-1249.

Dokiya, M. (2002). SOFC system and technology. *Solid State Ionics, 152-153*, 383-392.

Ernst, K-H., Campbell, C.T. and Moretti, G. (1992). Kinetics Of The Reverse Water-Gas Shift Reaction Over Cu(110). *Journal of Catalysis*, 134, 66-74.

Farhad,S. and Hamdullahpur, F. (2012). Minimization of Polarization Resistance in Solid Oxide Fuel Cells by Proper Design of Micro-/nano-structure of Porous Composite Electrodes. *Electrochimica Acta*, 61, 1-12.

Fergus, J.W., (1990). Oxide Anode Materials for Solid Oxide Fuel Cells, *Journal of Solid State Ionics*, 177, 1529-1541.

Fergus, J. W., Hui, R., Li, X., Wilkinson, D. P. and Zhang, J. (2009). Solid Oxide Fuel Cells Materials Properties and Performance. Boca Raton: CRC Press.

Geankoplis, C. J. (2003). Transport processes and separation process principles : (includes unit operations) (4^{th} ed.). Upper Saddle River, NJ: Prentice Hall.

Gines, M.J.L., Marchi, A.J. and Apesteguia, C.R. (1997). Kinetic study of the reverse water-gas shift reaction over $CuO/ZnO/A1_2O_3$ catalysts. *Applied Catalysis A: General*, 154, 155-171.

Goguet, A., Meunier, F., Breenm, J.P., Burch, R., Petch, M.I., Ghenciu, A.F. (2004) .Study of the origin of the deactivation of a Pt/CeO_2 catalyst during reverse water gas shift (RWGS) reaction. *Journal of Catalysis*, 226, 382–392.

Gunji, A., Kobayashi, T., Takahashi, H., Wen, C., Otomo, J., Ukai, K., et al. (2004). Carbon deposition behaviour on ni-ScSZ anodes for internal reforming solid oxide fuel cells. *Journal of Power Sources, 131*(1-2), 285-288.

Hart, N. T., Brandon, N. P., Day, M. J., and Shemilt, J. E. (2001). Functionally graded cathodes for solid oxide fuel cells. *Journal of Materials Science, 36*(5), 1077-1085.

Hecht, E.S., Gupta, G.K., Zhu, H., Dean, A. M., Kee, R.J., Maier, L., Deutschmann, O. (2005). Methane reforming kinetics within a Ni–YSZ SOFC anode support. *Applied Catalysis A: General*, 295, 40–51.

Hofmann, P., Panopoulos K. D., Fryda, L.E. and Kakaras, E. (2009) Comparison between two methane reforming models applied to a quasi-two-dimensional planar solid oxide fuel cell model, *Energy*, 34, 2151–2157.

Hofmann, Ph. and Panopoulos, K.D. (2010). Detailed dynamic Solid Oxide Fuel Cell modeling for electrochemical impedance spectra simulation. *Journal of Power Sources*, 195, 5320–5339.

Hui, R., Sun, C., Yick, S., Decès-Petit, C., Zhang, X., Maric, R. and Ghosh, D. (2010). $Ba_{1-x}Pr_xCo_{1-y}Fe_yO_{3-\delta}$ as cathode materials for low temperature solid oxide fuel cells. *Electrochimica Acta*, 55, 4772–4775.

Hussain, M. M., Li, X., and Dincer, I. (. (2009). A numerical investigation of modeling an SOFC electrode as two finite layers. *International Journal of Hydrogen Energy, 34*(7), 3134-3144.

Hussain, M., Li, X., and Dincer, I. (2006). Mathematical modeling of planar solid oxide fuel cells. *Journal of Power Sources, 161*(2), 1012-1022.

Ivers-Tiffee, E., Weber, A. and Herbstritt, D., (2001), Materials and Technologies for SOFC Components" *Journal of European Ceramic Society*, 21, 1805-1811.

Janardhanan, V. M., and Deutschmann, O. (2006). CFD analysis of a solid oxide fuel cell with internal reforming: Coupled interactions of transport, heterogeneous catalysis and electrochemical processes. *Journal of Power Sources, 162*(2), 1192-1202.

Jorgensen, M.J., Holtappels, P. and Appel, C.C., (2000). Durability Test of SOFC Cathode, *Journal of Applied Electrochemistry*, 30(4), 411-418.

Li, C., Shi, Y., and Cai, N. (2010). Elementary reaction kinetic model of an anode-supported solid oxide fuel cell fueled with syngas. *Journal of Power Sources, 195*(8), 2266-2282.

Li, X. (2006). Principles of fuel cells. Taylor & Francis, New York.

Lisbona, P., Uche, J., and Serra, L. (2005). High-temperature fuel cells for fresh water production. *Desalination, 182*(1-3), 471-482.

Liu, C., Munjanja, L., Cundari, T.R. and Wilson, A.K. (2010). Theoretical Studies on the Catalysis of the Reverse Water-Gas Shift Reaction Using First-Row Transition Metal *β*-Diketiminato Complexes. *J. Phys. Chem. A***,** 114, 6207–6216.

Liu, Y., Compson, C., and Liu, M. (2004). Nanostructured and functionally graded cathodes for intermediate temperature solid oxide fuel cells. *Journal of Power Sources, 138*(1-2), 194-198.

Minh, N. Q. and Takahashi, T. (1995). Science and Technology of Ceramic Fuel Cells. Amsterdam: Elsevier Science.

Mogensen, D., Grunwaldt, J.-D., Hendriksen, P.V., Dam-Johansen, K., Nielsen, J.U. (2011). Internal steam reforming in solid oxide fuel cells: Status and opportunities of kinetic studies and their impact on modeling: A review. *Journal of Power Sources*, 196, 25–38.

Nagata, S., Momma, A., Kato, T. and Kasuga, Y. (2001). Numerical analysis of output characteristics of tubular SOFC with internal reformer. *Journal of Power Sources, 101*(1), 60-71.

Nagata, S., Momma, A., Kato, T. and Kasuga, Y., (2001). Numerical Analysis of Output Characteristics of Tubular SOFC with Internal Reformer. *Journal of Power Sources*, 101, 60-71.

Nandasiri, M. I. (2013). Engineered Interfaces and Nano-scale Thin Films for Solid Oxide Fuel Cell Electrolytes. PhD Thesis, Western Michigan University.

Ni, M., Leung, D.Y.C. and Leung, M.K.H. (2009). Electrochemical modeling and parametric study of methane fed solid oxide fuel cells, *Energy Conversion and Management*, 50, 268–278.

Ni, M., Leung, M.K.H. and Leung, D.Y.C. (2007). Micro-Scale Modeling of a Functionally Graded Ni-YSZ Anode, *Chem. Eng. Technol.*, *30*(5), 587–592.

O'Hayre, R. P., Cha, S. W., Colella, W. and Prinz, F. B. (2006). Fuel Cell Fundamentals, John Wiley & Sons, New York.

Pastula, M., Devitt, J., Boersma, R. and Ghosh, D., (2001). Fuel Processing Development at Global Thermoelectric Inc., in *Proceedings of Solid Oxide FuelCell VII*, Singhal, S.C., and Dokiya, M.(Eds), The Electrochemical Society Proceedings Series, Pennington, NJ, 180-189.

Peng, R., Xia, C., Fu, Q., Meng, Q. and Peng, D. (2002), Sintering and Electrical Properties of $(CeO_2)_{0.8}(Sm_2O_3)_{0.1}$ Powders Prepared by Glycine-nitrate Process, *Materials Letters*, 56, 1043 – 1047.

Peng, R., Xia, C., Peng, D. and Meng, G. (2004). Effect of Powder Preparation on (CeO2)0.8(Sm2O3)0.1 Thin Film Properties by Screen-printing, *Materials Letters*, 58(5), 604-608.

Pharoah, J. G., Karan, K. and Sun, W. (2006). On Effective Transport Coefficients in PEM Fuel Cell Electrodes: Anisotropy of the Porous Transport Layers, *Journal of Power Sources*, 161, 214-224.

Phongaksorn, M. (2010). The Development of $Ni_{1-x-y}Cu_xMg_yO$-SDC Anode for Intermediate Temperature Solid Oxide Fuel Cells (IT-SOFCs). PhD Thesis, University of Waterloo.

Rass-Hansen, J., Christensen, C.H., Sehested, J., Helveg, S., Rostrup-Nielsen, J. R. and Dahl, S. (2007). Renewable hydrogen: carbon formation on Ni and Ru catalysts during ethanol steam-reforming. *Green Chem.*, 9, 1016–1021.

Reid, R. C., Prausnitz, J. M., and Poling, B. E. (1987). *Properties of gases and liquids* (4^{th} ed.). New York ; Montreal: McGraw-Hill.

Sanchez, D., Chacartegui, R., Munoz, A., and Sanchez, T. (2008). On the effect of methane internal reforming modelling in solid oxide fuel cells. *International Journal of Hydrogen Energy*, *33*(7), 1834-1844.

Selman, J. R. and Lin, Y. P. (1993). Application of ac impedance in fuel cell research and development. *Electrochimica Acta, 38*(14), 2063-2073.

Shi, Y. and Cai, N. (2006). General mechanistic model of solid oxide fuel cells. *Tsinghua Science and Technology, 11*(6), 701-711

Shi, Y., Cai, N., Li, C., Bao, C., Croiset, E., Qian, J., et al. (2007a). Modeling of an anode-supported ni-YSZ|Ni-ScSZ|ScSZ|LSM-ScSZ multiple layers SOFC cell. *Journal of Power Sources, 172*(1), 235-245.

Shi, Y., Chai, N., Li, C. (2007). Numerical modeling of an anode-supported SOFC button cell considering anodic surface diffusion. *Journal of Power Sources*, 164, 639–648.

Singh, K., Acharya, S.A. and Bhoga, S.S, (2007) Low Temperature processing of Dense Samarium-doped CeO2 Ceramics: Sintering and Intermediate Temperature Ionic Conductivity, *Ionics*, 13, 429 – 434.

Singhal, S. C. (2000). Advances in solid oxide fuel cell technology. *Solid State Ionics, 135*(1-4), 305-313.

Singhal, S. C. (2000). Advances in solid oxide fuel cell technology. *Solid State Ionics, 135*(1-4), 305-313.

Singhal, S.C. and Kendall, K. (2003). High temperature solid oxide fuel cell: Fundamental, design and application. Elsevier Advanced Technology, Oxford, UK.

Stambouli, A. B. and Traversa, E. (2002). Solid oxide fuel cells (SOFCs): A review of an environmentally clean and efficient source of energy. *Renewable & Sustainable Energy Reviews, 6*(5), 433-455

Suwanwarangkul, R., Croiset, E., Fowler, M.W., Douglas, P.L., Entchev, E., Douglas, M.A. (2003). Performance comparison of Fick's, dusty-gas and Stefan–Maxwell models to predict the concentration overpotential of a SOFC anode. *Journal of Power Sources*,122, 9–18.

Suwanwarangkul, R., Croiset, E., Entchev, E., Charojrochkul, S., Pritzker, M. D., Fowler, M. W., et al. (2006). Experimental and modeling study of solid oxide fuel cell operating with syngas fuel. *Journal of Power Sources, 161*(1), 308-322.

Ursaki, V. V., Lair, V., Zivkovic, L., Cassir, M., Ringuede, A. and Lupan, O., (2012). Optical Properties of Sm-doped Ceria Nanostructured Films Grown by Electrodeposition at Low Temperature. *Optical Materials*, 34, 1897-1901.

Wang, K., Ran, R., Zhou, W., Gu, H., Shao, Z and Ahn, J., (2008), Properties and Performance of $Ba_{0.5}Sr_{0.5}CO_{0.8}$ $Fe_{0.2}O_{3-\delta}$+ $Sm_{0.2}Ce_{0.8}O_{1.9}$ Composite Cathode, *Journal of Power Sources*, 179, 60 – 68.

Wei Zhang (2006). Simulation of Solid Oxide Fuel Cell-Based Power Generation Processes with CO_2 Capture. Master Thesis, University of Waterloo.

Wincewics, K.C. and Cooper, J.S., (2005). Taxonomies of SOFC Material & Manufacturing Alternatives, *Journal of Power Sources*, 140, 280-2965.

Xia, C., and Liu, M. (2001). Low-temperature SOFCs based on $Gd_{0.1}Ce_{0.9}O_{1.95}$ Fabricated by Dry Pressing. *Solid State Ionics*, 144(3-4), 249-255.

Yahiro, H., Eguchi, Y., Eguchi, K. and Arai, H. (1988). Oxygen Ion Conductivity of the Ceria-Samarium Oxide System with Fluorite Structure, *Journal of Applied Electrochemistry*, 18, 527-531.

Yakabe, H., Hishinuma, M., Uratani, M., Matsuzaki, Y., and Yasuda, I. (2000). Evaluation and modelling of performance of anode-supported solid oxide fuel cell. *J.Power Sources, 86*(1/2), 423-431.

Yamamoto, O. (2000). Solid oxide fuel cells: Fundamental aspects and prospects. *Electrochimica Acta, 45*(15-16), 2423-2435.

Yan, A., Phongaksorn, M., Nativel, D. and Croiset, E. (2012). Lanthanum promoted NiO–SDC anode for low temperature solid oxide fuel cells fueled with methane. *Journal of Power Sources*, 210, 374–380.

Yang, R.J., Lee, M.C., Chang, J.C., Lin, T.N., Chang, Y.C., Kao, W.X., Lee, L.S, and Cheng, S.W., (2012). Fabrication and Characterization of a $Sm_{0.2}Ce_{0.8}O_{1.9}$ Electrolyte Film by the Spin-Coating Method for a Low-temperature Anode-supported Solid Oxide Fuel Cells. *Journal of Power Sources*, 206, 111–118.

Young, D., Sukeshini, A. M., Cummins, R., Xiao, H., Rottmayer, M., and Reitz, T. (2008). Ink-jet printing of electrolyte and anode functional layer for solid oxide fuel cells. *Journal of Power Sources, 184*(1), 191-196.

Yuan, J. (2010). Simulation and Analysis of Multi-scale Transport Phenomena and Catalytic Reactions in SOFC Anodes. *Chemical Product and Process Modeling*, 5 (1), Article 12.

Zhao, F., Wang, Z., Liu, M., Zhang, L., Xia, C., Chen, F. (2008). Novel nano-network cathodes for solid oxide fuel cells. *Journal of Power Sources*,185, 13–18.

Zhu, H., and Kee, R. (2008). Modeling distributed charge-transfer processes in SOFC membrane electrode assemblies. *Journal of the Electrochemical Society, 155*(7), B715-B729.

Zhu, H., and Kee, R. J. (2011). Two-dimensional model of distributed charge transfer and internal reforming within unit cells of segmented-in-series solid-oxide fuel cells. *Journal of Power Sources, 196*(18), 7654-7664.

Zhu, H., Kee, R., Janardhanan, V., Deutschmann, O., & Goodwin, D. (2005). Modeling elementary heterogeneous chemistry and electrochemistry in solid-oxide fuel cells. *Journal of the Electrochemical Society, 152*(12), A2427-A2440.

Zhu, W. Z., and Deevi, S. C. (2003). A review on the status of anode materials for solid oxide fuel cells. *Materials Science and Engineering A, 362*(1-2), 228-239.